USING REMOTE SENSING TO DEVELOP IRRIGATION SCHEDULING TOOLS FOR VARIABLE RATE IRRIGATION

by

LORENA NUNES LACERDA

(Under the Direction of George Vellidis)

ABSTRACT

Current irrigation management zones (IMZs) for variable rate irrigation (VRI) systems are static. They are delineated in the beginning of the season and used thereafter. However, recent research has shown that IMZs boundaries are transient and change with time. Plant-based measurements such as leaf water potential (LWP) are being widely used on irrigation scheduling because of its accurate indication of when irrigation is needed. However, LWP is time consuming and scale limited. In this context, authors have explored the use of remote sensing to detect or estimate crop water status to overcome this limitation. Three studies were conducted in experimental and commercial cotton field in 2018, 2019 and 2020 to evaluate the use of remote sensing to develop dynamic irrigation management zones for variable rate irrigation in cotton. The first study was conducted in two experimental cotton fields located in Camilla, GA in the 2018 and 2020 growing seasons. In this study, ground physiological measurements, and remotely sensed data from unmanned aerial vehicle (UAV) were collected weekly in 2018 and biweekly in 2020. The second study was conducted in a commercial cotton field in South Georgia in 2019 and 2020. UAV and satellite data were collected weekly in both seasons. Soil water tension and a variety of physiological parameters were also collected in the same day as the flights. Predicted

plant height map was used to change IMZs boundaries during the cotton vegetative stage. The last study was conducted in 2019. Satellite images were downloaded from three different locations in Southern USA. Available coarse thermal images from MODIS were sharpened at 30, 60, 120, and 240 m resolutions using NDVI developed from Sentinel-2 and VENμS. Results from the three studies indicated great potential in the use of remote sensing to delineate dynamic management zones. Based on results predicted LWP maps can be created based on UAV-based canopy temperature. Sharpening of coarse thermal satellite images also showed relevant results for field scale. Indirect indicators of water status such as plant height was shown to be a great alternative for management zones delineation during the initial stages of growth and development.

INDEX WORDS: variable rate irrigation, vegetation indices, canopy temperature, thermal images, multispectral images, cotton

USING REMOTE SENSING TO DEVELOP IRRIGATION SCHEDULING TOOLS FOR VARIABLE RATE IRRIGATION

by

LORENA NUNES LACERDA

BS, Universidade Federal de Lavras, Brazil, 2015

A Dissertation Submitted to the Graduate Faculty of The University of Georgia in Partial Fulfillment of the Requirements for the Degree

DOCTOR OF PHILOSOPHY

ATHENS, GEORGIA

2021

USING REMOTE SENSING TO DEVELOP IRRIGATION SCHEDULING TOOLS FOR VARIABLE RATE IRRIGATION

by

LORENA NUNES LACERDA

Major Professor:	George Vellidis
Committee:	Yafit Cohen
	Francesco Morari
	Cristiane Pilon
	John L. Snider

Electronic Version Approved:

Ron Walcott
Vice Provost for Graduate Education and Dean of the Graduate School
The University of Georgia
May 2021

ACKNOWLEDGEMENTS

I would like to first thank all my family, in special my mother and my father for their hard work and support. I would like to also thank all my friends from Brazil, and from the USA for all the advice, cheering and great moments that helped me through the Ph.D. Thank you to Christopher Porter for supporting me in all the difficult moments and his family for welcoming me, and to Chiara Rossi for her friendship and support as well.

I want to show my greatest gratitude to my advisor, George Vellidis for giving me a vote of confidence since the beginning. I feel lucky to have had such an incredible person and scientist as a mentor. I would like to extend my gratitude to my committee members John Snider, Cristiane Pilon, Yafit Cohen, and Francesco Morari. Thank you to Matthew Levi from Athens for the assistance with samples and his expertise.

I would like to acknowledge the US-Israel Binational Agricultural Research and Development Fund (BARD) for providing financial support. I would like to also thank the University of Georgia Crop and Soil Sciences department. This research would not be possible without the technical support of Matt Gruver, Rodney Hill, Mike Tucker, Calvin Perry and all the student workers and graduate students. Finally, thank you to the farmers that worked in collaboration with us to make this research possible.

TABLE OF CONTENTS

Page

LIST OF TABLES

Page

LIST OF FIGURES

Page

CHAPTER 1

INTRODUCTION AND LITERATURE REVIEW

1.1.Introduction

The overall goal of this dissertation was to evaluate the use of remote sensing tools to schedule irrigation in cotton. Both UAV and satellite platforms were used to obtain remotely sensed images in the visible, near infrared, and thermal infrared wave bands. These data were compared to physiological measurements of cotton that were made for three years. The work was conducted at the plot scale at the University of Georgia's Stripling Irrigation Research Park, in a 38 ha grower's field in southwestern Georgia, and the regional scale that included Georgia and Mississippi.

The dissertation research is described in three chapters (Chapters 2, 3, and 4) which follow this introductory chapter. Chapter 2 describes the research done at the plot scale, Chapter 3 describes the research done at the field scale, and Chapter 4 describes the research done at the field and regional scale. A short description of each of chapter follows below. Chapter 1 (this chapter) includes a comprehensive literature review of published research on canopy temperature, crop water stress, leaf water potential, cotton water requirements, the effects of water stress in the cotton plant, irrigation management approaches, management zones delineation, and remote sensing.

Chapter 2: Using UAV-based thermal and multispectral imagery to detect crop water status variability in cotton.

The goal of this study was to explore the potential of using UAV-based thermal and multispectral images to estimate crop water stress variability in cotton. Common indicators of crop water status such as predawn leaf water potential (LWP_{PD}) are labor and time demanding and are limited to small-scale areas (Elsayed et al. 2011). To overcome this limitation, canopy temperature data were used to calculate the crop water stress index (CWSI) and a relationship between CWSI and LWP_{PD} was developed. This study was conducted at the University of Georgia's Stripling Irrigation Research Park near Camilla, GA during the 2018 and 2020 growing seasons. A strong correlation between CWSI and LWP_{PD} was found indicating that using UAV-based canopy temperature has the potential to predict $LWP_{PD.}$ The ability to predict LWP_{PD} allows the frequent monitoring of crop stress patterns in the field throughout the season and can help improve irrigation efficiency. In addition, individual bands in the visible and near infrared regions of the electromagnetic spectrum were correlated with LWP_{PD} and stomatal conductance as an alternative to canopy temperature to estimate crop water status indicators.

Chapter 3: Correlation of UAV and satellite-derived vegetation indices with cotton physiological parameters and their use as a tool for scheduling variable rate irrigation in cotton.

The goal of this study was to evaluate whether remote sensing can be used to estimate LWP and use those estimates to delineate irrigation management zones (IMZs) in a large grower-managed cotton field. Vegetation indices (VIs) developed from UAV and satellite images were correlated with cotton physiological parameters that are indicative of plant water stress to explore the potential of creating predicted LWP and height maps. In addition, predicted plant

height maps were used to delineate new in-season IMZ maps. The yield and irrigation water use efficiency (IWUE) of variable rate irrigation (VRI) and conventional irrigation were compared. To achieve this goal, a two-year study was conducted in a large cotton field in South Georgia. Spatial and temporal variability in soil water tension (SWT), plant height, LWP, photosynthetic assimilation rate and stomatal conductance between and within IMZs were measured. All parameters showed variability suggesting that IMZs boundaries were transient. VIs predicted plant height well. Correlations between vegetation indices and LWP need further evaluation.

Chapter 4: Field scale assessment of the TsHARP technique for thermal sharpening of MODIS satellite images using VENµS and Sentinel-2 derived NDVI.

This study aimed to assess the use of the TsHARP technique to sharpen MODIS thermal images using VENµS and Sentinel-2 multispectral images. The technique was applied at the field scale in the southeastern USA. Canopy temperature is an important tool for in-season monitoring of crop water status. Although some satellite platforms offer thermal images with high temporal resolution, current thermal satellite images do not have the fine resolution needed to identify stress patterns at a field scale. Thermal sharpening techniques have been extensively explored at the scene scale, but little research has been published on their potential use at the field scale to aid in irrigation management decisions. Grower-managed cotton fields were selected in three separate locations in the states of Georgia and Mississippi to test the accuracy of field predicted surface temperatures during the 2019 growing season. Coarse resolution thermal images were sharpened to spatial resolutions of 30, 60, 120, and 240 m. We observed that images sharpened at the finer resolution of 60 and 120 m presented the most consistent results across all fields.

1.2. Literature Review

1.2.1. Canopy Temperature

The canopy temperature is an important factor affecting cotton physiological processes. In many studies, 28°C (in a range of 25-31°C) was pointed as the optimum canopy temperature for cotton growth and development and used as the threshold for automated irrigation methods (Wanjura et al. 1992; O'Shaughnessy et al. 2010; Conaty et al. 2015). Temperatures above 28°C and below 25°C cause yield reductions and decreased fiber quality. The peak in micronaire (indicator of fiber fineness and maturity) occurs around 28.8°C. Ideal leaf transpiration ratio and leaf water use efficiency can be observed at 30.8°C, while agronomic water use efficiency peaks at 29.5°C and 30.4°C (Conaty et al. 2015). Wanjura et al. (1992) stated that provided the crop is receiving the appropriate amount of water supply, the highest lint yields were reached at 28°C. When canopy temperature rises above the optimum fruit development is affected. An increase of 2°C will cause fruit shed and the development of smaller bolls. This effect tends to be more severe as the temperature gets higher (Singh et al. 2007). These results were corroborated by Conaty et al. (2012), which showed that a decrease in yield occurred when canopy temperature exceeded 28°C (Figure 1.1).

Canopy and air temperatures have been extensively studied in cotton production. Although the terms are correlated, canopy temperature and ambient temperature have slightly different values and therefore cannot be used interchangeably (Conaty et al. 2012). The plant temperature in the middle of the day is usually lower than the temperature of the air around the canopy. This difference is attributed to different factors such as plant water status, air moisture content, wind, crop size and the diurnal cycle of canopy and air temperatures. The solar radiation energy flux increases and decreases throughout the day, which in turn causes the temperature to

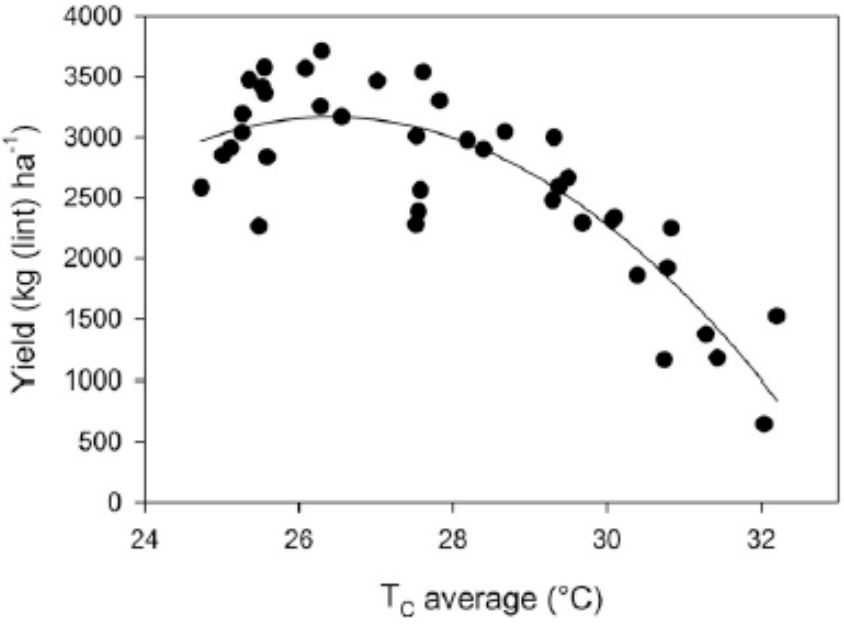

Figure 1.1. Relationship between canopy temperature (T_c) and cotton yield (Conaty et al. 2012).

rise and fall. This pattern affects both irrigated and water-stressed cotton plants, causing the gap in temperature between air and canopy to be higher or smaller depending on the dryness or humidity of the climate (Burke and Wanjura, 2010).

A study conducted by Ehrler (1973) showed that in an irrigated cotton field the difference between leaf and air temperatures decreased after irrigation and later increased as the soil water content decreased, causing water to become limited for plant uptake. In addition, a linear relationship was found between the leaf-air difference and vapor pressure deficit (VPD). VPD is defined as the difference between the existing water vapor in the air and the amount of vapor that the air can hold without condensation (Anderson 1936).

1.2.2. Crop water stress

The distinction between air and canopy temperatures is also important for the concept of crop water stress monitoring. Many authors have identified leaf temperature as a good indicator of the water status in the plant (Idso 1982; Gonzalez-Dugo et al. 2006; Conaty et al. 2015). The

premise that canopy temperature can indicate water stressed plants is based on the assumption that in well-watered plants, transpiration is at its potential rate, and the water that is being transpired evaporates, cooling the crop. As water becomes limiting transpiration is decreased, causing the temperature to increase (Jackson et al. 1988). Hence, the measurement of plant temperature can be related to crop water stress, resulting in a more reliable measurement than environment variables such as air temperature (Gonzalez-Dugo et al. 2006).

In the 1980s, two effective methods of calculating crop water stress from canopy temperature were developed (Idso et al. 1981; Jackson et al. 1981). In the first method, Jackson et al. (1981) used canopy temperature collected by infrared thermometer and data derived from energy balance equations (wet and dry bulb, air temperature and estimate of net radiation) to calculate crop water stress index (CWSI), which is an index widely used to indicate crop water stress. Idso et al. (1981) on the other hand, performed experiments involving VPD and the measurement of leaf and air temperatures difference, which enabled the development of CWSI that was independent of environmental variability (Reginato 1983). The temperature base CWSI developed can be defined as (Idso et al. 1981; Jackson et al. 1981):

$$CWSI = \frac{T_1 - T_{wet}}{T_{dry} - T_{wet}} \quad (1)$$

where T_1 is leaf temperature, T_{wet} is the lower canopy temperature limit (well-watered leaves), and T_{dry} is the higher canopy temperature limit (non-transpiring leaves).

Both methods worked well under sun and shade conditions and were effective in evidencing stress. Despite their effectiveness, a large-scale field application was not possible due to time-consuming measurements (Reginato 1983). To overcome this scalability problem current studies have adopted new procedures to calculate CWSI (Alchanatis et al. 2010; Cohen et al.

2005; Cohen et al. 2017; O'Shaughnessy et al. 2011), which will be discussed in detail in the irrigation scheduling by remotely sensed canopy temperature section.

1.2.3. Leaf Water Potential (LWP)

The water movement through the plant is driven by the difference in water potential between the shoot and the roots. Inside the plant, the water encounters frictional resistance that must be overcome. The higher the resistance, the larger is the difference in potential required to move the water. In optimal moisture conditions in which the water absorbed by the plants is equal to the water loss in the leaves, a difference between LWP (ψ_1) and root water potential is still existent. However, in conditions wherein transpiration rate is higher this difference becomes larger (Jarvis 1976). Due to this response to changes in soil and atmospheric environments, LWP is a great indicator of plant water status. Based on the following equation,

$$\psi_1 = \psi_s - R_{s1} T_f \quad (2)$$

(where ψ_s is the soil water potential, R_{s1} is the combination of soil and leaf water flow resistance, and T_f is the transpirational flux) it can be assumed that LWP varies accordingly with the soil moisture, the resistance to the water flow from soil to leaf, and the leaf transpiration. Therefore, LWP can drastically decrease in dry soil conditions and unfavorable climatic, thus being a good indicator of stress (Grimes et al. 1987).

The water potential of cotton leaves is not constant, and although it presents stability in specific periods, it varies along the day. The water potential in the leaves is in its maximum during the predawn hours (04:00 to 06:00), after which it starts to rapidly decline until reaches afternoon hours (12:00 to 15:00) wherein the LWP reaches its minimum. Cotton growth is slower during this period of minimum water potential (Cutler et al. 1977).

The variation in cotton LWP does not only affect growth rate but also the photosynthetic rate and leaf conductance (Turner et al. 1986), variation of sugar content (Cutler et al. 1977), and main stem elongation (Grimes and Yamada 1982). It has been observed that the photosynthetic rate measured in more than 12 leaves in the plant's main stem presented a decrease of 273 µmol $^{14}CO_2$ $m^{-2}s^{-1}$ with a decline of 0.2 MPa in the predawn leaf water potential during midday (Turner et al. 1986). Daily photosynthesis presented a decrease when LWP was approximately -3.5 MPa. In addition, low predawn water potential during flowering and first boll affected number of bolls, lint yield, and number of fruiting sites.

1.2.4. Cotton Water Requirements

The water requirement of cotton is not uniform throughout the growing season, and it changes according to different growth periods. In the initial stages, the water daily usage is lower compared to later stages, peaking in the middle of the season when the canopy is full and there is maximum boll load. After the first opened boll, the daily water usage starts to decline. In early stages of development, when crop water requirements may be less than 25.4 mm/week, the amount of water provided by rainfall is usually satisfactory in humid areas. In later stages of development, irrigation might be needed to help supply the water demand, which can exceed 50.8 mm/week in the middle of the season during plant growth and boll development (Fisher 2012).

1.2.5. Effects of water stress in the cotton plant

1.2.5.1. Brief Overview

Water stress is a condition in which a plant´s normal physiological processes are inhibited by a decrease in turgor pressure and water potential. The water deficit in the plant varies according to both air evaporative demand and water availability in the soil and can cause

changes in physiological and biochemical processes. The extent in which these processes are affected depend on duration and severity of drought, growth stage of the plant, and its genotype (Hsiao 1973; Loka et al. 2011). Usual effects on the plant are an increase in Reactive Oxygen Species (ROS), decrease in CO_2 uptake, obstruction of ATP synthesis, increase in photorespiration and decline in photosynthesis (Ullah et al. 2017). Less severe droughts affect the expansive growth of cotton and reduce CO_2 assimilation in the leaf (Turner et al. 1986; Mateos et al. 1991). Severe drought causes yield losses by drastically affecting boll retention (Grimes et al. 1970; Mateos et al. 1991), and significantly affects plant stature. Plants experiencing severe water shortage are shorter than well-watered plants due to a reduction in the number of main stem nodes (Pettigrew, 2004a). In addition to a lower number of main stem nodes, shorter plants also produce less Leaf Area Index (LAI), and therefore have a reduced vegetative growth.

1.2.5.2. Early crop development and vegetative growth

During early crop development, water availability significantly affects shoot and root growth dynamics. In response to a potential drought episode, the cotton plant usually prioritizes its root system as an adaptive response to avoid water deficit, causing an increase in the root/shoot ratio. The depth and growth of roots can greatly influence the plant´s capacity to withstand drought. Higher LWP and water uptake can be maintained by a deeper and denser root system, thus raising the plant´s tolerance to drought (Malik et al. 1979). However, this root elongation occurs at the expense of vegetative growth. The accumulation of photosynthate in the roots causes a reduction in shoot dry weight and a decrease in harvest index (Pace et al. 1999). Changes in shoot and root growth in early developed cotton plants were studied by Pace et al. (1999). Shoot growth was more affected and presented decreased leaf area, nodes, height, leaves

and stems' dry weight. In addition, stressed plants showed increased taproot length. However, if the drought stress persists for an extensive period, the root activity will be negatively impacted as well (Ullah et al. 2017).

The vegetative growth in early stages of development is a determining factor in the plant´s response through the remainder of the growing season (Grimes et al. 1978). In juvenile stages, the plant presents an exponential increase in the vegetative leaf growth, reaching a point at which leaf area may exceed the capacity of the roots to absorb and transport water. The high demand for water causes the plant to be very sensitive to water stress while producing new leaves (Mauney 1986). An eventual episode of moisture stress during this stage can cause a decrease in the number of flowers produced later in the reproductive stage. However, it has been suggested that exposure to water stress when the plants are 6 to 7 weeks old can be beneficial to cotton seed production (Kaur and Singh 1992).

1.2.5.3. Reproductive growth

Water stress affects nearly all stages of cotton reproductive growth, leading to a reduction in the number of blooms per unit area and thus affecting flowering (Pettigrew 2004b). Although it has been suggested that cotton is most susceptible to water stress between square initiation and first flower (Krieg 1997), in a more recent work conducted by Snowden et al. (2014), early flowering was indicated as the most sensitive stage. Physiological changes in water stressed plants during flowering and boll-forming period were the focus of Wang et al. (2016a). During these critical periods, the plants showed increased leaf senescence due to damaged cellular components and metabolism caused by high levels of reactive oxygen species (ROS). The activity of enzymes responsible for scavenging ROS such as Superoxide dismutase (SOD) was drastically decreased by water stress, which resulted in failure to control ROS levels. Other

results included limited growth and inhibition of dry matter accumulation due to a limitation in the source capacity of leaves. In an additional study, Guinn and Mauney (1984) stated that water stress decreases flowering rate. Since the number of bolls produced on each plant is proportional to cotton yield, and it is directly affected by boll retention and flowering rate, the yield will also be decreased. However, if the plant begins to receive a sufficient amount of water again, this negative effect can be attenuated by an increase in the flowering rate after a couple weeks.

1.2.5.4. Photosynthesis and photosynthetic apparatus

Photosynthesis is an important physiological process in the cotton plant, and it is highly affected by water stress. Despite the complexity of how this stress affects photosynthesis, it has been documented that photosynthetic rate can be reduced by inhibition of metabolic processes and by stomatal and non-stomatal limitations (Loka et al. 2011). Stomatal factors such as stomata closure and stomata conductance are two reaction mechanisms used by the plant that end up affecting photosynthesis in some way. Stomata closure is one of the first attempts of the plant to reduce water loss. However, while reducing water loss it unavoidably causes a decrease in intercellular CO_2 concentration (Ci). Ci is also reduced by the decreased stomata conductance that occurs during stress. With reduced intercellular CO_2 concentration, photosynthesis is limited. This limitation occurs mostly because the enzyme (Rubisco) responsible for the CO_2 assimilation has low affinity for CO_2 (Carmo-Silva et al. 2012).

During moderate drought, the decrease in Ci indicates that stomatal limitations to photosynthesis are dominant. As stomatal conductance (g_s) drops (due to water limitation) below a threshold of 100 mmol H_2O m^{-2} s^{-1} Rubisco shows a decrease in its activity. However, stomata closure is not the only mechanism occurring in the leaf. At a more severe drought, when g is at 50 mmol H_2O m^{-2} s^{-1} (Ci inflexion point) the Ci shows an increase. This increase in intercellular

CO_2 indicates that non-stomatal limitations to photosynthesis predominate at a more advanced stress stage (Flexas and Medrano, 2002).

There is ongoing discussion among the experts on whether photosynthesis is limited by drought primarily because of stomatal limitation (Carmo-Silva et al. 2012) or non-stomatal limitation (Ennahli and Earl 2005). One example of non-stomatal limitation is the decrease in ribulose bisphosphate (RuBP) that occurs due to inhibition of metabolic processes. Evidence suggests that this impairment in the plant´s metabolism begins at early stages of drought with damage to the adenosine triphosphate (ATP) synthesis. However, only when drought is severe it becomes the dominant limitation by inhibiting photosynthetic CO_2 assimilation (Flexas and Medrano 2002). Ackerson and Hebert (1981) studied cotton plants with varied water deficit levels and found that in plants adapted to the stress photosynthesis was significantly limited by non-stomatal factors. Even though adapted and non-adapted leaves presented similar leaf conductance the photosynthetic rate of adapted leaves was lower, suggesting that the decreased rate was due to other factors such as physical changes in the chloroplast caused by accumulation of starch. Corroborating with Flexas and Medrano results, Lokhande and Reddy (2014) observed that stomatal limitation was the main cause of decline in photosynthetic rate, but as the stress progressed and became more severe non-stomatal limitations played a role.

1.2.5.5. Cotton lint yield

The effects of water stress in the cotton yield has been extensively studied by numerous authors (Gerik et al. 1996; McMichael and Hesketh 1982; Pettigrew 2004b; Wang et al. 2016b). However, the degree and intensity in which the yield is affected can vary considerably. Onder et al. (2009) documented the impact of different irrigation treatments ranging from severe stress to full irrigation (in which the plants did not experience water stress at any given point). Under

severe, mild, and slight stress treatments, decreased boll weight, lint percentage, seed yield, number of sympodial branches, and leaf area index were observed. Yield reduction was also documented by McMichael and Hesketh (1982). Severe drought had great effect in yield just after planting and 44 days after planting. Plants exposed to severe stress after 73 days did not show significant reduction in yield. In non-irrigated treatment, yield reduction occurred due to decrease in number of bolls, seed, and seed and lint index. Furthermore, no significant reduction in boll size was observed in plants that did not experience drought until 44 days after planting. A more recent study showed that overall lint yield was reduced and the distribution of yield within different fruiting branches was altered (Wang et al. 2016b). Higher fruiting branches of stressed plants showed significant decrease in the number and size of bolls, seed number per boll, and boll biomass distribution.

1.2.6. Cotton water use efficiency (WUE)

Cotton water use efficiency (WUE) can be defined as the lint yield produced per unit of water received by the crop (Tennakoon and Milroy, 2003). WUE can vary according to different irrigation methods, varied water application rates, and other management practices. It can be calculated using the following equation suggested by Ibragimov et al. (2007):

$$WUE = \frac{Y}{ET} \quad (3)$$

where ET is the crop evapotranspiration, Y is the dry yield under irrigation condition, and WUE is expressed in kg m^{-3}. An alternative way of expressing the crop water use efficiency is in kg/ha/mm, which is calculated as the total lint yield (kg/ha) produced per millimeter of water that was transpired by the crop during the growing season (Tennakoon and Milroy, 2003).

Chastain et al. (2014) observed that as the growing season progressed cotton cultivated under drought conditions presented a decrease in water use efficiency. In another study, cotton was cultivated under three different irrigation conditions (fully irrigated, deficiently irrigated, and dryland) in two different years (Howell et al., 2004). In the first year WUE was higher for fully irrigated cotton (0.194 kg m^{-3}), and the lowest efficiency (0.092 kg $m^{-}3$) resulted from dryland cotton. In the following year plants under deficit irrigation presented the highest WUE (0.219 kg m^{-3}), yet the lowest value (0.103 kg $m^{-}3$) was again from dryland plants. Yazar et al. (2002) conducted an experiment with low-energy precision application (LEPA) and trickle-irrigation with 4 (100, 75, 50, and 25%) and 3 (100, 67, and 33%) different levels of irrigation respectively. The highest efficiency (0.741 kg m^{-3}) among all resulted from the treatment with a trickle irrigation system (67% of full irrigation) with a 6-day interval between irrigation events. For the LEPA system, the highest WUE was observed in plants that received 25% of full irrigation. For both systems, WUE decreased as water use increased.

New approaches to increase water use efficiency involve the use of deficit irrigation scheduling. Baker et al (2015) compared cotton WUE under CWSI and stress time (ST) irrigation triggering methods. Both representing stress indices based on canopy temperature. Overall, cotton lint yield was higher with increased water use by the plant, but water use efficiency peaked at lower water use for both CWSI (439mm) and ST (494mm) suggesting that irrigating cotton with less water than the amount needed for maximum yield can optimize WUE.

1.2.7. Irrigation management approaches

1.2.7.1. University of Georgia (UGA) checkbook method

Irrigation scheduling is a management practice used to avoid stress episodes in critical growth stages by determining irrigation timing and rate of water application (O'Shaughnessy and

Evett, 2010). The time in which the crop will be irrigated is determined by an environmental or plant-based factor that serves as a trigger. Conventionally, environmental triggers such as soil moisture status, presented in terms of water content or water potential, and soil water balance calculated using estimates of evapotranspiration and crop water requirements are more commonly used to schedule irrigation (Jones 2004).

The University of Georgia (UGA) checkbook is an irrigation method based on historical average evapotranspiration data collected over 16 years in the state of Georgia. The recommendations from UGA extension are based on the amount of water needed during each week of cotton's life cycle (Table 1.1). This weekly target is met with rainfall and supplemental irrigation (Georgia Cotton Production Guide 2018; Vellidis et al. 2016b).

The checkbook method has been successfully used to achieve higher yields in Georgia, yet other methods have outperformed it in yield and water use efficiency (Chastain et al. 2016b). Vellidis et al. (2016b) observed higher yields and WUE using SmartIrrigation Cotton App, and in UGA Smart Sensor Array (SSA) plots than in plots irrigated by the checkbook approach in

Table 1.1. Irrigation schedule suggested for cotton in Georgia (Cotton Production Guide 2018).

Crop Stage	**Centimeters/Week**	**Centimeters/Day**
Week beginning at 1st bloom	2.5	0.38
2nd week after 1st bloom	3.8	0.56
3rd week after 1st bloom	5.1	0.76
4th week after 1st bloom	5.1	0.76
5th week after 1st bloom	3.8	0.56
6th week after 1st bloom	3.8	0.56
7th week and beyond	2.5	0.38

both conventional and conservation tillage. Similar results were found by Vellidis et al. (2016a) whereas the checkbook method had lower yields than Cotton App and UGA SSA in three different years regardless of tillage method. Additionally, in two of the three years WUE of the checkbook method was lower than for the two other approaches.

1.2.7.2. Predawn and minimum leaf water potential

Plant physiological responses are directly related to changes in water status in plant tissues, rather than changes in soil water potential. This places a potential limitation on some environmental triggers that depend on soil-water relationship, thus favoring the use of plant-based approaches (Jones 2004). As previously noted, LWP is a good indicator of plant water need and has been often used for irrigation scheduling due to its relationship with many plant physiological processes. Minimum and predawn are two variations of LWP and were defined earlier. Because they represent two critical moments of the day (time in which LWP is minimum and drought stress is maximum, and time of maximum LWP respectively), their use can greatly affect irrigation management decisions (Snider et al. 2016).

Minimum LWP is highly dependent on the weather, which presents a disadvantage in its use when compared to predawn. Variations in vapor pressure deficit, cloud cover, and changes in temperature are often followed by changes in minimum LWP (Jones 1900; Snider et al. 2016). Furthermore, minimum LWP in plants that show isohydric behavior such as cotton is not a very sensitive stress indicator, since these plants tend to maintain a constant water status even with changes in transpiration rate (Fernandez 2017). Nevertheless, in regions that do not present significant variation on day-to-day temperature and cloud cover minimum LWP was shown to be a reliable water stress indicator and thus effective for irrigation scheduling. In California, minimum leaf water potential showed a relationship with vegetative and fiber growth for cotton

grown in different soil types. Root extension and optimum yields were achieved when irrigation was scheduled at minimum LWP ranging from -1.8MPa to -2MPa (Grimes and Yamada 1982).

Differently from midday LWP, predawn measurements have been successfully used to control irrigation in different crops and regions. Predawn LWP measured with a Scholander-type pressure chamber was used in peach orchards in Portugal to determine irrigation using a deficit irrigation approach. A relationship between relative evapotranspiration and predawn LWP was developed, showing high relation during water stress conditions. This relationship allowed irrigation to be scheduled in different systems by using only predawn LWP measurements (Paço et al. 2013). Predawn LWP was also shown as a superior indicator for irrigation scheduling in plum trees. If used to modify irrigation rates, higher fruit weight could be observed since predawn LWP showed high relation with fruit weight in two different years, thus proving to be a great indicator of fruit weight during harvest (Intrigliolo and Castel, 2006). In cotton, a recent study conducted by Chastain et al. (2016b) tested effectiveness of predawn LWP to increase WUE in drip-irrigated cotton in the southeastern United States. By using a season-long irrigation threshold of -0.5MPa lint yield and water productivity were maximized, and irrigation applied was lower compared to other common methods such as checkbook. Additionally, a strong nonlinear relationship between predawn LWP and CWSI was developed (Figure 1.2), which can greatly aid in automated plant-based irrigation systems.

1.2.7.3. Cotton Smart Irrigation App

Irrigation scheduling using smartphone apps are often based on evapotranspiration (ET). Numerous factors affect plant evapotranspiration including crop characteristics, management, weather parameters, and other environmental aspects. Because weather is a critical factor ET calculation is often based on meteorological data collected in real-time together with the FAO

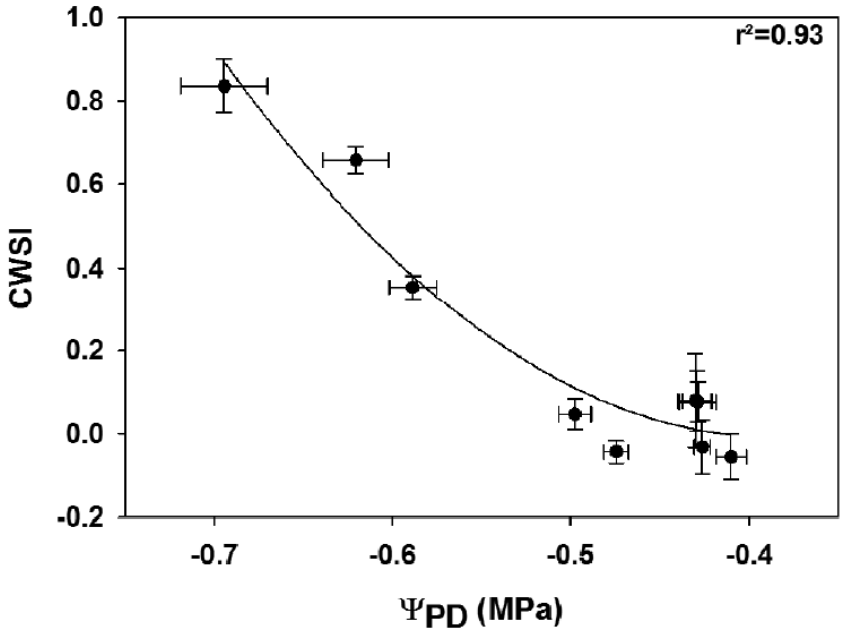

Figure 1.2. Relationship between predawn LWP and CWSI (Chastain et al. 2016b).

Penman-Monteith equation (Migliaccio et al. 2015; Allen et al. 1998). To obtain crop-specific ET (ET_c), crop coefficient (K_c) and reference ET (ET_o) are used (eq. 3). However, K_c (Jensen 1968) is not constant during all the plant's life cycle. During the early phenological stages K_c values are small reaching 1.0 or more (when the water demand is at its maximum) and increases in the later stages when crop reaches maturity and starts to senesce (Vellidis et al. 2016a).

$$ET_c = ET_o \times K_c \tag{3}$$

The cotton app is an easy-to-use interface that outputs information to help in irrigation decisions rather than delivering irrigation recommendations like other irrigation apps (Migliaccio et al. 2015). To develop an initial K_c curve specific for cotton produced in southern Georgia and northern Florida, information from other studies were utilized. A posterior calibration of the curve was performed with plot and field experiments. To estimate the amount of water used by the crop a model was used to calculate ET_c. K_c used in the model changed according to

accumulated heat units, which can be expressed in terms of growing degree days (GDD). To account for these changes GDD was calculated using Eq. 4. In addition to ET_c, other data such as meteorological data from weather stations, soil parameters, and crop phenology were used to estimate root zone soil water deficits (RZSWD) and percent of total available soil water. The users then receive notifications when RZSWD is 40 to 50% higher than total available water in the soil. This approach showed great performance when compared to other irrigation scheduling methods (Vellidis et al. 2014; Vellidis et al. 2016a). Yields resulting from cotton app irrigation recommendations were similar to scheduling tools that use soil moisture sensors and higher when compared to checkbook method yields (Vellidis et al. 2015).

$$GDD = \frac{Tmax + Tmin}{2} - T_{base} \tag{4}$$

1.2.7.4. Variable rate irrigation (VRI)

Center pivot irrigation plays a major role in irrigation in the state of Georgia. However, conventional pivot systems are unable to apply varied water application rates, thus not meeting plant needs on different soil types. They are also not capable of avoiding application in non-cropped areas. Due to aforementioned limitations problems of over and under application of water are commonly seen in pivot irrigation system and has become a concern for the public and researchers (Perry and Pocknee 2003). Since water is a major determinant of crop yield, irrigation uniformity has been a common interest amongst farmers (Yule et al. 2008). Furthermore, fields present high soil variability, slope variability, and water holding capacity and therefore site-specific irrigation can lead to significant water savings (Vellidis et al. 2013).

In 2001, researchers from the University of Georgia Precision Agriculture Team developed the VRI system (Vellidis et al. 2016c). The system's principle lies in varying

application rates by controlling the pivot speed and by cycling the sprinklers on and off. The number of sprinkler groups is based on the level of resolution wanted by the farmer, varying from 3 to 10 groups. A grid with a 2 to 10-degree arc is represented by each group of sprinklers, in which the number of degrees also vary according to the desired resolution. The application rate respective to each grid is set as a percentage of normal application rate and can range from 0% to 200% (Vellidis et al. 2013).

The VRI system requires a series of steps to perform. The field is first divided into management zones that are then used to create application maps defined using desktop computer software. The maps are loaded into the VRI controller. A GPS system is used to determine the pivot mainline angle and position. The sprinklers' application rates are then set based on the control map (Perry and Pocknee 2003). Different approaches have been used to define control maps' zones. Yule et al. (2008) mapped soil water availability using soil electrical conductivity (Ec) to calculate soil moisture status and schedule irrigation accordingly. A second approach presented by Liakos et al. (2015) delineated the zones by using aerial images, ground measurements of soil Ec, and the United States Department of Agriculture Natural Resources Conservation Service (NRCS) web soil survey.

The VRI system has definitely been an important improvement in irrigation scheduling methods. However, with static prescription maps the system is not able to respond to environmental variables that affect crop growth rate and soil moisture conditions. A new approach presented by Vellidis et al. (2016c) addressed this limitation by proposing a dynamic VRI system, in which the prescription maps would be based on a combined use of real-time soil moisture sensing network and an irrigation scheduling decision support tool (Liakos et al. 2015). Soil moisture sensors were installed in each management zone expressing results in terms of soil

water tension (SWT). The average SWT from the nodes was then used to calculate volume of irrigation. The VRI system results in a peanut field were promising. With a total amount of water applied (76 mm) much lower than the conventional irrigation (109 mm), and achieving similar yields (5543 $Kg.ha^{-1}$, 5552 $Kg.ha^{-1}$, VRI and conventional respectively), the VRI system resulted in WUE 43% higher than conventional methods.

UGA Smart Sensor Array (SSA)

The first prototype of the UGA SSA node for irrigation scheduling was developed in 2008. The node consists of three Watermark® granular resistive-type soil moisture sensors, thermocouples, circuit board, and an active radio frequency (RF) transmitter (Vellidis et al. 2008). The depth of Watermark® sensors in the node varies according to the crop. For cotton, the sensors are installed at 20, 40, and 60 cm below soil surface. The radio transmitter used is a low-power 2.4 GHz radio module that transmits the sensor data in hourly intervals to a base station located in the center of each field. The data is stored in a solar-powered netbook computer and is transmitted to an FTP server via cellular modem every hour. To avoid any problems in the data transmission process due to blocking of signal pathways or malfunctioning of nodes, a wireless mesh network is used for communication between the nodes. Data from one node to another is passed through an RF transmitter, which also plays the role of a repeater. In the face of a problem, the software reconfigures the signal route to maintain data acquisition from the network (Vellidis et al. 2016c).

As mentioned, the data from the sensors is sent by the base station to an FTP server. This server stores all the raw data from the soil moisture sensors. Additionally, a commercial server is used for visual representation of the data, wherein the data is manipulated, processed, classified and stored. The commercial server also serves as an interface with users through a dedicated

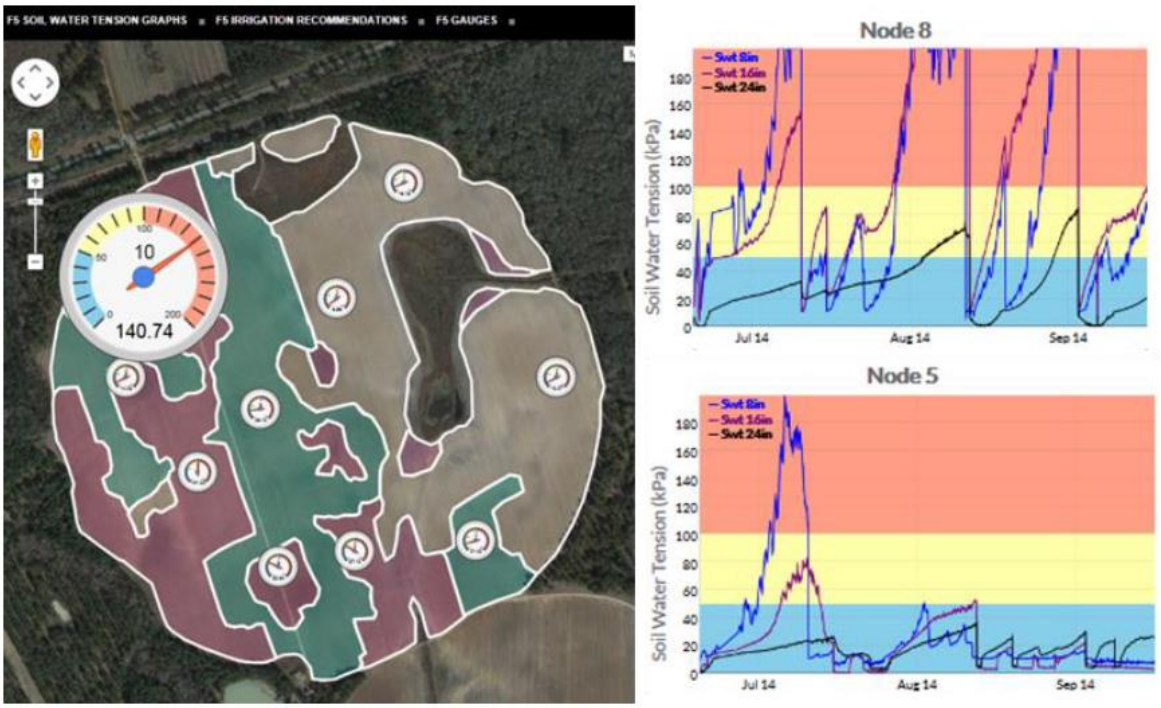

Figure 1.3. Two different ways of representing soil water tension in the web-based interface (Vellidis et al. 2016c).

website (www.ugassa.org). This web-based interface enables the visualization of soil moisture data in two different ways (color-coded gauges and soil water tension curves) (Figure 1.3) that were created by using Personal Home Page (PHP) and Javascript programming languages (Liakos et al. 2015; Vellidis et al. 2016c).

Decision support tool (DST)

One additional feature offered by the web-based user interface is irrigation recommendations for each IMZ. Liang et al. (2016) modified the original Van Genuchten model (van Ganuchten, 1980) to convert soil matric potential (or SWT) to volumetric water content (VWC) (Eq.5). The relationship between the two variables is characterized by soil water retention curves (SWRC). As the soil VWC decreases from water saturation to permanent wilting point (PWP), the SWT increases in different rates (Reynolds et al. 2009). At the beginning, larger pores dry out quickly (since the water is being weakly held by capillary forces)

and SWT shows a slow increase until it reaches the inflection point. At the inflection point smaller pores start to dry. Water in smaller pores is strongly held; therefore, the SWT will start to increase more rapidly (Figure 1.4). The inflection point will vary accordingly to soil texture, which strongly influences the Van Genuchten model. From the curve, it is also possible to estimate VWC at the PWP and at field capacity, which is extremely important for prescribing irrigation (Liang et al. 2016).

$$\Theta(\psi) = \Theta_r + [(\Theta_s - \Theta_r)/[1 + (\alpha|\psi|^n)]^{1-1/n} \quad (5)$$

Where, $\Theta(\psi)$ is the water retention curve ($1^3 1^{-3}$), $|\psi|$ is suction pressure ([1]) or cm of water, Θ_s is the saturated water content ($1^3 1^{-3}$), Θ_r is the residual water content ($1^3 1^{-3}$), α is related to the inverse of the air entry suction, a>0 ($[1^{-1}]$) or cm^{-1}, and n is a measure of the pore size distribution.

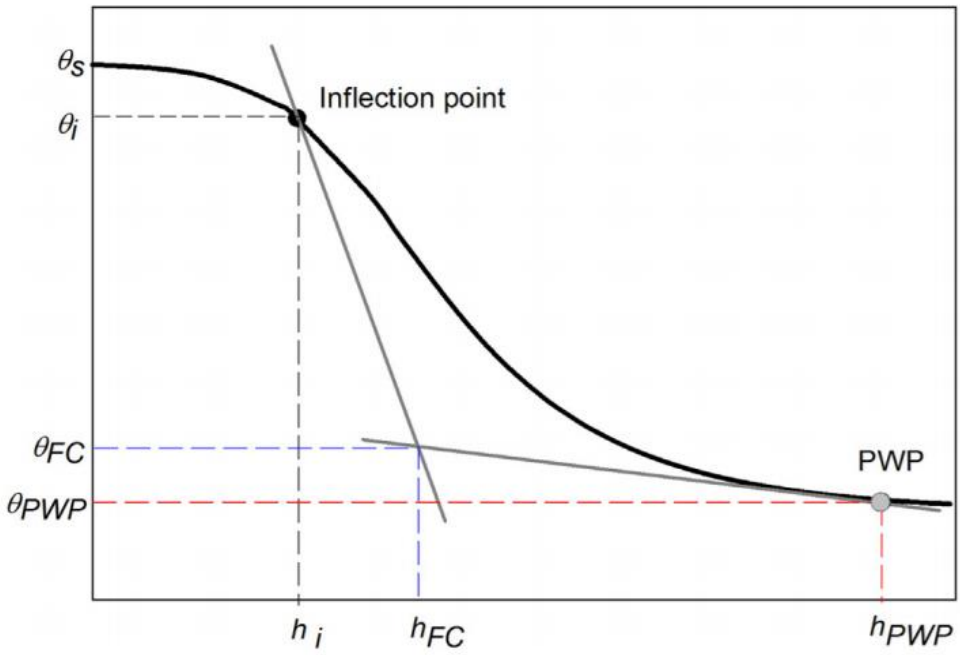

Figure 1.4. Identification of field capacity with the Van Genuchten model tangent lines (Liang et al. 2016).

The modified Van Genuchten model has been used to prescribe irrigation needed to bring soil profile of IMZs to field capacity or percentage of field capacity (Vellidis et al. 2016c). Average SWT data measured hourly between 07:00 and 09:00 of all nodes within an IMZ is used in the model to calculate volume of irrigation. SWT of each node is a result of a weighted average between values measured in each one of the three Watermark® sensors. Weighted values for cotton are shown in Equation 7. Irrigation recommendation was successfully prescribed and readily available for farmers on a daily basis (Liakos et al. 2015).

$$(0.5)(kPa\ at\ 20\ cm) + (03)(kPa\ at\ 40\ cm) + (0.2)(kPa\ at\ 60\ cm) \quad (7)$$

Remote sensed canopy temperature

Recent advances in thermal imagery enabled the collection of surface temperature for large areas (Cohen et al. 2005). This presents a potential solution to the scalability problem in the use of canopy temperature based CWSI to assess crop water status (Alchanatis et al. 2010). The ease in canopy temperature data collection at large scale made possible the direct and indirect employment of CWSI in irrigation scheduling. Shae et al. (1999) directly controlled irrigation using CWSI by establishing threshold values, while Rosenberg et al. (2014) explored an indirect approach by using the CWSI/LWP relationship. Additional advantages of remotely sensed images include its reliability and non-invasive nature (Alchanatis et al. 2010).

It has been demonstrated that thermal imaging can be successfully used to calculate LWP as an alternative to direct measurements. LWP maps estimated from CWSI were found adequate to represent crop water status. High variability in water potential was observed, and better distinction of different irrigation amounts was shown when compared to LWP derived from leaf temperature (Cohen et al. 2005). Moreover, LWP maps can be used in the delineation of LWP

based management zones. Despite all benefits of remotely sensed CWSI/LWP, farmers still rely on LWP point measurements to assess water status in large cotton fields. In this method, only a few leaves are sampled, and they do not always represent the spatial variability of the whole area (Cohen et al. 2005; Cohen et al. 2015).

Irrigation scheduling based on thermal images heavily relies on regression models of LWP against CWSI generated after extensive research on the CWSI/LWP relationship (Cohen et al. 2015; Chastain et al. 2016b; Cohen et al. 2017). Although different methodologies have been used in the conversion process of thermal images into LWP maps, the same premise is shared. The first step is to extract pixel canopy temperature. Afterwards, the pixel temperature is used in the equation suggested by Idso et al. (1981) and CWSI is calculated. LWP values are then estimated from CWSI values by pixel (Rosenberg et al. 2014).

1) Canopy temperature extraction

An empirical methodology for temperature extraction that can be used for field crops was developed by Meron et al. (2010). This methodology is based in two assumptions. Assumption 1 states that canopy and soil-related pixels in a thermal image are separated by upper and lower thresholds related to air temperature using Eq.8:

$$(T_{air} - 10) < T_{cr} < (T_{air} + 7) \tag{8}$$

where T_{air} is air temperature (°C) and T_{cr} is the temperature of canopy-related pixels in a thermal image. The second assumption is that the canopy temperature is represented by an average temperature of the coldest 33% of canopy-related pixels. The image histogram ranged from 19°C to 45.5°C in 0.1°C intervals. Using the class conditional temperature histogram of the canopy-related pixels $f(\mathrm{T})$, T_{canopy} can be calculated using Eq.9:

$$T_{canopy} = \frac{\sum_{i=1}^{0.33n} T_{cr} * f}{\sum_{i=1}^{0.33n} f_i} \quad (9)$$

where T_{canopy} (°C) is the canopy temperature, f is the number of pixels in each *cr* class of the histogram, and *n* is the number of canopy pixels resulted from Eq.8.

2) Calculation of CWSI

Extracted canopy temperature, and two reference values are used to calculate CWSI, based on Eq.1. The two reference values represent the minimum temperature of a fully transpiring leaf (well-watered crop), and the maximum temperature of a non-transpiring leaf (stressed crop) (Cohen et al. 2015; Meron et al. 2010; Rosenberg et al. 2014). Various empirical, theoretical, and statistical forms of wet and dry baselines have been proposed, and a summary of them can be seen in Table 1.2. For small scale, all forms have been used to calculate both baselines, while for large scales dry baseline has been only empirically calculated and wet baseline empirically, theoretically and statistically (Cohen et al. 2017).

Empirical baselines

Empirical wet baselines (non-water stressed) were found to be strongly related to specific climate conditions and crops. Alfalfa, soybean and squash presented linear relationships between T_F (foliar temperature) minus T_a (air temperature) and VPD, yet the relationships were different and therefore unique to each crop. It was also observed that when a state of potential evaporation exists the air VPD was sufficient to specify the differential of foliar-air temperature (Idso et al. 1981). Because empirical dry and wet baselines are so dependent on VPD several non-water stress baselines are required to determine CWSI values, as can be observed in Acala cotton (Jackson et al. 1981).

Table 1.2. Wet and dry baselines used to calculate CWSI (modified from Cohen et al. 2017).

Baseline type		How is it calculated or measured?	Used for small scale	Used for large scale
Wet	Empirical	Air temperature + X °C where X is an empirical estimate dependent on VPD[a]	Irmak et al. (2000), Jackson (1991), Erdem et al. (2005)	Bellvert et al. (2014)
	Theoretical 1	Temperature calculation using energy balance equation (suggested by Jones 1992)	Jones (1999), Alchanatis et al. (2010)	
	Theoretical 2	Temperature calculation using energy balance equation (suggested by Monteith and Unsworth 1990)	Rud et al. (2014)	O'Shaughnessy et al. (2011)
	Measured: bio-indicator	Temperature measurement of a wet real leaf	Jones (1999)	
	Measured: artificial surface	Temperature measurement of a wet artificial reference surface	Cohen et al. (2005), Alchanatis et al. (2010), Meron et al. (2010)	
	Statistical/bio-indicator	Average temperature of the coolest 5-10% of the canopy pixels and the like	Alchanatis et al. (2010), Rud et al. (2014)	Gonzalez-Dugo et al. (2013)
Dry	Empirical	Air temperature + X °C where X is an empirical estimate[a]. The canopy-air difference is unique for each crop in each region	Jackson (1991), Irmak et al. (2000), Cohen et al. (2005), Alchanatis et al. (2010)	O'Shaughnessy et al. (2011), Gonzalez-Dugo (2013), Meron et al. (2010)
	Theoretical	Temperature calculation using energy balance equations (suggested by Jones 1992)	Jones (1999)	
	Measured: bio indicator	Temperature measurement of a real leaf covered with petroleum jelly	Jones (1999)	

Irmak et al. (2000) calculated CWSI for corn using measured lower and upper baselines by following methodology suggested by Idso et al. (1981), in which the difference between canopy temperature (T_c) and T_a in degree Celsius was related to VPD (kPa) (Figure 1.5). The upper baseline represented $T_c - T_a$ for plants that showed severe stress. Average T_c - T_a values

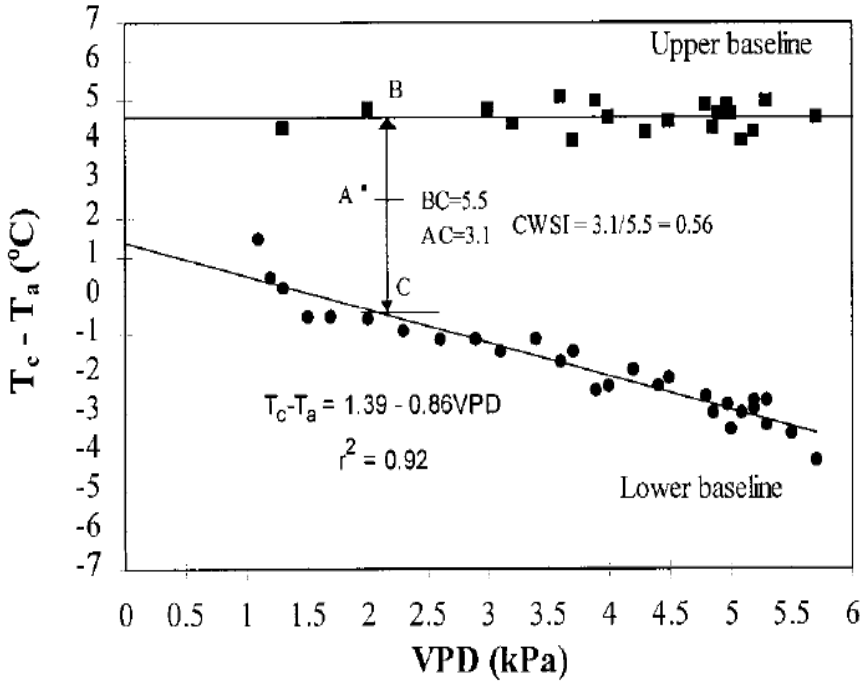

Figure 1.5. One day example of the relationship between T_c - T_a and VPD (Irmak et al., 2000).

were calculated to create the upper baseline. Although the upper baseline values varied between 4 and 5.1°C, it was assumed relatively constant at about +4.6°C. Cohen et al. (2005) used results reported to estimate the upper boundary (T_{dry}) by adding 5°C to air temperature measured with a dry bulb. In a commercial fruit tree orchard T_a *+2* was used for *Prunus* sp. and T_a*+4* for *Citrus* sp. (Gonzalez-Dugo et al. 2013).

Similar to upper baseline, lower baseline has also been empirically estimated by adding measured canopy temperature to the air temperature measured with a wet bulb. Jackson et al. (1991) developed non-water-stressed baseline in two different cotton growth stages (early season and late season) by simultaneously measuring leaf temperature and wet bulb values over several days. Erdem et al. (2005) estimated wet baseline in potatoes with canopy temperature data collected with infrared thermometry in furrow and drip irrigated treatments one day after an irrigation event. At a larger scale, Bellvert et al. (2015) used infrared temperature sensor (IRTS)

connected to data loggers installed in well-watered grapevines and calculated average canopy temperature every 30 minutes. Non-water-stressed baselines were developed for four different phenological stages (from anthesis to fruit set, fruit to veraison, veraison until harvest and harvest until postharvest).

Theoretical baselines

CWSI values that are gotten from a theoretical approach rely solely on meteorological measurements and calculation of both baselines, which requires advanced meteorological stations in close proximity to the point of measurement. The closer the station, the higher the chance of accurate input to the balance energy model suggested by Jones (1992). This dependence on meteorological measurements can present a limitation to this approach. Additional disadvantages are related to the energy balance model assumption that there is an equilibrium between a leaf and its surroundings, which may not hold true (Alchanatis et al. 2010). Theoretical wet and dry baselines based on energy balance equation suggested by Jones (1992) and Jones (1999) respectively, were used by Alchanatis et al. (2010) and derived from the following equations:

$$T_{wet} = T_a + \frac{r_{HR} r_{aW} \gamma R_{ni}}{\rho_a c_p [\gamma (r_{aW}) + \Delta r_{HR}]} - \frac{r_{HR} VPD}{\gamma r_{aW} + \Delta r_{HR}} \quad (10)$$

where T_a is air temperature, r_{HR} is the resistance to radiative heat transfer that is based on leaf dimension of 0.1 m, r_{aW} is the water vapor boundary layer resistance, γ is the psychrometric constant, R_{ni} is net radiation, ρ_a is the air density, c_p is the specific heat of air and Δ is the saturation vapor pressure curve slope.

$$T_{dry} = T_a + \frac{r_{HR} R_{ni}}{\rho_a c_p}$$

(11)

A second energy balance equation has been suggested by Monteith and Unsworth (1990). This approach has only been used to estimate wet baselines. In large scale, it was used in soybean and cotton (O'Shaughnessy et al. 2011) and in small scale in potato fields (Rud et al. 2014). This alternative estimation of wet baselines can be estimated as follow:

$$T_W \approx T_a - \frac{e_s(T_a) - e_a}{\Delta + \gamma}$$

(12)

where T_a is air temperature (°C), e_s is saturated vapor pressure (Pa) at the air temperature, e_a is actual vapor pressure (Pa), Δ is slope (Pa °C^{-1}) of the saturated vapor pressure vs the temperature curve evaluated at air temperature, and γ is the psychrometric constant (Pa°C^{-1}).

Statistical baselines

Lower baselines can also be estimated using a statistical or bio-indicator approach, which assumes that there are well or over irrigated areas in a field (Rud et al. 2014). The plant temperature measurements are made with a sensor such as a thermal camera, and the average of the coolest or lowest 5 or 10% of canopy pixels in the image are used as the wet baseline. This approach is regarded as farmer-friendly because of its minimum requirements, since a nearby meteorological station is needed only for air temperature measurement (Cohen et al. 2017). Although it was successfully used in commercial orchard fields (Gonzalez-Dugo et al. 2013) and recommended as a measure of wet baseline for cotton (Cohen et al. 2017) this methodology presents some weaknesses. Rud et al. (2014) observed that CWSI values originating from statistical methodology were lower in well-irrigated treatments when compared to empirical and theoretical. Later in the season (99 DAP) the difference in statistical and theoretical T_{wet} was as high as 3.6°C. Results indicated that statistical methodology may be more suitable for large

fields rather than experimental plots. Higher chance of biased calculation of T_{wet} is expected for small scale since the probability of having over-irrigated sub-areas is lower in smaller fields.

3) Conversion of CWSI into LWP

Differences in climate conditions have led to the development of region-specific relationships between CWSI and LWP. A strong non-linear relationship in cotton for southern USA humid conditions was found between CWSI and predawn LWP measurements (Chastain et al. 2016b), whilst for Israeli conditions, Cohen et al (2015) observed a linear relationship between LWP and CWSI derived from high-resolution thermal images. Despite its specificities, all models exhibit the same inverse pattern in which CWSI increases as LWP decreases (Chastain et al. 2016b; Cohen et al. 2015). Although this association is stable, it can change in different growth stages of the plant (Jackson 1991).

In a recent study, a multi-year CWSI-LWP relationship was used to convert thermal images of cotton experimental plots into LWP maps (Cohen et al. 2017). The following equation was used:

$$LWP[MPa] = -1.77CWSI - 1.28 - K \quad (13)$$

where K represents a transformation constant between LWP measurement methodology and other methodologies. In this study the transformation constant of K=0.4 MPa was used. Pixel LWP values derived from the equation were assigned to one of four different water status classes (Table 2). Results showed high correlation between calculated and measured LWP. Although over-estimation was observed in calculated LWP values, methodology suggested by Meron et al. (2010), in which 33% of coldest canopy-related pixels were averaged attenuated soil effects and thus reduced the over-estimation problem.

Table 1.3. Water status classes in cotton based on LWP values (Cohen et al. 2017).

Class	Water status description	LWP range (MPa)
1	Over-irrigated (Oir)	[−1.45] ≥ LWP > [RecLWP + RMSE]
2	Well irrigated (WI)	[RecLWP + RMSE] ≥ LWP > [RecLWP−RMSE]
3—20–50 DAF[a]	Low water stress (LWS)	[RecLWP−RMSE] ≥ LWP > [−2.4]
3—50–70 DAF	Low water stress (LWS)	[RecLWP−RMSE] ≥ LWP > [−3.0]
4—20–50 DAF	Medium to sever water stress (MSWS)	[−2.4] ≥ LWP
4—50–70 DAF	Medium to sever water stress (MSWS)	[−3.0] ≥ LWP

[a] Days after flowering onset

1.2.8. Management zones (MZs) delineation

Dividing a large area in smaller homogenous subareas for site-specific management is the basic premise of precision agriculture (PA) (Brock et al. 2005). Despite its importance, management zones (MZs) delineation is still a challenge for PA applications due to the many factors (soil, biotic and climate) involved in determining crop yield. Dynamic interactions between these factors add even more complexity (Fridgen et al. 2004) causing significant field spatial variability within each year (Blackmore et al. 2003) and a year to year variation in the optimum number of MZs (Fraisse et al. 2001). In the process of MZ delineation, authors usually are led to respond to three basic questionings pertinent for identification of representative zones. The first question is what data should be used to delineate the zones within a field; the second is what classification method is the best to process this data into unique zones; and the final question concerns the appropriate number in which the field should be divided (Fridgen et al. 2004).

1.2.8.1. Data sets

Management zones for variable rate application can be delineated based on a variety of data sets such as individual plant and soil properties, soil-plant relationship, and multiple properties simultaneously. Blackmore et al. (2003) created spatial and temporal trend maps of different grain crops' yield data collected between the years of 1995 and 2000 for four different fields. Yield map patterns of different years were then used to predict yield of future years. Results showed that predicted yield did not correlate with actual yield, but the trend maps seemed to be a promising tool in identifying homogenous MZs. Crop performance was also used by Brock et al. (2005) to delineate zones for a corn-soybean rotation, and a spatial association comparison was made between yield-based MZs and published soil survey map units. It was found that MZs showing lower yield data were significantly associated with high sloping and eroded areas, while high yielding MZs were associated with wetter areas, thus showing great potential in identifying within field variability.

Morari et al. (2009) used association between soil electrical conductivity (EC) and physical soil properties to delineate potential MZs. Clay and silt particles showed a positive relationship with EC, while coarser particles such as sand and gravel were negatively associated aiding in the identification of soil patterns and its division in different zones. In a more recent work, Scudiero et al. (2013) combined geospatial apparent soil electrical conductivity (EC_a) and reflectance measurements of bare soil to identify spatial variability of soil properties. Both variables combined can be used to identify areas of homogeneous soil fertility and help in site-specific management.

The delineation of management zones for site-specific irrigation is highly affected by soil hydraulic and physical properties (Haghverdi et al., 2015). These properties control plant-

available water, affecting irrigation scheduling, and therefore are often used to delineate IMZs. Zones for precision irrigation were reasonably delineated by using geostatistical analysis to correlate spatial variability of field moisture capacity, saturated moisture content, wilting point, and dry bulk density (Jiang et al. 2011a). A subsequent study highlighted the importance of soil properties for irrigation management even in leveled fields with 1% of slope (Longchamps et al. 2015). Soil water content presented spatial variability with long ranges and temporal dependency, evidencing the need of unique zones delineation in a field that visually does not seem to have significant variability.

The most commonly used method to obtain soil and crop stage information is the selection of few random locations in the field to be sampled (Chiericati et al., 2007). This method requires intensive labor and is time consuming, which can become an expensive practice. Electromagnetic induction (EMI) scanner is a sensor equipped with a small transmitter coil capable of estimating large volumes of EC_a data by measuring ratio between two different magnetic fields (magnetic field generated by EMI, and magnetic field generated by induced current) (James et al. 2003). The combination of EMI and vegetation indices derived from multispectral remote sensing data has been shown as a possible substitute method for IMZs delineation that is both more efficient and cost-effective than traditional field sampling (Chiericati et al. 2007).

All above-mentioned work focused on the delineation of static zones. MZs were delineated once and boundaries were static during the growing season, therefore not responding to within season changes in soil and plant water status. Recent work using wireless network of infrared thermometers developed dynamic prescription maps system for irrigation scheduling in cotton, in which IMZ boundaries changed according to plant feedback on crop water stress

(O'Shaughnessy et al. 2015). Further research has evidenced the need for irrigation management zones with dynamic boundaries (Cohen et al. 2017). LWP maps created from remotely sensed canopy temperature showed great variability throughout the season. Due to the unpredictable effect of different environmental factors in the water level in the plant, LWP change patterns cannot be predicted. Hence, dynamic prescription maps can greatly improve VRI systems.

1.2.8.2. Methodology

Many authors have successfully delineated MZs that represented variability in the field, yet there is a lack of simple protocols on how to delineate zones in a practical way. This presented a barrier to the widespread adoption for this management approach (Brock et al. 2005). Procedures often involve statistical techniques that require time to learn and are not always well suited for producers. Although many software programs are equipped with tools capable of transforming spatial data into management zones, there was still a need for an easy-to-use software that could help in the decision-making process (Fridgen et al. 2004).

The most commonly used method to delineate MZs involves the application of unsupervised clustering techniques (Haghverdi et al. 2015). In unsupervised clustering, data is grouped into different classes based on their inherent structure. In methodology described by Fraisse et al. (2001), the principal component analysis (PCA) and ISODATA (Iterative Self-Organizing Data Analysis Technique) clustering algorithms were used in combination with Unscrambler software to divide fields in different MZs. The most important variables were identified with the help of PCA and then used in the unsupervised classification method to divide fields into 2, 3, 4, 5 and 6 management zones. Recently, Haghverdi et al. (2015) compared three different unsupervised clustering techniques (k-means, ISODATA and gaussian mixture model) in combination with two other software tools (Matlab and ArcGIS) and a new zoning

methodology based on integer linear programming (ILP). ILP was designed for the center pivot system with limited speed control capability. Up to 40% of variance in water content in the field was explained by this new approach, while the clustering methods efficiently delineated homogenous zones based on soil hydraulic properties.

Management Zone Analyst (MZA)

In 2004, a new software for management zone delineation was developed by Fridgen et al., and it has become vastly used (Brock et al. 2005; Jiang et al. 2011a; Jiang et al. 2011b). Different from other Geographic Information Systems (GIS) software, the MZA was designed specifically for spatial zoning, which makes it more user-friendly (Jiang et al. 2011a). Another advantage of this new software is its capability to not only assign field information into potential zones, but also output a range of cluster numbers that indicates the appropriate number of zones that should be delineated (Fridgen et al. 2004). This is a great advance from methodologies, because it does not require the user to decide the optimum number of zones.

The software uses an unsupervised clustering algorithm called fuzzy *c*-means (also known as fuzzy *k*-means) that is based on the sum of square distance of all data points in a cluster domain to its centroid (Fridgen et al. 2004). The algorithm assigns points to different clusters after an iterative process similar to ISODATA and controls the extent in which memberships are shared between classes. This algorithm, selected to meet the need for clustering inputs, is based on continuum soil and landscape information. Supervised clustering techniques were excluded from MZA because it requires the user to have prior knowledge of areas that will be selected to train the algorithm.

To determine the optimum number of zones based on descriptive statistics and unsupervised fuzzy classification, the MZA software provides users with two performance

indices (Jiang et al. 2011a). The first is the fuzziness performance index (FPI), which measures the degree of separation between data matrix fuzzy *c*-partitions and is defined as:

$$FPI = 1 - \frac{c}{(c-1)}[1 - \sum_{k=1}^{n}\sum_{i=1}^{c}(u_{ik})^2/n] \quad (14)$$

where u_{ik} ($1 \le i \le c$, $1 \le k \le n$) is the membership value to the *i*th cluster center in the cluster centroid matrix for the *k*th observation in the data matrix, *c* is the cluster number and *n* is the number of observations.

The second performance index is the normalized classification entropy (NCE). The NCE models the disorganization of a fuzzy *c*-partition of the cluster centroid (Jiang et al. 2011b). The classification entropy (H) is defined as:

$$H(U;c) = -\sum_{k=1}^{n}\sum_{i-1}^{c} u_{ik}\log_a(u_{ik})\ /n \quad (15)$$

where logarithmic base *a* is any positive integer and *U* is a fuzzy membership matrix. Therefore, NCE can be defined as:

$$NCE = H(U;c)/\left[1 - \left(\frac{c}{n}\right)\right] \quad (16)$$

FPI and NCE values close to 0 mean that there is a large partition component and small sharing between *c*-partitions, indicating good classification results. The best number of zones will be determined by the class in which FPI and NCE values are at their minimum.

1.2.9. Vegetation Indices

Multispectral imagery is a tool that allows one to quickly obtain large amounts of data on varied crops. The amount of light being reflected by growing plants is associated with chlorophyll content and plant health. Green leaves with high chlorophyll content reflect more in the near infrared (NIR) and in the green wavelengths than in the red wavelength, while stressed leaves have low reflectance on wavelengths varying from 750 to 1100nm (Ortiz et al. 2011). Due to this difference in reflectance and absorption of light in the red and NIR bands, these two bands can be combined in many quantitative indices of vegetation conditions (Panda et al. 2010).

Vegetation indices have been correlated with crop properties such as LAI, green biomass (Inman et al. 2008), LWP (Elsayed et al. 2011), stomatal conductance, non-photochemical quenching (NPQ) (Rapaport et al. 2015), and plant water content (PWC) (Liu et al. 2004). For instance, the Normalized Difference Vegetation Index (NDVI) has been reported to be highly correlated with LWP, LAI and lint yield in cotton (Wanjura and Upchurch 2004). The correlation between NDVI and the three cotton properties ranged between $R^2 = 0.7$ and 0.75, which can be explained by the high association between LWP and individual red (750nm) and near infrared (880nm) wavelengths.

Despite its widespread use, NDVI presents many problems such as saturation in dense vegetation canopies (Sellers 1985), insensitivity to LAI with increasing LAI values, and the effect of soil brightness (Carlson and Ripley 1997). In cotton, when canopy closure occurs, NDVI values are greater than 0.8 and a plateau in the relation between NDVI and crop water use is reached. Nevertheless, NDVI has a positive linear relationship with crop water use when NDVI values are between 0.15 and 0.80, enabling effective use of NDVI in the delineation of management zones prior to canopy closure (Hunsaker et al. 2003).

The use of remote sensing in crop water assessment has greatly improved with the development of new vegetation indices. In recent work, three normalized water indices (WABIs) were created by combining the crop reflectance in three different bands (Rapaport et al. 2015). Hyperspectral signatures of water stressed grapevine leaves were correlated to midday LWP and it was found that the reflectance trend at different spectral regions can efficiently detect water stress as it was also indicated by Elsayed et al. (2011). Water stressed leaves presented decreased reflectance in the green (530-550 nm) and red edge (700-750 nm) regions and higher reflectance in the shortwave infra-red region (1500 nm; SWIR) (Figure 1.6). The normalized water balanced water indices (WABIs) presented better correlation with LWP than many well-known indices including NDVI. The ratio between SWIR and green bands, which yielded WABI-2 was the best in detecting LWP, presenting a R^2= 0.89 (Rapaport et al. 2015).

In 2002, a pioneer work funded by the NASA's solar-powered Pathfinder-Plus unmanned aerial vehicle (UAV) showed the usefulness of using UAVs to detect irrigation anomalies in agricultural fields (Herwitz et al. 2004). Since then, many authors have explored different types

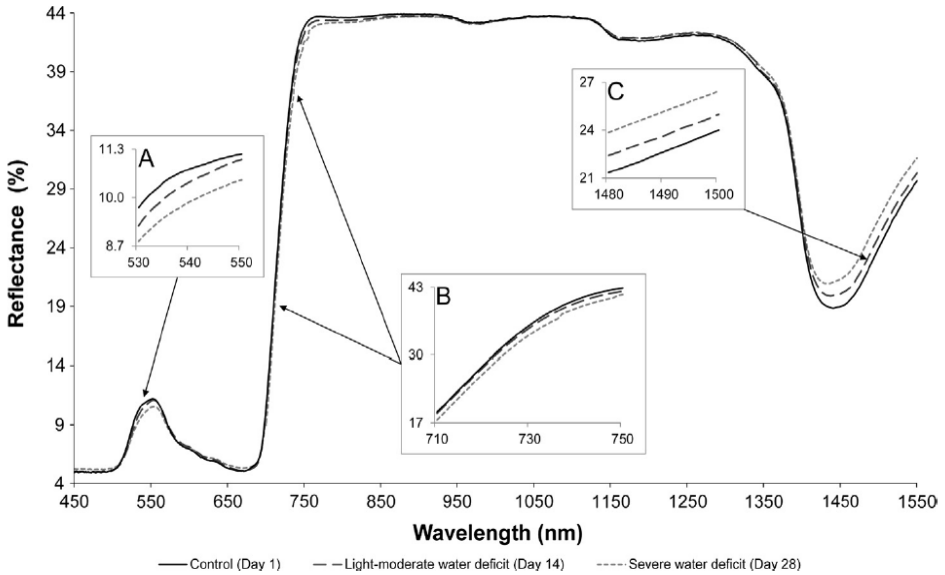

Figure 1.6. Changes in canopy reflectance in different spectral bands (Rapaport et al. 2015).

of commercial off-the-shelf unmanned aerial vehicles to assess water stress in varied crops with higher resolution than satellite platforms. Bajula et al. (2012) used an UAV equipped with a multispectral sensor Multiple Camera Array (MCA-6, Tetracam Inc., California, USA) to collect data from vineyards and calculate different indices related to water status. Zarco-Tejada et al. (2013) proposed a normalized Photochemical Reflectance Index (PRI) calculated from images taken with a SixCam multispectral camera (QuantaLab-IAS-CSIC, Cordoba, Spain) mounted on a fixed wing UAV. Many other pieces of equipment and platforms have been studied, and new technologies continue to emerge (Gago et al. 2015). Additional work exploring these technologies can lead to new vegetation indices that can better represent crop traits and platforms that are more user-friendly and simpler to use.

1.3. References

Ackerson, R.C., Hebert, R.R. (1981). Osmoregulation in cotton in response to water stress: I. Alterations in photosynthesis, leaf conductance, translocation, and ultrastructure. *Plant Physiology* 67, 484-488.

Alchanatis, V., Cohen, Y., Cohen, S., Moller, M., Sprinstin, M., Meron, M., et al. (2010). Evaluation of different approaches for estimating and mapping crop water status in cotton with thermal imaging. *Precision Agriculture* 11, 27-41.

Allen, R.G., Pereira, L.S., Raes, D., Smith, M. (1998). Crop evapotranspiration: Guidelines for computing crop water requirements. *Irrigation and Drainage*. Food and Agricultural Organization, United Nations, Rome, Italy.

Anderson, D.B. (1936). Relative humidity or vapor pressure deficit. *Ecology* 17, 277-282.

Bajula, J., Diago, M.P., Balda, P., Zorer, R., Meggio, F., Morales, F., et al. (2012). Assessment of vineyard water status variability by thermal and multispectral imagery using an unmanned aerial vehicle (UAV). *Irrigation Science* 30, 511-522.

Baker, J.T., Gitz, D.C., Stout, J.E., Lascano, R.J. (2015). Cotton water use efficiency under two different deficit irrigation scheduling methods. *Agronomy* 5, 363-373.

Bellvert, J., Marsal, J., Girona, J., Zarco-Tejada, P.J. (2015). Seasonal evolution of crop water stress index in grapevine varieties determined with high-resolution remote sensing thermal imagery. *Irrigation Science* 33, 81-93.

Bellvert, J., Zarco-Tejada, P.J., Girona, J., Fereres, E. (2014). Mapping crop water stress index in a ‘Pinot-noir’ vineyard: comparing ground measurements with thermal remote sensing imagery from an unmanned aerial vehicle. *Precision Agriculture* 15, 361-376.

Bellvert, J., Zarco-Tejada, P.J., Marsal, J., Girona, J., Conzalez-Dugo, V., Fereres, E. (2016). Vineyard irrigation scheduling based on airborne thermal imagery and water potential thresholds. *Australian Journal of Grape and Wine Research* 22, 307-315.

Blackmore, S., Godwin, R.J., Fountas, S. (2003). The analysis of spatial and temporal trends in yield map data over six years. *Biosystems Engineering* 84, 455-466.

Brock, A., Brouder, S.M., Blumhoff, G., Hofmann, B.S. (2005). Defining yield-based management zones for corn-soybean rotations. *Agronomy Journal* 97, 1115-1128.

Burke, J.J., Wanjura, D.F. (2010). Plant Responses to Temperature Extremes. In: Stewart J.M., Oosterhuis D.M., Heitholt J.J., Mauney J.R. (eds) Physiology of Cotton. Springer, Dordrecht.

Carlson, T.N., Ripley, D.A. (1997). On the relation between NDVI, fractional vegetation cover, and leaf area index. *Remote Sensing of the Environment* 62, 241-252.

Carmo-Silva, A.E., Gore, M.A., Andrade-Sanchez, P., French, A.N., Hunsaker, D.J., Salvucci, M.E. (2012). Decreased CO_2 availability and inactivation of Rubisco limit photosynthesis in cotton plants under heat and drought stress in the field. *Environmental and Experimental Botany* 83, 1-11.

Chastain, D.R., Snider, J.L., Collins, G.D., Perry, C.D., Whitaker, J., Byrd, S.A., et al. (2016b). Irrigation Scheduling using predawn leaf water potential improves water productivity in drip-irrigated cotton. *Crop Science* 56, 3185-3195.

Chiericati, M., Morari, F., Sartori, L., Ortiz, B., Perry, C., Vellidis, G. (2007). Delineating management zones to apply site-specific irrigation in the Venice lagoon watershed. In: Stafford, J.V. (Ed.), Precision Agriculture '07, Wageningen Academic Publishers, The Netherlands: Wageningen, pp. 599-606.

Cohen, Y., Alchanatis, V., Meron, M., Saranga, Y., Tsipris, J. (2005). Estimation of leaf water potential by thermal imagery and spatial analysis. *Journal of Experimental Botany* 56, 1843-1852.

Cohen, Y., Alchanatis, V., Saranga, Y., Rosenberg, O., Sela, E., Bosak, A. (2017). Mapping water status based on aerial thermal imagery: comparison of methodologies for upscaling from a single leaf to commercial fields. *Precision Agriculture* 18, 801-822.

Cohen, Y., Alchanatis, V., Sela, E., Saranga, Y., Cohen, S., Meron, M., et al. (2015). Crop water status estimation using thermography: Multi-year model development using ground-based thermal images. *Precision Agriculture* 16, 311-329.

Conaty, W.C., Burke, J.J., Mahan, J.R., Neilsen, J.E., Sutton, B.G. (2012). Determining the optimum plant temperature of cotton physiology and yield to improve plant-based irrigation scheduling. *Crop science* 52, 1828-1836.

Conaty, W.C., Mahan, J.R., Neilsen, J.E., Tan, D.K.Y., Yeates, S.J., Sutton, B.G. (2015). The relationship between cotton canopy temperature and yield, fibre quality and water-use efficiency. *Field Crop Research* 183, 329-341.

Cutler, M.J., Rains, D.W., Loomis, R.S. (1977). Role of changes in solute concentration in maintaining favorable water balance in field-grown cotton. *Agronomy Journal* 69, 773-779.

Ehrler, W.L. (1973). Cotton leaf temperatures as related to soil water depletion and meteorological factors. *Agronomy Journal* 65, 404-409.

Elsayed, S., Mistele, B., Schmidhalter, U. (2011). Can changes in leaf water potential be assessed spectrally? *Functional Plant Biology* 38, 523-533.

Ennahli, S., Earl, H.J. (2005). Physiological limitations to photosynthetic carbon assimilation in cotton under water stress. *Crop Science & Metabolism* 45, 2374-2382.

Erdem, T., Orta, A.H., Erdem, Y., Okursoy, H. (2005). Crop water stress index for potato under furrow and drip irrigation systems. *Potato Research* 48, 49-58.

Fernandez, J.E. (2017). Plant-based methods for irrigation scheduling of wood crops. *Horticulturae* 3, 35.

Fisher, D.K. (2012). Cotton water requirements in humid areas. USDA Agricultural Research Service, Stoneville, Mississippi.

Flexas, J., Medrano, H. (2002). Drought-inhibition of photosynthesis in C_3 plants: stomatal and non-stomatal limitations revisited. *Annals of Botany* 89, 183-189.

Fraisse, C.W., Sudduth, K.A., Kitchen, N.R. (2001). Delineation of site-specific management zones by unsupervised classification of topographic attributes and soil electrical conductivity. Transactions of ASAE 44, 155-166.

Fridgen, J.J., Kitchen, N.R., Sudduth, K.A, Drummond, S.T., Wiebold, W.J., Fraisse, C.W. (2004). Management zone analyst (MZA): software for subfield management zone delineation. *Agronomy Journal* 96,100–108.

Gago, J., Douthe, C., Coopman, R.E., Gallego, P.P., Ribas-Carbo, M., Flexas, J., et al. (2015). UAVs challenge to assess water stress for sustainable agriculture. *Agricultural Water Management* 153, 9-19.

Gerik, T.J., Faver, K.L., Thaxton, P.M., El-Zik, K.M. (1996). Late season water stress in cotton: I. Plant growth, water use, and yield. *Crop Science* 36, 914-921.

Grimes, D.W., Yamada, H. (1982). Relation of cotton growth and yield to minimum leaf water potential. *Crop Science* 22, 134-139.

Grimes, D.W., Yamada, H., Hughes, S.W. (1987). Climate-normalized cotton leaf water potentials for irrigation scheduling. *Agricultural Water Management* 12, 293-304.

Grimes, D.W., Miller, R.J., Dickens, L. (1970). Water stress during flowering of cotton. California Agriculture 24, 4-6.

Grimes, D.W., Dickens, W.L., Yamada, H. (1978). Early-season water management for cotton. *Agronomy Journal* 70, 1009-1012.

Gonzalez-Dugo, M.P., Moran, M.S. Mateos, L., Bryant, R. (2006). Canopy temperature variability as an indicator of crop water stress severity. *Irrigation Science* 24, 233-240.

Gonzalez-Dugo, V., Zarco-Tejada, P. Nicolas, E., Nortes, P.A., Alarcon, J.J., Intrigliolo, D.S., et al. 2013. Using high resolution UAV thermal imagery to assess the variability in the water status of five fruit tree species within a commercial orchard. Precision Agriculture 14, 660-678.

Guinn G., Mauney, J.R. (1984). Fruiting of cotton. I. Effects of moisture status on flowering. *Agronomy Journal* 76, 90-94.

Haghverdi, A., Leib, B.G., Washington-Allen, R.A., Ayers, P.D., Buschermohle, M.J. (2015). Perspectives on delineating management zones for variable rate irrigation. *Computers and Electronics in Agriculture* 117, 154-167.

Herwitz, S.R., Johnson, L.F., Dunagan, S.E., Higgins, R.G., Sullivan, D.V., Zheng, J., et al. (2004). Imaging from an unmanned aerial vehicle: agricultural surveillance and decision support. *Computers and Electronics in Agriculture* 44, 49-61.

Howell, T.A., Evett, S.R., Schneider, A.D. (2004). Evapotranspiration of full-, deficit-irrigated, and dryland cotton on the Northern Texas High Plans. *Journal of Irrigation and Drainage Engineering* 130, 277-285.

Hsiao, T.C. (1973). Plant responses to water stress. *Annual Review of Plant Physiology* 24, 519-570.

Hunsaker, D.J., Pinter Jr., P.J., Barnes, E.M., Kimball, B.A. (2003). Estimating cotton evapotranspiration crop coefficients with a multispectral vegetation index. *Irrigation Science* 22, 95-104.

Ibragimov, N., Evett, S.R., Esanbekov, Y., Kamilov, B.S., Mirzaev, L., Lamers, J.P.A. (2007). Water use efficiency of irrigated cotton in Uzbekistan under drip and furrow irrigation. *Agricultural Water Management* 90, 112-120.

Idso, S.B., Jackson, R.D., Pinter Jr., P.J., Reginato, R.J., Hatfield, J.L. (1981). Normalizing the stress-degree-day parameter for environmental variability. *Agricultural Meteorology* 24, 45-55.

Inman, D., Khosla, R., Reich, R., Westfall, D.G. (2008). Normalized Difference Vegetation Index and soil color-based management zones in irrigated maize. *Agronomy Journal* 100, 60-66.

Irmak, S., Haman, D.Z., Bastug, R. (2000). Determination of crop water stress index for irrigation timing and yield estimation of corn. *Agronomy Journal* 92, 1221-1227.

Intrigliolo, D.S., Castel, J.R. (2006). Performance of various water stress indicators for prediction of fruit size response to deficit irrigation in plum. *Agricultural Water Management* 83, 173-180.

Jackson, R.D., Idso, S.B., Reginato, R.J., Pinter, Jr., P.J. (1981). Canopy temperature as a crop water stress indicator. *Water Resources Research* 17, 1133-1138.

Jackson, R.D., Kustas, W.P., Choudhury, B.J. (1988). A reexamination of the crop water stress index. *Irrigation Science* 9, 309-317.

Jackson, S.H. (1991). Relationships between normalized leaf water potential and crop water stress index values for acala cotton. *Agricultural Water Management* 20, 109-118.

James, I.T., Waine, T.W., Bradley, R.I., Taylor, J.C., Godwin, R.J. (2003). Determination of soil type boundaries using electromagnetic induction scanning techniques. *Biosystems Engineering* 86, 421-430.

Jarvis, P.G. (1976). The interpretation of the variations in leaf water potential and stomatal conductance found in canopies in the field. *Philosophical Transactions of the Royal Society of London* 273, 593-610.

Jensen, M.E. (1968). Water consumption by agricultural plants (Chapter 1). In: Kozlowski, T.T. (ed.) Plant Water Consumption and Response. *Water Deficits and Plant Growth*, 2, 1-22.

Jiang, Q., Fu, Q., Wang, Z. (2011a). Delineating site-specific irrigation management zones. *Irrigation and Drainage* 60, 464-472.

Jiang, Q., Fu, Q., Wang, Z. (2011b). Study on delineation of Irrigation Management Zones based on management zones analyst software. In: Li D., Liu Y., Chen Y. (eds) Computer and Computing Technologies in Agriculture IV. CCTA 2010. IFIP Advances in Information and Communication Technology, vol 346. Springer, Berlin, Heidelberg.

Jones, H.G. (1990). Physiological aspects of the control of water status in horticultural crops. *Horticultural Science* 25, 19-26.

Jones, H.G. (1992). Plants and microclimate. Cambridge University Press (2nd edition) pp. 231-236.

Jones, H.G. (19990. Use of infrared thermometry for estimation of stomatal conductance as a possible aid to irrigation scheduling. *Agricultural and Forest Meteorology* 95, 139-149.

Jones, H.G. (2004). Irrigation scheduling: advantages and pitfalls of plant-based methods. *Journal of Experimental Botany* 55, 2427-2436.

Kaur, R., Singh, O.S. (1992). Response of growth stages of cotton varieties to moisture stress. *Indian Journal of Plant Physiology* 35, 182-185.

Krieg, D.R. (1997). Genetic and environmental factor affecting productivity of cotton. Proceeding Beltwide Cotton Conference, New Orleans, LA, January 7-10 Natl. Cotton Counc. Am., Memphis, TN, p.1347.

Liakos, V., Vellidis, G., Tucker, M., Lowrance, C., Liang, X. (2015). A decision support tool for managing precision irrigation with center pivots. In: J.V. Stafford (Ed.), Precision Agriculture '15 - Papers Presented the 10th European Conference on Precision Agriculture (10ECPA), Tel Aviv, Israel, p677-683.

Liang, X., Liakos, V., Wendroth, O., Vellidis, G. (2016). Scheduling irrigation using an approach based on the van Genuchten model. *Agricultural Water Management* 176, 170-179.

Liu, L., Wang, J., Huang, W., Zhao, C., Zhang, B., Tong, Q. (2004). Estimating winter wheat plant water content using red edge parameters. *International Journal of Remote Sensing* 25, 3331-3342.

Loka, D.A., Oosterhuis, D.M., Ritchie, G.L. (2011). Water-Deficit Stress in Cotton. In Stress Physiology in Cotton, Oosterhuis, D.M. (eds) 7, 37-72.

Lokhande, S., Reddy, K.R. (2014). Reproductive and fiber quality responses of Upland Cotton to Moisture Deficiency. *Agronomy Journal* 106, 1060-1069.

Longchamps, L., Khosla, R., Reich, R., Gui, D.W. (2015). Spatial and temporal variability of soil water content in leveled fields. *Soil & Water Management & Conservation* 79, 1446-1454.

Malik, R.S., Dhankar, J.S., Turner, N.C. (1979). Influence of soil water deficits on root growth of cotton seedlings. *Plant and Soil* 53, 109-115.

Mateos, L., Berengena, J., Orgaz, F., Diz, J., Fereres, E. (1991). A comparison between drip and furrow irrigation in cotton at two levels of water supply. *Agriculture Water Management* 19, 313-324.

Mauney, J.R. (1986). Vegetative growth and development of fruiting sites. In Cotton physiology. The Cotton Foundation, Memphis, TN.

McMichael, B.L., Hesketh, J.D. (1982). Field investigations of the response of cotton to water deficits. *Field Crops Research* 5, 319-333.

Meron, M., Tsipris, J., Orlov, V., Alchanatis, V., Cohen, Y. (2010). Crop water stress mapping for site-specific irrigation by thermal imagery and artificial reference surfaces. *Precision Agriculture* 11, 148-162.

Migliaccio, K.W., Morgan, K.T., Vellidis, G., Zotarelly, L., Fraisse, C., Zurweller, B.A., et al. (2015). Smartphone apps for irrigation scheduling. Transactions of ASABE 59, 291-301.

Monteith, J.L., M.L. Unsworth. (1990). Principles of environmental physics. London, UK: Edward Arnold.

Morari, F., Castrignano, A., Pagliarin, C. (2009). Application of multivariate geostatistics in delineating management zones within a gravelly vineyard using geo-electrical sensors. *Computers and Electronics in Agriculture* 68, 97-107.

Onder, D., Akiscan, Y., Onder, S., Mert, M. (2009). Effect of different irrigation water level on cotton yield and yield components. *African Journal of Biotechnology* 8, 1536-1544.

Ortiz, B., Shaw, J., Fulton, J. (2011). Basics of crop sensing. Alabama Cooperative Extension System, ANR-1398.

O'Shaughnessy, S.A., Evett, S.R. (2010). Canopy temperature based system effectively schedules and controls center pivot irrigation of cotton. *Agricultural Water Management* 97, 1310-1316.

O'Shaughnessy, S.A., Evett, S.R., Colaizzi, P.D. (2015). Dynamic prescription maps for site-specific variable rate irrigation of cotton. *Agriculture Water Management* 159, 123-138.

O'Shaughnessy, S.A., Evett, S.R., Colaizzi, P.D., Howell, T.A. (2011). Using radiation thermography and thermometry to evaluate crop water stress in soybean and cotton. *Agricultural Water Management* 98, 1523-1535.

Pace, P.F., Cralle, H.T., El-Halawany, S.H.M., Cothren, J.T., Senseman, S.A. (1999). Drought-induced changes in shoot and root growth of young cotton plants. *The Journal of Cotton Science*, 183-187.

Panda, S.S., Ames, D.P., Panigrahi, S. (2010). Application of vegetation indices for agricultural crop yield prediction using neural network techniques. *Remote Sensing* 2, 673-696.

Paço, T.A., Ferreira, M.I., Pacheco, C.A. (2013). Scheduling peach orchard irrigation in water stress conditions: use of relative transpiration and predawn leaf water potential. *Fruits* 68, 147-158.

Perry, C., Pocknee, S. (2003). Development of a variable-rate pivot irrigation control system. In: (Ed.) K.J. Hatcher, Proceedings of the 2003 Georgia Water Resources, Conference at the University of Georgia, April 23-24.

Pettigrew, W.T. (2004a). Physiological consequences of moisture deficit stress in cotton. *Crop Sciences* 44, 1265-1272.

Pettigrew, W.T. (2004b). Moisture deficit effects on cotton lint yield, yield components, and boll distribution. *Agronomy Journal* 96, 377-383.

Rapaport, T., Hochberg, U., Shoshany, M., Karnieli, A., Rachmilevitch, S. (2015). Combining leaf physiology, hyperspectral imaging and partial least squares-regression (PLS-R) for grapevine water status assessment. *ISPRS Journal of Photogrammetry and Remote Sensing* 109, 88-97.

Reginato, R.J. (1983). Field quantification of crop water stress. Transactions of the ASAE 26, 0772-0775.

Reynolds, W.D., Drury, C.F., Tan, C.S., Fox, C.A., Yang, X.M. (2009). Use of indicators and pore volume-function characteristics to quantify soil physical quality. *Geoderma* 152, 252-263.

Rosenberg, O., Alchanatis, V., Cohen, Y. (2014). Are thermal images adequate for irrigation management? In J.V. Stafford (Ed.), The 12th International conference on precision agriculture, Sacramento, CA.

Rud, R., Cohen, Y., Alchanatis, V., Levi, A., Brikman, R., Shenderey, C., et al. (2014). Crop water stress index derived from multi-year ground and aerial thermal images as an indicator of potato water status. *Precision Agriculture* 15, 273-289.

Scudiero, E., Teatini, P, Corwin, D.L., Deiana, R., Berti, A., Morari, F. (2013). Delineation of site-specific management units in a saline region at the Venice Lagoon margin, Italy, using soil reflectance and apparent electrical conductivity. *Computers and Electronics in Agriculture* 99, 54-64.

Sellers, P.J. (1985). Canopy reflectance, photosynthesis, and transpiration. *International Journal of Remote Sensing of Environment* 6, 1335-1372.

Shae, J.B., Steele, D.D., Gregor, B.L. 1999. Irrigation scheduling methods for potatoes in the Northern Great Plains. *Transactions of the ASAE*, 42, 351-360.

Singh, R.P., Vara Prasad, P.V., Sunita, K., Giri, S.N., Reddy, K.R. (2007). Influence of high temperature and breeding for heat tolerance in cotton: A review. *Advances in Agronomy* 93, 313-385.

Snider, J.L. and Chastain, D.R. (2016). Plant-Based Irrigation Scheduling. In: Snider, J.L. and Oosterhuis, D.M. (eds) Linking Physiology to Management. The Cotton Foundation, Cordova, TN, pp 97-116.

Snowden, M.C., Ritchie, G.L., Simao, F.R., Bordovsky, J.P. (2014). Timing of Episodic drought can be critical in cotton. *Agronomy Journal* 106, 452–458.

Tennakoon, S.B., Milroy, S.P. (2003). Crop water use and water use efficiency on irrigated cotton farms in Australia. *Agricultural Water Management* 61, 179-194.

Turner, N.C., Hearn, A.B., Begg, J.E., Constable, G.A. (1986). Cotton (*Gossypium hirsutum L.*): Physiological and morphological responses to water deficits and their relationship to yield. *Field Crops Research* 14, 153-170.

Ullah, A., Sun, H., Yang., X., Zhang, X. (2017). Drought coping strategies in cotton: increased crop per drop. *Plant Biotechnology Journal* 15, 271-284.

Van Genuchten, M.Th. (1980). A closed-form equation for predicting the hydraulic conductivity of unsaturated soils. *Soil Sciences* 44,892-898.

Vellidis, G., Liakos, V., Andreis, J.H., Perry, C.D., Porter, W.M., Barnes, E.M., et al. (2016a). Development and assessment of a smartphone application for irrigation scheduling in cotton. *Computers and Electronics in Agriculture* 127, 249-259.

Vellidis, G., Liakos, V., Perry, C.D., Porter, W.M., Tucker, M. (2016b). Irrigation scheduling for cotton using soil moisture sensors, smartphone apps, and traditional methods. In: Boyd, S., Huffman, M., and Robertson, B. (Eds), Proceedings of the 2016 Beltwide Cotton Conference, New Orleans, LA, National Cotton Council, Memphis, TN, p.772-780.

Vellidis, G., Liakos, V., Perry, C., Tucker, M., Collins, G., Snider, J., et al. (2014). A smartphone app for scheduling irrigation on cotton. In Proceedings of the 2014 Beltwide Cotton Conference, New Orleans, LA, Memphis, TN: National Cotton Council.

Vellidis, G., Liakos, V., Porter, W., Tucker, M., Liang, X. (2016c). A dynamic variable rate irrigation control system. 13th International Conference on Precision Agriculture. St. Louis, Missouri.

Vellidis, G., Liakos, V., Tucker, M., Perry, C., Andreis, J., Fraisse, C., et al. (2015). A smartphone app for precision irrigation scheduling in cotton. In Precision Agriculture 15. Wageningen Academic Publishers, 713-720.

Vellidis, G., Tucker, M., Perry, C. Kvien, C. Bednarz, C. (2008). A real-time wireless smart sensor array for scheduling irrigation. *Computers and Electronics in Agriculture* 61, 44-50.

Vellidis, G., Tucker, M., Perry, C., Reckford, D, Butts, C., Henry, H., et al. (2013). A soil moisture sensor-based variable rate irrigation scheduling system. In: J.V. Stafford (Ed.), Precision Agriculture 2013. Wageningen Academic Publishers, Wageningen.

Wang, R., Gao, M., Ji, S., Wang, S., Meng, Y., Zhou, Z. (2016a). Carbon allocation, osmotic adjustment, antioxidant capacity and growth in cotton under long-term soil drought during flowering and boll-forming period. *Plant Physiology and Biochemistry* 107, 137-146.

Wang, R., Ji, S., Zhang, P., Meng, Y., Wang, Y., Chen, B., Zhou, Z. (2016b). Drought effects on cotton yield and fiber quality on different fruiting branches. *Crop Science* 56, 1265-1276.

Wanjura, D.F., Upchurch, D.R., Maas, S. (2004). Spectral reflectance estimates of cotton biomass and yield. Proceedings of the Beltwide Cotton Conference, San Antonio, TX-January 5-9.

Wanjura, D.F., Upchurch, D.R., Mahan, J.R. (1992). Automated irrigation based on threshold canopy temperature. Transactions of the ASAE 35, 1411-1417.

Whitaker, J., Culpepper, S., Freeman, M., Harris, G., Kemerait, B., Perry, C., et al. (2018). Georgia Cotton Production Guide. Cooperative Extension, University of Georgia.

Yazar, A., Sezen, S.M., Sesveren, S. (2002). LEPA and trickle irrigation of cotton in the Southeast Anatolia Project (GAP) area in Turkey. *Agricultural Water Management* 54, 189-203.

Yule, I., Hedley, C.B., Bradbury, S. (2008). Variable-rate irrigation. Paper presented at the 12th Annual Symposium on Precision Agriculture Research and Application in Australia, Sydney, September 19, p. 7-9.

Zarco-Tejada, P.J., Gonzalez-Dugo, V., Willians, L.E., Suarez, L., Berni, J.A.J., Goldhamer, D., et al. (2013). A PRI-based water stress index combining structural and chlorophyll effects: Assessment using diurnal narrow-band airborne imagery and the CWSI thermal index. *Remote Sensing of Environment* 138, 38-50.

CHAPTER 2

USING UAV-BASED THERMAL AND MULTISPECTRAL IMAGERY TO DETECT CROP WATER STATUS VARIABILITY IN COTTON[1]

[1] Lacerda, L., Snider, J., Cohen, Y, Liakos, V., and Vellidis, G. To be submitted to the *Precision Agriculture* Journal

Abstract

Plant-based measurements such as leaf water potential (LWP) are used widely for irrigation scheduling because they are accurate at indicating when irrigation is needed. Despite being an efficient indicator, scheduling irrigation with LWP is time consuming and scale-limited. The work reported here explored the potential of using remote sensing to estimate cotton crop water status because this would allow the use of these techniques over large areas and on a more frequent basis. The study was conducted over two growing seasons (2018, 2020) in southwestern Georgia, USA using a complete randomized block design plot scheme with three irrigation treatments (rainfed, well-irrigated, and overirrigated). To monitor the irrigation treatment effects on cotton physiological response, predawn LWP (LWP_{PD}), stomatal conductance (g_s), mainstem height, leaf area index (LAI) and gas exchange measurements were taken in both growing seasons. UAV-based images collected in the green, red, red edge, near infrared, and thermal infrared wavebands were evaluated as predictors of plant water status indicators. Significant differences between the treatments were not observed in the 2018 growing season due to regular precipitation events. In 2020, the two irrigated treatments showed higher LWP_{PD}, LAI and g_s than the rainfed treatment. The study also compared the relationship between three crop water stress index (CWSI) calculation methodologies and LWP_{PD}. CWSI was calculated from thermal infrared images collected with a UAV. Despite the somewhat narrow range of LWP_{PD}, the different CWSIs showed a strong non-linear relationship indicating that UAV-based canopy reflectance has the potential to be used to create predictive LWP maps for the southeastern U.S. Despite the somewhat narrow range of LWP_{PD} caused by regular precipitation events during the growing seasons, the different CWSIs showed a strong non-linear relationship. UAV-based multispectral images also showed significant correlation with LWP_{PD} at specific dates. There

were differences in reflectance curves for different LWP_{PD} classes in the red edge and NIR wavebands. Overall, the results showed the potential of using affordable UAV- thermal and multispectral systems to monitor crop water status variability across the field and throughout a growing season.

2.1. Introduction

Cotton (*Gossypium hirsutum* L.) is an economically important crop in the United States (Chastain et al. 2014). In the commodity market, it is the number one trade product and the most important fiber crop. From a global perspective, cotton production is mostly concentrated in semi-arid and arid regions, often under irrigated conditions due to its negative response to excessive rainfall in certain morphological stages (Feike et al. 2017; Cetin and Basbag 2010), as well as its requirements for high solar radiation levels and high temperatures (Constable and Bange 2015). Even though its production is concentrated in arid areas, it can be cultivated under a variety of different water regimes (Hearn 1979; Turner et al. 1986).

In the southeastern United States, the average rainfall is approximately 1270 mm annually, which is enough water to supply crop needs for high yields (Bednarz et al. 2002). However, the distribution of rainfall during the growing season in this region may not align with the peak crop water requirements in some years. An eventual drought episode, even if short, at a critical stage of crop development can reduce the number of floral buds, boll retention (Turner et al. 1986), boll weight and distribution (Wang et al. 2016), and final yield (Hu et al. 2018). In addition, drought stress can cause reduction of photosynthetic rate caused by, among other factors, reduction in stomatal conductance (Loka et al. 2011). Overirrigation can also be a problem since it can result in low irrigation efficiency by creating drainage problems in the soil and resulting in depressed yields (Yazar et al. 2002). In addition, excessive irrigation can have a

severe impact on water resources, causing, in some cases, the depletion of surface and ground water (Soth et al. 1999; Vellidis et al. 2016b).

Because of the yield limitations imposed by water stress, a variety of irrigation scheduling techniques have been developed with the aim of improving the timing and amount of irrigation water applied with the end result of increasing irrigation water use efficiency (Vellidis et al. 2016a; Meeks et al. 2017; Li et al. 2019). Jones (2004) divided the most commonly used irrigation scheduling methods into three main classes; 1) irrigation based on soil water potential and soil water content, 2) soil water balance calculations, which involves estimating rainfall and evapotranspiration (ET), and 3) plant stress sensing, which is subdivided into tissue water status measurements and physiological responses. One direct plant stress indicator is leaf water potential (LWP).

Plant-based measurements such as LWP are an accurate indicator of the need for irrigation and can maximize water use efficiency in cotton (Grimes and Yamada 1982; Grimes et al. 1987; Chastain et al. 2016). Although there has been some controversy around the effectiveness of LWP as an irrigation indicator because of temporal fluctuations caused by environmental conditions (Jones, 2004), authors have found satisfactory results for different crops (Bellvert et al. 2016; Paço et al. 2013). In cotton, Argyrokastritis et al. (2015) measured midday LWP under two different irrigation methods (full and deficit irrigation) and found that LWP for stressed plants was significantly lower than the fully irrigated plants.

Despite being a good indicator for irrigation scheduling, LWP measured with a Scholander pressure chamber is time consuming and scale limited (Jackson, 1982; Elsayed et al. 2011) as each measurement in the field requires several minutes to perform with relatively cumbersome equipment. In this context, authors have explored the use of remote sensing to

detect or estimate crop water status as an alternative (Alchanatis et al. 2010; Rosenberg et al. 2014; Cohen et al. 2005). One approach is to calculate crop water stress index (CWSI) from canopy temperature extracted from thermal infrared images and to establish a relationship between CWSI and LWP (Cohen et al. 2015). LWP predicted from this relationship showed high agreement with measured LWP and was used to map LWP variability (Cohen et al. 2015).

Electromagnetic energy reflected from crop canopies in the visible and near infrared (NIR) wavebands have also shown great potential to detect water stress (Elsayed et al. 2011). Leaf structure and composition is the major determinant for leaf reflectance in the NIR region (Liu et al. 2004). Reflectance in this waveband tends to increase with increased water content. The effects of water content in the leaf intercellular air spaces, and cell shape and size can be detected not only in the NIR wavelength range (740-790 nm) but also in the red edge (680-740 nm) (Carter 1991). Vegetation indices (VIs) combining the percentage of light reflected in the NIR and visible wavebands such as the red band were also found to have high correlation with vegetation water content (Chen et al. 2005).

The overall goal of this study was to explore the potential of using UAV-based multispectral images and thermal images for measuring crop water stress in cotton in southern Georgia. Specific objectives were to use UAV-based multispectral images and thermal images to predict LWP_{PD} and stomatal conductance (g_s); and to compare the relationship between CWSI and LWP_{PD} with three different CWSI methodologies.

2.2. Materials and Methods

2.2.1. Study site and management practices

A two-year study was conducted in 2018 and 2020 in two different experimental fields at the University of Georgia's Stripling Irrigation Research Park (SIRP) in Camilla, GA (Figure

2.1). In 2018, 54 plots were established in a field of approximately 1 ha in size (31°16'43.33"N, 84°17'48.17"W). Each plot consisted of 16 rows each 12.2 m in length. The center 4 rows of each plot were used for data collection. Three different cultivars were planted at 2.5 cm depth on May 2nd. The three cultivars used were PHY 330 and PHY 440 (PhytoGen, Dow AgroSciences LLC, IN), and ST 6182 (GLT – Bayer Stoneville). Irrigation treatments were rainfed, 100% of estimated crop ET (ETc) and 125% ETc. A randomized complete block design was used with six replicates of each treatment (3 varieties × 3 irrigation treatments × 6 replicates).

In 2020, 27 plots were established in an experimental field approximately 3.6 ha in size. Plots had the same length and width as plots in 2018. Only the DP 1646 (Deltapine, Bayer) cultivar was used and was planted on May 13th. Irrigation treatments were the same as in 2018 (0% ETc, 100% ETc, and 125% ETc). A randomized complete block design was used with three replicates of each treatment (3 irrigation treatments × 3 replicates).

2.2.2. Irrigation treatments

The irrigation treatments were applied using a linear move system with overhead sprinkler irrigation equipped with variable rate irrigation (VRI) in 2018, and from three center pivot systems in 2020. ET_c was estimated using the SmartIrrigation Cotton App (Vellidis et al., 2016b). In the SmartIrrigation App, ET_c is estimated daily from reference ET (ET_0) using meteorological data from the Camilla University of Georgia Weather Station Network weather station at SIRP located within 300 m of both fields and a crop coefficient (K_c) extracted from a K_c curve that was validated for more than five years at SIRP (Vellidis et al., 2016b). Daily K_c was multiplied by daily ET_o to estimate daily ET_c. The 100% ET_c treatment (well-watered) was based on the deficit between daily ET_c and rainfall, which consisted of the well-watered treatment. The 125% ET_c treatment (over-irrigated) irrigation amount was estimated by

multiplying daily ET_c – precipitation by 1.25. The rainfed treatment received irrigation until the squaring stage to help with initial development and growth. No supplemental water was applied for the remaining of the season. Maximum irrigation rate per irrigation event was set at 19.05 mm in 2018 and 20.3 mm in 2020. The irrigation thresholds were estimated to avoid runoff and were also based on the irrigation system capacity.

2.2.3. Field data collection

To monitor the irrigation treatment effects cotton growth and physiological response, predawn LWP, mainstem height, LAI and gas exchange measurements were taken in both growing seasons. Measurements were collected weekly in 2018 and in two-week intervals in 2020 from squaring until the last week of irrigation. Predawn LWP (LWP_{PD}) was collected from 04:00 to 06:00 h for the uppermost fully expanded leaf of two plants in each plot using a Scholander pressure chamber (Model 615; PMS Instruments, Albany, OR). Cotton leaves were cut at the base of the petiole and sealed inside the chamber where pressure was applied until xylem sap exuded from the petiole cut surface. In-field leaf area index (LAI) was collected using an AccuPAR LP-80 (Decagon Devices Inc., Pullman, WA) ceptometer. This equipment consists of two light probes connected to a datalogger. A small quantum sensor is placed on a tripod to collect above canopy photosynthetically intercepted radiation (PAR) while a long quantum probe is placed under the canopy to collect below canopy PAR values simultaneously. Two above and below measurements were taken in each plot with one measurement being taken with the long probe positioned parallel to the cotton rows, and one perpendicular to the rows. The two measurements were averaged for analysis. In addition, gas exchange measurements were taken from the uppermost fully expanded leaf on two plants in each plot. Gas exchange measurements (stomata conductance (g_s)) were conducted from 12:00 to 14:00 h using an LI-6800 (LI-COR

Biosciences, Lincoln, NE) portable photosynthesis system. Leaf chamber settings included a flow rate of 600 µmol s^{-1}, reference CO_2 = 400 µmol mol^{-1}, air temperature = ambient temperature, relative humidity = 60 ± 15%, and chamber light intensity = 1500 µmol m^{-2} s^{-1} photosynthetically active radiation (PAR). The leaf was clamped into the chamber until steady-state conditions were reached (60 to 120 seconds per sample).

2.2.4. UAV sensors and data acquisition

Remotely sensed data were collected using two 3DR Solo quadcopters (3D Robotics, Berkeley, CA, United States), each equipped with a different sensor. To acquire thermal images, a FLIR Vue Pro R (Model 640, 69°FOV, 9mm, 30Hz; FLIR Systems, Inc., Wilsonville, OR) camera was adapted to the quadcopter using a fixed mount and a GPS geotagger (sUAS LLC, Beltsville, MD) to geotag images during flight. The FLIR Vue pro R uses an uncooled Vox microbolometer detector and collects 14-bit images (with embedded calibrated temperature values) in the 7.5 to 13.5 µm region of the electromagnetic spectrum. The second quadcopter was equipped with a Parrot Sequoia (MicaSense, Seattle, WA) multispectral camera. This sensor acquires images in four narrow bands that included green (530-570 nm), red (640-680 nm), red edge (730-740 nm) and NIR (770-810 nm). The Parrot Sequoia was adapted to the UAV using a fixed mount and a power and data board that provided power to the camera and geographic coordinates to geotag images during the flight.

UAV flights in 2018 were performed at 50 m altitude at a flight speed of 4 m/s and 80% front and side lap for multispectral flights and 90% for thermal. The spatial resolution of the multispectral images was 5.6 cm and 10.5 cm for thermal images. In 2020, side and front laps for both flights were the same as in 2018, but flights were performed at a higher altitude of 90 m and

higher speed of 9 m/s. The spatial resolution of multispectral images was 8.5 cm and 16.5 cm for thermal images.

2.2.5. Image processing

UAV flight images were stitched using Pix4Dmapper software (Pix4D SA, Lausanne, Switzerland). Processing templates were personalized to ensure the highest stitching quality. Ground control points (GCPs) were placed in the four corners of the field and used during stitching process to increase projection accuracy. The position of each GCP was taken with a GPS receiver in the field and then uploaded to Pix4Dmapper. GCPs were selected in at least 10 images for calibration. In addition, radiometric calibration was also performed in the multispectral images by using images of a calibration panel taken before and after each flight.

Final thermal and multispectral reflectance maps generated in Pix4Dmapper were then uploaded into ArcMap (ESRI, Redlands, CA, USA) for data processing and extraction. Shapefile with plot boundaries were created based on the images from the first flight, that also served as a base for georeferencing for subsequent images throughout the season. In addition, a buffer area of 0.5 m was created between plot boundaries. Both measures were taken to avoid extraction of pixels from rows outside the plot area.

The isocluster unsupervised classification method was used to identify soil and canopy pixels in multispectral images. Once separated, soil pixels were deleted before average pixel values per plot were extracted. In thermal images a methodology developed by Meron et al. (2010) was used for canopy temperature extraction. Briefly, soil and canopy pixels are separated by an upper (air temperature + 7°C) and lower (air temperature – 10°C) threshold. Subsequently, a second step is performed to eliminate mixed pixels commonly seen in the edges of the rows. In

this step, a class conditional temperature histogram of canopy related pixels is used, and the canopy temperature (T_c) is extracted by calculating the 33% coolest pixels.

2.2.6. Thermal camera accuracy

To test the accuracy of the FLIR Vue Pro R camera, a reference surface (RS) structure was constructed (Figure 2.2). The RS consisted of a 60 x 60 cm aluminum plate that was 2.2 cm thick. The size of the RS ensured that they would be represented by more than one pixel in both the multispectral and thermal images. One side was painted with matte paint and electronic components that enabled the plate's temperature to be measured in real time were attached to the other side. To measure the plate's temperature four thin film platinum resistance temperature detectors (RTDs) with three conductors were used. These sensors are classified as type A with an accuracy of +/- 0.15°C. To enable the real time temperature readings, an Arduino Mega embedded system (Arduino LLC, Torino, Italy) powered by rechargeable lithium batteries was used (Figure 2.2a). The Arduino was programmed to take readings every 5 seconds. An RTD sensor amplifier with MAX31865 breakout (Adafruit Industries, NY, USA) was used to connect the RTD sensors to the Arduino board and to ensure accuracy. The four sensors were attached to the bottom of the plate and covered by a 25 mm layer of expanded polystyrene insulation foam (Figure 2.2b). The plates were then attached to a PVC frame (Figure 2.2b, c)

In 2018, three surfaces painted black were placed in the field during the thermal flights to assess accuracy of temperature data extracted from the images. To obtain a wider range of known temperatures, two surfaces were modified and painted white and gray in 2020 (Figure 2.2c). Average temperatures measured by the four RTD sensors were calculated for comparison with the thermal camera. The ThermaCAM Researcher Pro 2.10 software (FLIR Systems, Inc., Wilsonville, OR) was used for individual image analysis. For each flight, at least one image in

which a RS appeared perpendicular to the camera was analyzed and the pixel temperature was extracted for comparison with averaged temperature measured from the four RTD sensors. To ensure temperature values from both platforms were from the same period, time stamps were checked. The sensor temperature was plotted versus the temperature measured from the FLIR camera and very good agreement between the two was observed (Figure 2.3). An error of approximately 2 °C was seen in 2018, and 2.77 °C in 2020. Error values were within the +/- 5 °C accuracy range claimed by the manufacturer.

2.2.7. Crop Water Stress Index

Canopy temperature data collected with the UAV-based thermal camera were used to calculate CWSI based on the following equation $CWSI= (T_c - T_{wet})/(T_{dry} - T_{wet})$, where CWSI varies from 0 to 1, representing a crop without any water limitation and a non-transpiring crop (Idso, 1981), T_{wet} represents the temperature of the lower baseline, and T_{dry} represents the temperature of the upper baseline. The wet and dry baselines were calculated using three different methodologies. The Jones 1 CWSI was calculated using theoretical dry and wet baselines based on the energy balance equation suggested by Jones (1999). The Jones 2 CWSI used the same theoretical wet baseline, but the dry baseline was calculated empirically by adding 5°C to the air temperature. The Monteith CWSI was calculated using a theoretical wet baseline based on Monteith and Unsworth (1990) and the empirical dry baseline used on Jones 2. Meteorological data used for baseline calculations was collected from the Camilla weather station located at SIRP. Data was recorded every 15 minutes from 12:00 to 14:00 h was averaged and used in calculations. The average of the 33% coolest pixels of each plot was used as T_c in the CWSI equation.

2.2.8. Statistical Analysis

The experiment was arranged as a randomized complete block design with three cultivars and three irrigation treatments. A two-way ANOVA using standard least squares was used for analysis of effects using JMP Pro 14.1.0 (SAS Institute, 2013). Treatment average values were analyzed using Tukey test. Data from all irrigation and cultivar treatments were used for 2018 and from all irrigation treatments for 2020 for the LAI, LWP_{PD}, and g_s analysis. A second-order polynomial regression was used to determine relationship between all three CWSIs calculated and LWP_{PD}. A sigmoid curve was used to demonstrate the reflectance curves of LWP_{PD} categories in the green, red, red edge, and NIR bands. The plot LWP_{PD} averages used for the reflectance analysis were chosen only from selected plots that showed different levels of water status. Plots with similar biomass were chosen to mitigate the difference in reflectance levels caused by difference in biomass. A linear regression was used to determine relationship between the two most sensitive bands.

2.3. Results and Discussion

2.3.1. Weather and Irrigation

Minimum and maximum air temperatures and rainfall during both growing seasons are represented in Figure 2.4. Precipitation was high in 2018 with average monthly rainfall above 100 mm in May and June and above 200 mm towards the middle of the season, while in 2020 precipitation was lower at the beginning of the season and higher in August and September. Total water (rainfall + irrigation) per treatment in 2018 was more than 1.5 times the amount in 2020 due to the high precipitation (Table 2.1). Cotton grown in Georgia requires approximately 460 mm of water well distributed among the growth stages (Bednarz et al. 2002; Ritchie et al.

2009). In 2018, precipitation was well above the cotton water requirement while in the second-year precipitation was approximately 113 mm lower than that required.

In 2018, precipitation was better distributed, and plants received enough water to supply its requirements in all growth stages. Approximate daily water requirement for cotton in humid regions from emergence to first square is around 2.54 mm (Bauer et al. 2012; Fisher 2004). This daily requirement ranges from 2.54 to 5.08 mm from first square to the first flower stage, and reaches its highest at early flowering until peak bloom with daily water use ranging from 5.08 to 7.11 mm. Cotton plants are sensitive to water stress during squaring (Bauer et al. 2012) and drought during this period can limit growth and number of nodes (Snowden et al. 2014), but highest sensitivity is seen during early bloom. Episodic drought in this period is critical and can lead to lower yield and lower fiber quality. After peak bloom daily water use decreases, but cotton plants still have a moderate sensitivity to water stress. Contrary to 2018, in 2020 smaller and inconsistent precipitation events caused episodic drought in the rainfed plots. Several consecutive days without rain caused the daily average precipitation to be 0.86 mm for the squaring period, which is well below the cotton water needs for the same period. Similarly, in a period of 17 days during early bloom, precipitation was only 7.87 mm.

2.3.2. Leaf area index (LAI)

Leaf area is an important cotton morphological trait because of its influence on final yield (Saleem et al. 2016) and its importance in determining crop ET (Al-Khafaf et al. 1978). Leaf area is very sensitive to drought because water stress leads to reduced cell division and expansion (Alves and Setter, 2004, Koch et al. 2019). In addition, drought conditions accelerate leaf senescence and abscission leading to lower LAI.

LAI treatment averages are presented in Figure 2.5. In both seasons LAI seasonal trends were similar with small values during the initial stages of development with values close to 1 at around 40 to 50 days after planting (DAP), and a rapid increase in leaf area between 50 and 80 DAP, and a subsequent decrease at the end of the season. During the first season, excessive rainfall resulted in similar LAI values between the different irrigation treatments (Figure 2.5a). Maximum treatment LAI values in the season were achieved at 99 DAP, with overirrigated plots showing an average LAI of 6.13, followed by 5.91 from well-watered plots and 5.7 in the rainfed plots. In contrast, a sharp difference in LAI trends between irrigation treatments can be seen in 2020. The rainfed treatment had the overall lowest averages with the highest LAI of 3.6 achieved at 95 DAP. Well-watered and overirrigated treatments had similar trends. Differences between these two treatments were evident only in the last two measurements at 95 to 111 DAP. Highest LAI for the irrigated treatments was also achieved at 95 DAP with values of 6.2 and 5.3 for the overirrigated and well-watered treatments, respectively. Similar irrigation regime effects in cotton LAI were observed by Noreen et al. (2013). Highest LAI was achieved during the flowering stage in which the biggest effects of drought on the rainfed treatment can also be observed.

Figure 2.6 shows the season-long LAI average values per treatment. In 2018, no significant differences were observed between treatments. Conversely, in 2020 rainfed and irrigated treatments were significantly different. The average LAI for well-watered and overirrigated treatments were not statistically different from each other, but overirrigated treatment had a value 0.58 higher than the well-watered. The rainfed treatment presented the lowest LAI of 2.54, which was 34% lower than the average between the other two treatments.

2.3.3. Leaf water potential (LWP_{PD}) and stomata conductance (g_s)

Seasonal weekly LWP_{PD} trends in 2018 were similar across all treatments (Figure 2.7a). Season-long averages ranged from -0.20 to -0.43 MPa, -0.24 to -0.41 MPa, and -0.22 to -0.38 MPa for rainfed, 100% ETc and 125% ETc treatments, respectively. In 2020, treatments had different seasonal LWP_{PD} trends (Figure 2.7b). The lowest average values for rainfed, well-watered, and overirrigated treatments were -0.60, -0.56, and -0.57 MPa, respectively. The well-watered and overirrigated treatments had the highest LWP_{PD} values (-0.34 and -0.38 MPa, respectively). Season-long irrigation treatment averages of LWP_{PD} were not significantly different in 2018 (Figure 2.8a). In contrast, season-long averages were significantly different ($p<0.05$) in 2020 (Figure 2.8b). The highest average LWP_{PD} value was observed in the well-watered treatment (-0.43 MPa) followed by the overirrigated treatment (-0.47). The rainfed plots had an average LWP_{PD} value 8% lower than the 100% ETc treatment. The decreased LWP_{PD} is a result of the anisohydric response of cotton plants (Tardieu and Simonneau 1998; Chastain et al. 2014) in which the water potential in the leaf decreases in response to a lower soil water potential.

As previously shown, canopy growth was substantially reduced in the rainfed plots displaying a lower LAI than irrigated treatments in 2020, which is evidence of obvious drought stress. Chastain et al. (2016) pointed out that plant growth inhibition was only observed when LWP_{PD} reached values below -0.8 MPa. Although measured LWP_{PD} values for the second season were higher than this previously noted threshold, a more severe drought occurred during the season in the weeks in between measurements. Although these periods of low precipitation did not coincide with LWP_{PD} field sampling days, the drought effects were prominent in the rainfed plots and can be detected by the leaf area differences between rainfed and irrigation treatments.

Stomatal conductance results for both seasons are shown in Figures 2.7c and d. In 2018, irrigation treatments seasonal averages were not statistically different from each other. The lowest average conductance values were 0.61, 0.69 and 0.57 mol m^{-2} $s^{-1}$for rainfed, 100% ETc, and 125% ETc respectively. The highest averages were observed for 125% ETc treatment (1.79 mol m^{-2} s^{-1}) followed by rainfed (1.78 mol m^{-2} s^{-1}) and 100% ETc (1.76 mol m^{-2} s^{-1}). Similar to results seen for LWP_{PD}, g_s average values were frequently lower in the rainfed plots in 2020 (Figure 2.7d). Well-watered and over-irrigated treatments had similar average g_s throughout the season with the exception of one week in late August.

Season-long g_s treatment averages were statistically similar in 2018 with all averages around 1.22 mol H_2O m^{-2} s^{-1} (Figure 2.8c). In 2020, average g_s values followed the trends observed for LWP_{PD} (Figure 2.8d). The highest leaf g_s was observed in the well-watered treatment with a value of 1.68 mol m^{-2} s^{-1}. The rainfed treatment showed the lowest season-long average with a value of 1.47 mol m^{-2} s^{-1}. The overirrigated treatment did not show any significant difference from the other two treatments.

The reduction in leaf stomatal conductance is a mechanism commonly seen in drought stressed plants to limit water loss (Li et al. 2020). A lower leaf water potential is observed when soil water availability is decreased, which triggers stomatal closure (Pilon et al. 2018). A substantial decrease in g_s was detected three days after plants were exposed to drought. In a recent study it was observed that g_s in rainfed plots was 72 and 58% lower than irrigated treatments in two consecutive years (Chastain et al. 2014). Pilon et al. (2018) observed even higher differences of 81% between well-watered and drought stressed cotton plants.

2.3.4. Relationship between crop water stress index (CWSI) and leaf water potential (LWP)

The CWSI values from the three different methods from all dates were shown in table 2.2. All methods yielded similar values within treatments in the individual dates. The season-long averages in both years were represented in Figure 2.9. There were no significant differences in the CWSI values between the irrigation treatments and within irrigation treatments in 2018. From the three methods used Jones 1 CWSI had the lowest values across all treatments, followed by Monteith and Jones 2. Overall CWSI values during the season were as high as 0.65 observed in the Jones 2 method and not lower than 0.48 in the Jones 1.

In 2020, CWSI average values were not different within each water treatment but were statistically different across treatments used ($p<0.05$). Specifically, all three methods resulted in higher CWSI values for the rainfed treatment. Season-long averages for the rainfed treatment were 0.53, 0.63, and 0.58 for Jones 1, Jones 2, and Monteith, respectively. Well-watered and overirrigated averages were similar with values of 0.4, 0.5 and 0.4 for Jones 1, Jones 2, and Monteith, respectively.

Weekly CWSI treatment averages plotted against LWP_{PD} for 2020 are shown in Figure 2.10. All CWSIs had a strong non-linear relationship with LWP_{PD} with all coefficients of determination equal to or higher than 0.61 ($p<.0001$). The strongest relationship was seen for the CWSI from Jones 1 and Jones 2 methods with values of 0.65 ($p<.0001$) and errors of 0.06 and 0.10, respectively. The theoretical dry and wet baselines used to calculate CWSI from Jones 1 resulted in overall lower values than when using the empirical baselines used for Jones 2 and Monteith. CWSI treatment averages plotted against LWP_{PD} did not have a significant relationship in 2018 and are not shown.

The relationship between CWSI and LWP_{PD} for the southern US was developed by Chastain et al. (2016) in a study conducted in the same region as the present study. A non-linear relationship between CWSI and LWP_{PD} was also observed with a coefficient of determination of 0.93. Results from their study showed a wider variation in $LWP_{PD.}$ However, canopy temperature for CWSI calculation was collected with proximal infrared sensors pointed directly at the canopy of individual plants. In the work reported here, the different CWSIs were calculated from UAV-based canopy temperature over plot-sized area and still showed strong correlation despite the lower variation in LWP_{PD}. Calculated CWSI values for plots with higher LWP_{PD} were overall higher than observed by Chastain et al. (2016), indicating an overestimation of the canopy temperature measured from the UAV camera.

The relationship between different CWSIs and LWP_{PD} is region specific. Results from present work using empirical, and theoretical baselines and from Chastain et al. (2016) that used empirical wet and dry baselines from Idso (1981) indicated a non-linear relationship between the two variables in the humid southeast of the U.S. Alchanatis et al (2010) developed the CWSI/LWP relationship for cotton in Israel where there is a Mediterranean climate using empirical and theoretical baselines and found a strong linear relationship. Similar linear relationship was also observed in the arid environment of northwestern Texas, U.S. using an empirical CWSI (O'Shaugnassey et al. 2011).

Cohen et al. (2017) highlighted the usefulness of using the CWSI/LWP relationship to create estimated LWP maps throughout the season. The ability to monitor plant water status from canopy temperature can help improve irrigation management decisions based on crop water needs even in the southeastern U.S. where humidity and frequent cloud cover makes this methodology challenging (Jones 2004).

2.3.5. Relationship between individual bands, leaf water potential (LWP_{PD}) and stomatal conductance (g_s)

Weekly treatment reflectance averages in the green, red, red edge and NIR bands for the entire season in 2018 and 2020 are represented in Figure 2.11. During 2018, treatment average canopy reflectance was very similar (Figure 2.11 a-d). There was a substantial decrease in reflectance in the green and red wavebands from June (36 DAP) to mid-September (71 DAP) after which reflectance remained constant between 0.08 to 0.09 for the green band, and 0.03 and 0.04 for the red band (Figure 2.11a, b). This is consistent with the increase in canopy cover and the overall increase in the presence of chlorophyll during this period. Chlorophyll is the pigment responsible for absorbing light in these wavebands as the light is the primary energy source for photosynthesis. Reflectance in the red edge band varied between 0.33 to 0.43 throughout the season (Figure 2.11c), while NIR reflectance showed an overall gradual increase despite the low value on the last sampling date in mid-September (Figure 2.11d). This is also consistent with increase in canopy cover as a well-watered, full-canopy crop will reflect the majority of the light in the NIR waveband.

During the 2020 growing season, there was a difference in canopy reflectance between treatments. This difference can be seen in the green, red, red edge and NIR bands, in which canopy in the rainfed plots had higher reflectance in the green and red wavebands (Figure 2.11e) and lower reflectance in the red edge (Figure 2.11g) and NIR wavebands (Figure 2.11h) than the irrigated treatments. The well-watered and overirrigated treatments had very similar reflectance across all wavebands.

The relationship between visible and NIR wavebands and plant water status indicators have been explored in a few studies (Ripple 1986; Bowman, 1989; Chen et al. 2012). Table 2.3

shows the weekly Pearson correlation between canopy reflection in the individual wavebands and LWP_{PD}. Significant correlations at multiple wavebands were observed only at 50 DAP in 2018, and at 59 and 74 DAP in 2020. Highest correlations were seen for the green waveband in 2018 (0.53, $p<.0001$) and for the red band in 2020 (-0.73, $p<.0001$). Reflectance in the red edge and NIR wavebands were highly correlated with values of 0.67 ($p<.001$) and 0.58 ($p<.001$) respectively.

The representative canopy spectral response curves from 2020 in the four wavebands are represented in Figure 2.12. The canopy reflectance curve was created only for dates on which more than one waveband had correlation higher than 0.5. The response curves represent the average reflectance value extracted from the two middle rows in the 9 plots with widest LWP_{PD} averages. The leaf reflectance curves were similar in the green and red wavebands and seemed to not be affected by different LWP_{PD}. Differences in canopy reflectance were noticed in the red edge and NIR bands with the highest differences at the longest wavelength. Results show an overall tendency of reflectance to decrease with lower LWP_{PD} values when curves are grouped into two main groups. Curves with LWP_{PD} higher than -0.51 MPa and lower than -0.55 were found to have the more distinguished differences. The lowest LWP_{PD} curve (-0.65 MPa) had the lowest reflectance in these two bands. The more prominent differences between reflectance responses in plants with varied water potentials in the red edge and NIR wavebands are related to the changes in leaf internal structures caused by loss of turgor pressure inside the cells (Bowman 1989).

Figure 2.13 shows the sensitivity of the different spectral bands to changes in LWP_{PD}. Reflectance in the green waveband remained constant while red waveband reflectance increased slightly with decreasing LWP_{PD} suggesting low sensitivity to changes in leaf water status. Both

the red edge and NIR wavebands exhibited decreasing reflectance with decreasing LWP_{PD}. Average reflectance in the red edge band varied from 0.27 to 0.33, while in the NIR waveband it varied from 0.35 to 0.45 as LWP_{PD} increased. The response of the green, red edge, and NIR wavebands is consistent to the changes in physiology that take place in the cotton canopy as water stress increases.

A linear regression was used to characterize the relationship between the red edge and NIR bands (Figure 2.14). A strong positive relationship between reflectance from these two wavebands was observed for treatments at all LWP_{PD} values. The regression coefficient was 0.83 ($p<.0001$).

The correlation between the reflectance in individual wavebands and stomatal conductance is shown in Table 2.4. In 2018, weekly canopy reflectance and g_s values showed significant correlations only at 71 and 113 DAP. In 2020, significant correlations were observed only at 59 DAP. All significant correlations were weak to moderate with green and red wavebands showing the highest correlations at all three dates. The weak correlations observed for the red edge and NIR bands can be a result of the low variability in g_s values throughout the season (see Figure 2.7c,d) . In addition, it has been pointed that stomatal conductance has a strong relationship with NIR and red edge wavebands when they are combined to calculate a VI (Carter 1998). Their study was pointed that individual wavebands such as NIR were not directly correlated with g_s, rather the wavebands correlated with photosynthetic rate that in turn is strongly correlated with g_s. In the current study, reflectance curves for different g_s value classes was not developed due to weak correlations. A wider range of g_s caused by a more severe drought can increase sensitivity of individual wavebands to different g_s values.

2.4. Conclusions

The current study explored cotton physiological and morphological responses to different irrigation treatments and their correlation with spectral reflectance to different regions of the spectrum over two growing seasons (2018, 2020). Significant differences between the treatments were not observed in the 2018 growing season due to regular precipitation events. In 2020, irrigated treatments (well-irrigated, and overirrigated) showed higher LWP_{PD}, LAI and g_s than rainfed treatment. Rainfed plots experienced drought for a maximum of 14 days during flowering, however field measurement dates did not coincide with peak stress periods. Despite the somewhat narrow range of LWP_{PD}, the different CWSIs showed a strong non-linear relationship indicating that UAV-based canopy reflectance has the potential to be used to create predicted LWP maps for the Southern US. Theoretical wet and dry baselines used to calculate Jones 1 CWSI had the strongest relationship (0.65, $p<.0001$) with LWP_{PD} and had the lowest error (0.06 MPa).

UAV-based multispectral images also showed significant correlation with LWP_{PD} at specific dates. There were differences in reflectance curves for different LWP_{PD} classes in the red edge and NIR wavebands. Both wavebands showed a strong linear relationship with red edge reflectance increasing with increased NIR reflectance. Results showed that these two wavebands can be used to develop new VIs in the visible and NIR ranges as an alternative to canopy temperature. Correlations between individual waveband reflectance showed lower correlations with g_s and are less promising for water status mapping.

Overall, the results showed a great potential of using affordable UAV- thermal and multispectral systems to monitor crop water status variability across the field and throughout a growing season. Further studies should test the UAV-based CWSI capacity to predict LWP_{PD}

with high accuracy across different locations and cultivars. In addition, calibration methods for thermal infrared cameras should be developed to reduce temperature errors and mitigate the temperature overestimation.

2.5. References

Alchanatis, V., Cohen, Y., Cohen, S., Moller, M., Sprinstin, Meron, M., Tsipris, J., Saranga, Y., Sela, E. (2010). Evaluation of different approaches for estimating and mapping crop water status in cotton with thermal imaging. *Precision Agriculture* 11, 27-41.

Alves, A.A.C, Setter, T.L. (2004). Response of cassava leaf area expansion to water deficit: cell proliferation, cell expansion and delayed development. *Annals of Botany*, 94, 605-613.

Al-Khafaf, S., Wierenga, P.J., Williams, B.C. (1978). Evaporative flux from irrigated cotton as related to leaf area index, soil water, and evaporative demand. *Agronomy Journal*, 70, 912-917.

Argyrokastritis, I.G., Papastylianou, P.T., Alexandris, S. (2015). Leaf water potential and crop water stress index variation for full and deficit irrigated cotton in Mediterranean conditions. *Agriculture and Agricultural Science Procedia*, 4, 463-470.

Bauer, P., Faircloth, W., Rowland, D., Richie, G. (2012). Water -sensitivity of cotton growth stages. In Perry. C., Barnes, E. (Eds) Cotton Irrigation Management for Humid Regions, Cotton Incorporated.

Bednarz, C., Ritchie, G, Hook, J, Yager, R, Cromer, S, Cook, D. et al. (2002). Cotton crop water use and irrigation scheduling. In: A.S. Culpepper, (Ed.) Georgia Cotton Research-Extension Report. Univ. of Georgia, Athens, GA, USA. pp. 61-64.

Bellvert J., Zarco-Tejada, P.J., Marsal, J., Girona, J, Gonzalez-Dugo, V., Fereres, E. (2016). Vineyard irrigation scheduling based on airborne thermal imagery and water potential thresholds. *Australian Journal of Grape and Wine Research*, 22, 307-315.

Bowman, W.D. (1989). The relationship between leaf water status, gas exchange, and spectral reflectance in cotton leaves. *Remote Sensing of Environment*, 30, 249-255.

Carter, K.H. (1996). Transpiration efficiency of tropical maize (*Zea mays* L.). PhD thesis. Swiss Federal Institute of Technology, Zurich, Switzerland.

Carter, G.A. (1998). Reflectance wavebands and indices for remote estimation of photosynthesis and stomatal conductance in Pine crops. *Remote Sensing of Environment*, 63, 61-72.

Cetin, O., S. Basbag. (2010). Effects of climatic factors on cotton production in semi-arid regions - A review. *Research on Crops* 11, 785-791.

Chastain D.R., Snider J.L., Collins G.D., Perry C.D., Whitaker J., Byrd S.A. (2014). Water deficit in field-grown *Gossypium hirsutum* primarily limits net photosynthesis by decreasing stomatal conductance, increasing photorespiration, and increasing the ratio of dark respiration to gross photosynthesis. *Journal of Plant Physiology*, 171, 1576-1585.

Chastain D.R., Snider, J.L., Collins, G.D., Perry, C.D., Whitaker, J., Byrd, S.A., Oosterhuis, D.M., Porter, W.M. (2016). Irrigation Scheduling using predawn leaf water potential improves water productivity in drip-irrigated cotton. *Crop Science,* 56, 3185-3195.

Chen, D., Huang, J., Jackson, T.J. (2005). Vegetation water content estimation for corn and soybeans using spectral indices derived from MODIS near- and short-wave infrared bands. *Remote Sensing of Environment* 98, 225-236.

Chen, H., Wang, P., Li, J., Zhang, J., Zhong, L. (2012). Canopy spectral reflectance feature and leaf water potential of sugarcane inversion. *Physics Procedia*, 25, 595-600.

Cohen Y., Alchanatis, V., Meron, M., Saranga, Y., Tsipris, J. (2005). Estimation of leaf water potential by thermal imagery and spatial analysis. *Journal of Experimental Botany* 56, 1843-1852.

Cohen, Y., Alchanatis, V., Saranga, Y., Rosenberg, O., Sela, E., Bosak, A. (2016). Mapping water status based on aerial thermal imagery: comparison of methodologies for upscaling from a single leaf to commercial fields. *Precision Agriculture*, 18, 801-822.

Cohen Y., Alchanatis, V., Sela, E., Saranga, Y., Cohen, S., Meron, M., Bosak, A., Tsipris, V., Orolov, V. (2015). Crop water status estimation using thermography: multi-year model development using ground-based thermal images. *Precision Agriculture* 16, 311-329.

Constable, G.A., M.P. Bange. (2015). The yield potential of cotton (Gossypium hirsutum L.). *Field Crops Research*, 182, 98-106.

Elsayed, S., Mistele, B., Schmidhalter, U. (2011). Can changes in leaf water potential be assessed spectrally? *Functional Plant Biology*, 38, 523-533.

Feike, T., Khor, L.Y., Mamitimin, Y., Ha, N., Li, L., Abdusalih, N., et al. (2017). Determinants of cotton farmers' irrigation water management in arid Northwestern China. *Agricultural Water Management,* 187, 1-10.

Fisher, D.K. (2004). Simple and inexpensive lysimeters for monitoring reference- and crop-ET. Proceedings of the 25th Annual International Irrigation Conference, November 14-16, Tampa, Florida.

Grimes D.W., Yamada, H. (1982). Relation of cotton growth and yield to minimum leaf water potential. *Crop Science,* 22, 134-139.

Grimes D.W., H. Yamada, S.W. Hughes. (1987). Climate-normalized cotton leaf water potentials for irrigation scheduling. *Agricultural Water Management,* 12, 293-304.

Hearn A.B. (1979). Water relationships in cotton. Outlook on Agriculture, 10, 159-166.

Hu, W., Snider, J.L., Wang, H., Zhou, Z., Chastain, D.R., Whitaker, J., et al. (2018). Water-induced variation in yield and quality can be explained by altered yield component contributions in field-grown cotton. *Field Crops Research*, 224, 138.147.

Idso, S.B., Jackson, R.D., Pinter Jr., P.J., Reginato, R.J., Hatfield, J.L. (1981). Normalizing the stress-degree-day parameter for environmental variability. *Agricultural Meteorology*, 24, 45-55.

Jackson, R.D. (1982). Canopy temperature and crop water stress. In 'Advances in irrigation'. (Eds GS Campbell, MD Jackson) pp. 43-85. Academic Press: New York.

Jones H.G. (1999). Use of infrared thermometry for estimation of stomatal conductance as a possible aid to irrigation scheduling. *Agricultural and Forest Meteorology* 95, 139-149.

Jones, H.G. (2004). Irrigation scheduling: advantages and pitfalls of plant-based methods. *Journal of Experimental Botany*, 55, 2427-2436.

Koch, G., Rolland, G., Dauzat, M., Bédiée, A., Baldazzi, V., Bertin, N., et al. (2019). Leaf production and expansion: A generalized response to drought stresses from cells to whole leaf biomass- A case study in the tomato compound leaf. *Plants*, 8, 409.

Li, F., Dong, Y., Zhao, Y. (2019). Irrigation scheduling optimization for cotton based on the AquaCrop model. *Water Resources Management*, 33, 39-55.

Li, X., Smith, R., Choat, B., Tissue, D.T. (2020). Drought resistance of cotton (*Gossypium hirsutum)*is promoted by early stomatal closure and leaf shedding. *Functional Plant Biology*, 47, 91-98.

Liu, L., Wang, J., Huang, W., Zhao, C., Zhang, B., Tong, Q. (2004). Estimating winter wheat plant water content using red edge parameters. *Remote Sensing* 25, 3331-3342.

Loka, D.A., Oosterhuis, D.M., Ritchie, G.L. (2011). Water-Deficit Stress in Cotton. pp. 37-72. In: Oosterhuis, D.M. (ed.). Stress Physiology in Cotton. The Cotton Foundation, Memphis, Tenn.

Meeks, C.D., Snider, J.L., Porter, W.M., Vellidis, G., Hawkins, G., Rowland, D. (2017). Assessing the utility of primed acclimation for improving water savings in cotton using a sensor-based irrigation scheduling system. *Crop Science*, 57, 2117-2129.

Meron, M., Tsipris, J., Orlov, V., Alchanatis, V., Cohen, Y. (2010). Crop water stress mapping for site-specific irrigation by thermal imagery and artificial reference surfaces. *Precision Agriculture* 11, 148-162.

Monteith J.L., M.L. Unsworth. (1990). Principles of environmental physics. London, UK: Edward Arnold.

Noreen, S., Athar, H.U.R., Ashraf, M. (2013). Interactive effects of watering regimes and exogenously applied osmoprotectants on earliness indices and leaf area index in cotton (*Gossypium hirsutum* L.) crop. *Pakistan Journal of Botany*, 45, 1873-1881.

O'Shaughnessy, S.A., Evett, S.R., Colaizzi, P.D., Howell, T.A. (2011). Using radiation thermography and thermometry to evaluate crop water stress in soybean and cotton. *Agricultural Water Management*, 98, 1523-1535.

Paço T.A., Ferreira, M.I., Pacheco, C.A. (2013). Scheduling peach orchard irrigation in water stress conditions: use of relative transpiration and predawn leaf water potential. Fruits, 68, 147-158.

Pilon, C., Loka, D., Snider, J.L., Oosterhuis, D.M. (2018). Drought-induced osmotic adjustment and changes in carbohydrate distribution in leaves and flowers of cotton (*Gossypium hirsutum* L.). *Journal of Agronomy and Crop Science*, 205, 168-178.

Ripple, W.J. (1986). Spectral reflectance relationships to leaf water stress. *Photogrammetric Engineering & Remote Sensing*, 52, 1669-1675.

Ritchie, G.L., Whitaker, J.R., Bednarz, C.W., Hook, J.E. (2009). Subsurface drip and overhead irrigation: a comparison of plant boll distribution in upland cotton. *Agronomy Journal*, 101, 1336-1344.

Rosenberg, O., Alchanatis, V., Cohen, Y. (2014). Are thermal images adequate for irrigation management? In Stafford J.V. (Ed.), The 12th International conference on precision agriculture, Sacramento, CA.

Saleem, M.F., Raza, M.A.S., Ahmad, S., Khan, I.H., Shahid, A.M. (2016). Understanding and mitigating the impacts of drought stress in cotton- a review. *Pakistan Journal of Botany*, 53, 609-623.

Snowden, M.C., Ritchie, G.L., Simao, F.R., Bordovsky, J.P. (2014). Timing of episodic drought can be critical in cotton. *Crop Ecology & Physiology* 106, 452-458.

Soth J., C. Grasser, R. Salerno. (1999). The impact of cotton on freshwater resources and ecosystems. A preliminary synthesis. Worldwide Fund for Nature (WWF), Gland, Switzerland.

Tardieu, F., Simonneau, T. (1998). Variability among species of stomatal control under fluctuating soil water status and evaporative demand: modeling isohydric and anisohydric behaviors. *Journal of Experimental Botany*, 49, 419-432.

Turner N.C., Hearn, A.B., Begg, J.E., and Constable, G.A. (1986). Cotton (*Gossypium Hirsutum L.*): Physiological and morphological responses to water deficits and their relationship to yield. *Field Crops Research* 14, 153-170.

Vellidis, G., Liakos, V., Andreis, J.H., Perry, C.D., Porter, W.M., Barnes, E.M., et al. (2016b). Development and assessment of a smartphone application for irrigation scheduling in cotton. *Computers and Electronics in Agriculture*, 127, 249-259.

Vellidis, G., Liakos, V., Perry, C., Tucker, M., Collins, G., Snider, J., et al. (2014). A smartphone app for scheduling irrigation on cotton. In S. Boyd, M. Huffman and B. Robertson (Eds) Proceedings of the 2014 Beltwide Cotton Conference, New Orleans, LA, National Cotton Council, Memphis, TN, p.175-186.

Vellidis, G., Liakos, V., Porter, W., Tucker, M., Liang, X. (2016a). A dynamic variable rate irrigation control system. 13th International Conference on Precision Agriculture. St. Louis, Missouri.

Wang, R., Zhang, P., Meng, Y., Wang, Y., Chen, B., Zhou, Z. (2016). Drought effect on cotton yield and fiber quality on different fruiting branches. *Crop Science, 56, 1265-1276.*

Yazar, A., S.M. Sezen, S. Serveren. (2002). LEPA and trickle irrigation of cotton in the Southeast Anatolia Project (GAP) area in Turkey. *Agricultural Water Management*, 54, 189-203.

TABLES AND FIGURES

Table 2.1. Irrigation, rainfall, and total water applied in both fields in Camilla, GA during the 2018 and 2020 growing seasons.

Year	Treatment	Irrigation	Precipitation	Total Water
		---------- mm ----------		
2018	Rainfed	0	828	828
	100% ETc	220	828	1048
	125% ETc	251	828	1079
2020	Rainfed	36	347	383
	100% ETc	252	347	599
	125% ETc	309	347	656

Table 2.2. Average treatment CWSI values calculated from the three different methods for all dates.

Year	Date	Treatments	CWSI (Jones 1)	CWSI (Jones 2)	CWSI (Monteith)
2018	07/12/18	Rainfed	0.573	0.749	0.713
		100% ETc	0.534	0.702	0.659
		125% ETc	0.550	0.721	0.680
	07/27/18	Rainfed	0.515	0.617	0.523
		100% ETc	0.498	0.597	0.499
		125% ETc	0.492	0.592	0.491
	08/09/18	Rainfed	0.331	0.429	0.325
		100% ETc	0.318	0.412	0.305
		125% ETc	0.326	0.422	0.317
	08/23/18	Rainfed	0.626	0.797	0.760
		100% ETc	0.586	0.748	0.702
		125% ETc	0.604	0.770	0.727
2020	07/26/20	Rainfed	0.614	0.778	0.741
		100% ETc	0.406	0.525	0.448
		125% ETc	0.410	0.529	0.453
	08/16/20	Rainfed	0.148	0.453	0.333
		100% ETc	0.385	0.418	0.291
		125% ETc	0.300	0.328	0.181
	09/01/20	Rainfed	0.543	0.713	0.656
		100% ETc	0.422	0.561	0.475
		125% ETc	0.492	0.648	0.578

Table. 2.3. Pearson correlation between weekly average reflectance at individual wavebands and average LWP_{PD} during both growing seasons from 44 DAP onwards.

Bands	DAP									
	2018						2020			
	44	50	65	71	86	113	59	74	95	111
Green	-0.10	0.53**	0.03	0.13	-0.02	-0.11	-0.40*	-0.12	0.16	-0.39
Red	-0.10	0.49*	0.05	0.29*	0.03	-0.09	-0.42*	-0.73**	0.02	-0.49
REg	-0.15	0.38*	0.12	-0.03	-0.21	-0.23	0.38*	0.67*	0.34	-0.07
NIR	0.007	-0.05	-0.05	0.18	0.02	0.12	0.40*	0.58*	0.23	0.27

Table. 2.4. Pearson correlation between weekly average reflectance at individual bands and average g_s during both growing seasons from 44 DAP onwards.

Bands	DAP									
	2018						2020			
	44	50	65	71	86	113	59	74	95	111
Green	0.0005	0.29	-0.26	-0.42*	0.25	-0.35*	-0.50*	-0.04	0.32	0.27
Red	0.04	0.27	-0.18	-0.35*	0.19	-0.36*	-0.48*	-0.29	-0.26	0.02
REg	0.08	0.12	0.07	-0.28*	-0.04	-0.34	0.27	0.35	0.38	0.25
NIR	0.04	0.02	0.004	-0.32*	-0.20	0.25	0.35	0.34	0.27	-0.10

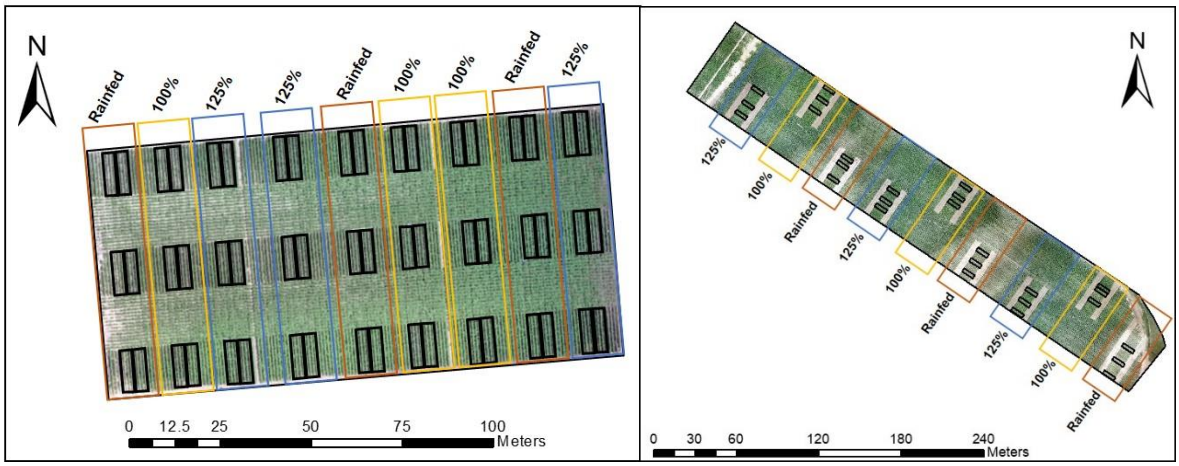

Figure 2.1. . Layout of fields in 2018 and 2020. Irrigation treatments are shown in different colors. Well-watered treatment is represented as 100% ETc, and overirrigated is represented as 125% Etc.

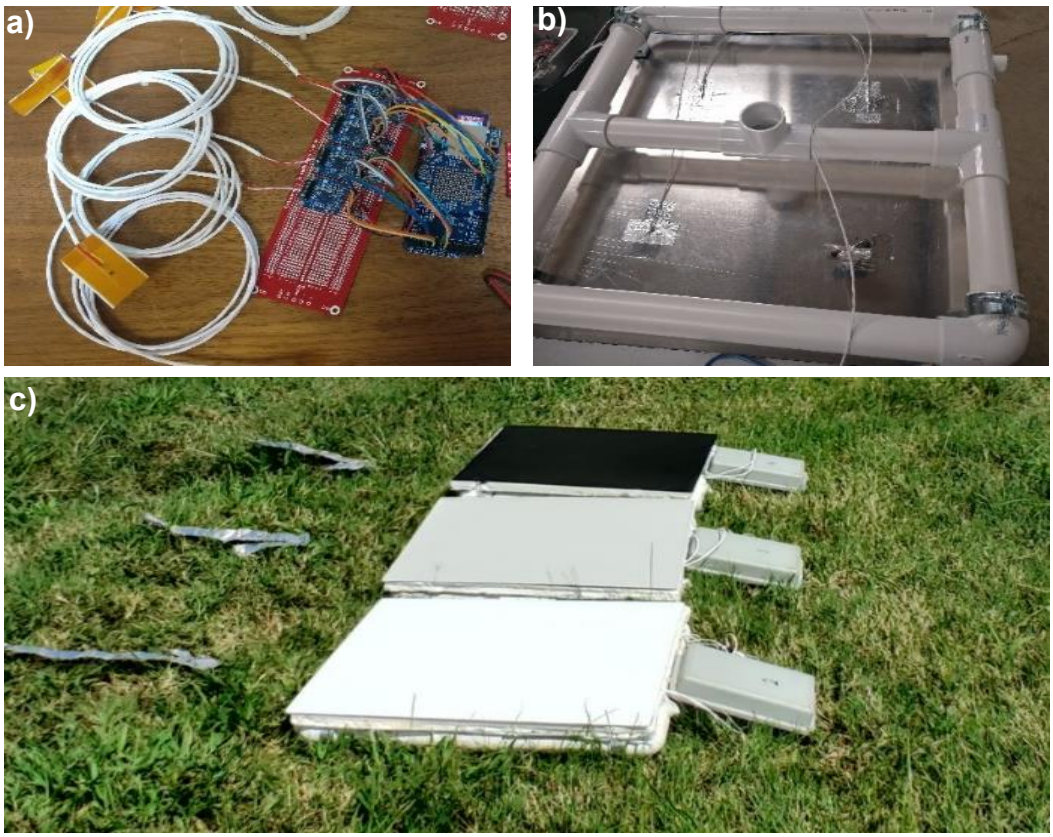

Figure 2.2. Electronics for temperature sensing in real time (a), placement of RTDs in the aluminum plate (b) and white, gray, and black RS in the field (c).

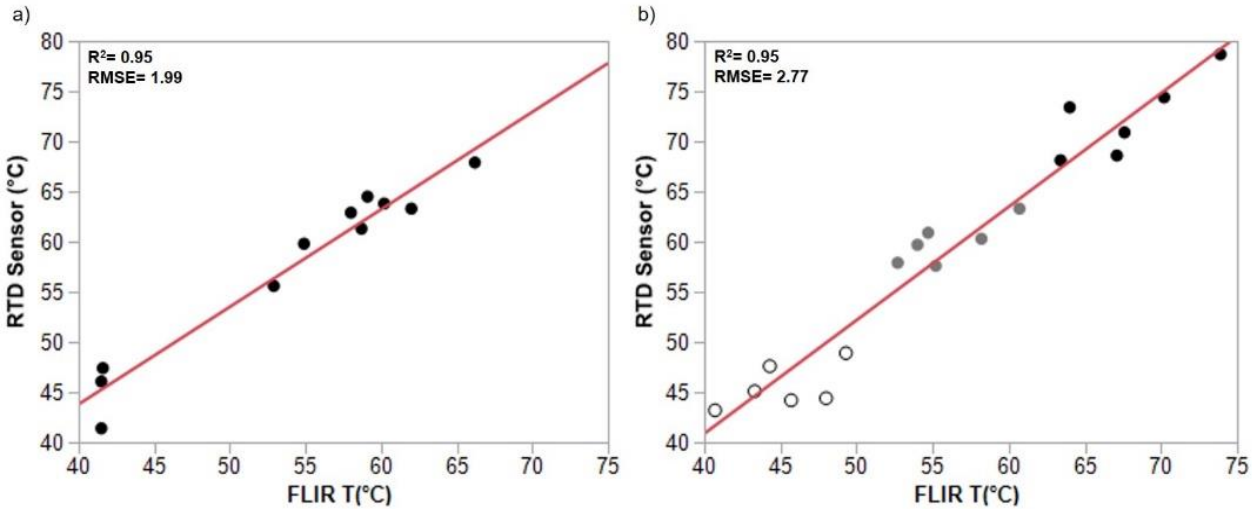

Figure 2.3. Relationship between FLIR-based temperature and RTD sensor temperature in (a) 2018, and (b) 2020. White, grey, and black points in 2020 refer to the different colored surfaces.

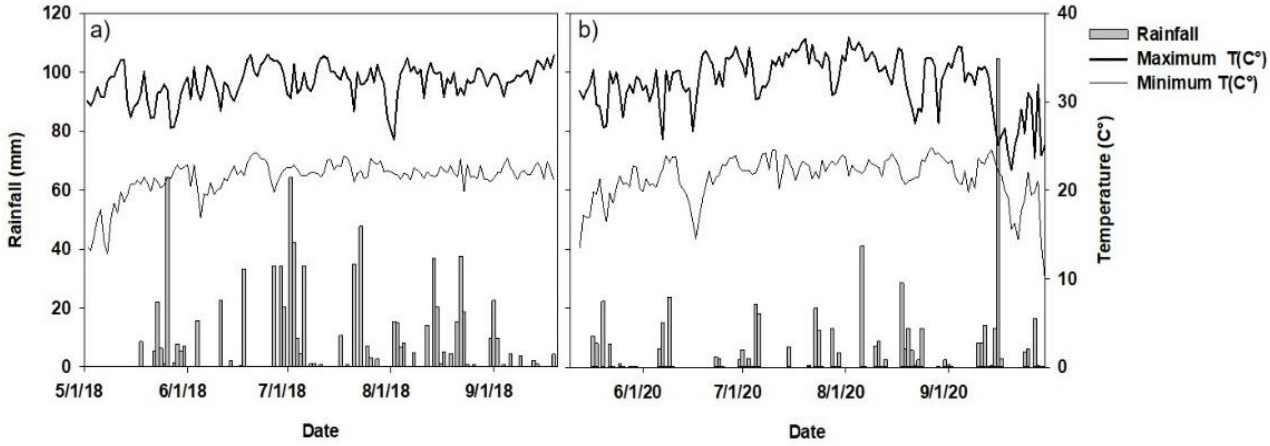

Figure 2.4. Daily precipitation and maximum and minimum air temperature during the cotton-growing season in 2018 (a) and 2020 (b).

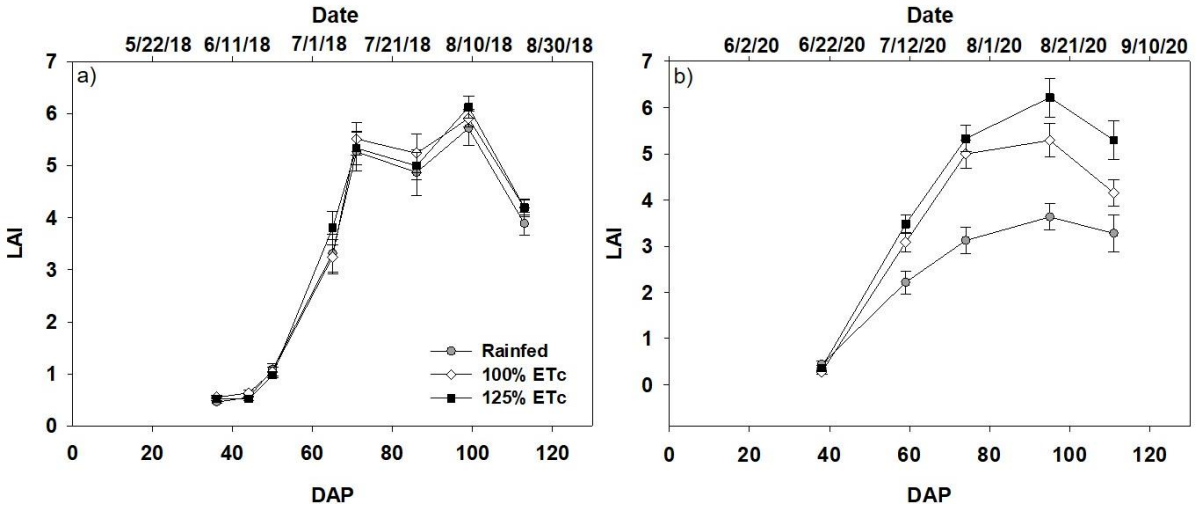

Figure 2.5. Leaf area index (LAI) seasonal trends in Camila, GA in 2018 (a) and 2020 (b). Data represent means ± SE (2018; n = 18, 2020; n = 9).

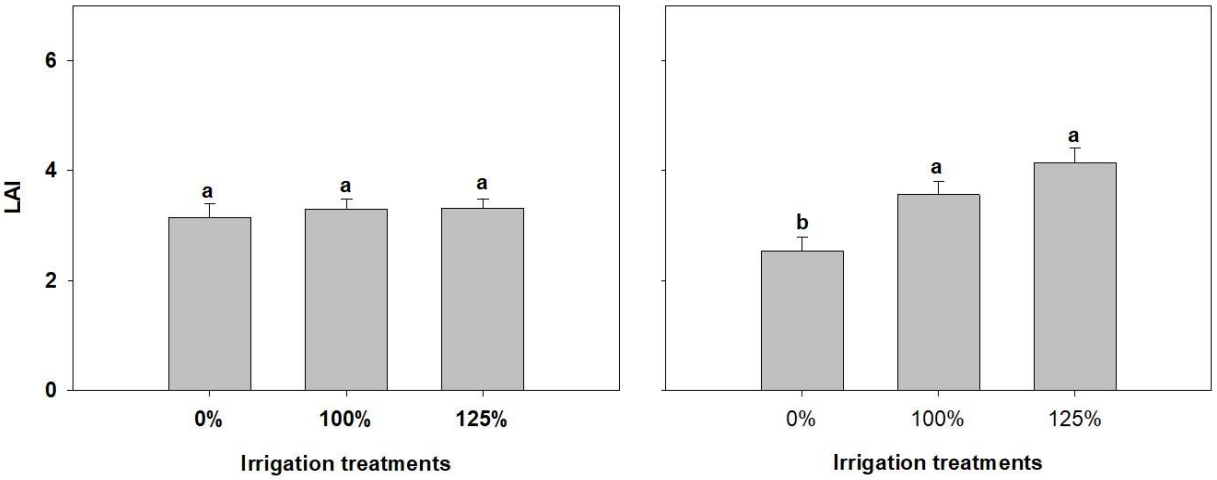

Figure 2.6. Season-long irrigation treatment leaf area index (LAI) averages for cotton grown in Camilla, GA in 2018 (a) and 2020 (b). Bars with the same letters are not significantly different ($p<0.05$). Data represent means ± SE (2018; n = 8, 2020; n = 5).

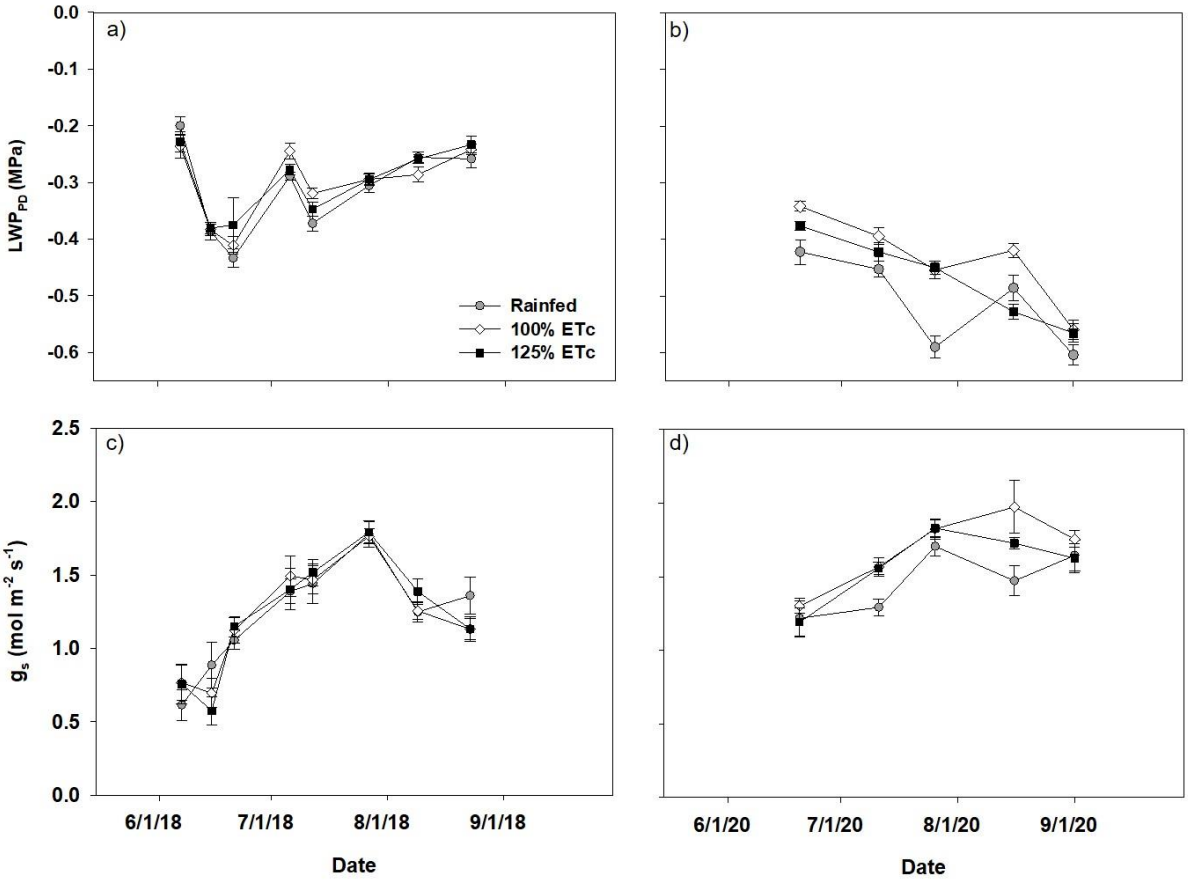

Figure 2.7. Predawn leaf water potential (LWP_{PD}) (a,b) and stomata conductance (g_s) (c-d) seasonal trends in Camila, GA. The 2018 growing season is represented on the left panel and the 2020 in the right panel. Data represent means ± SE (2018; n = 18, 2020; n = 9).

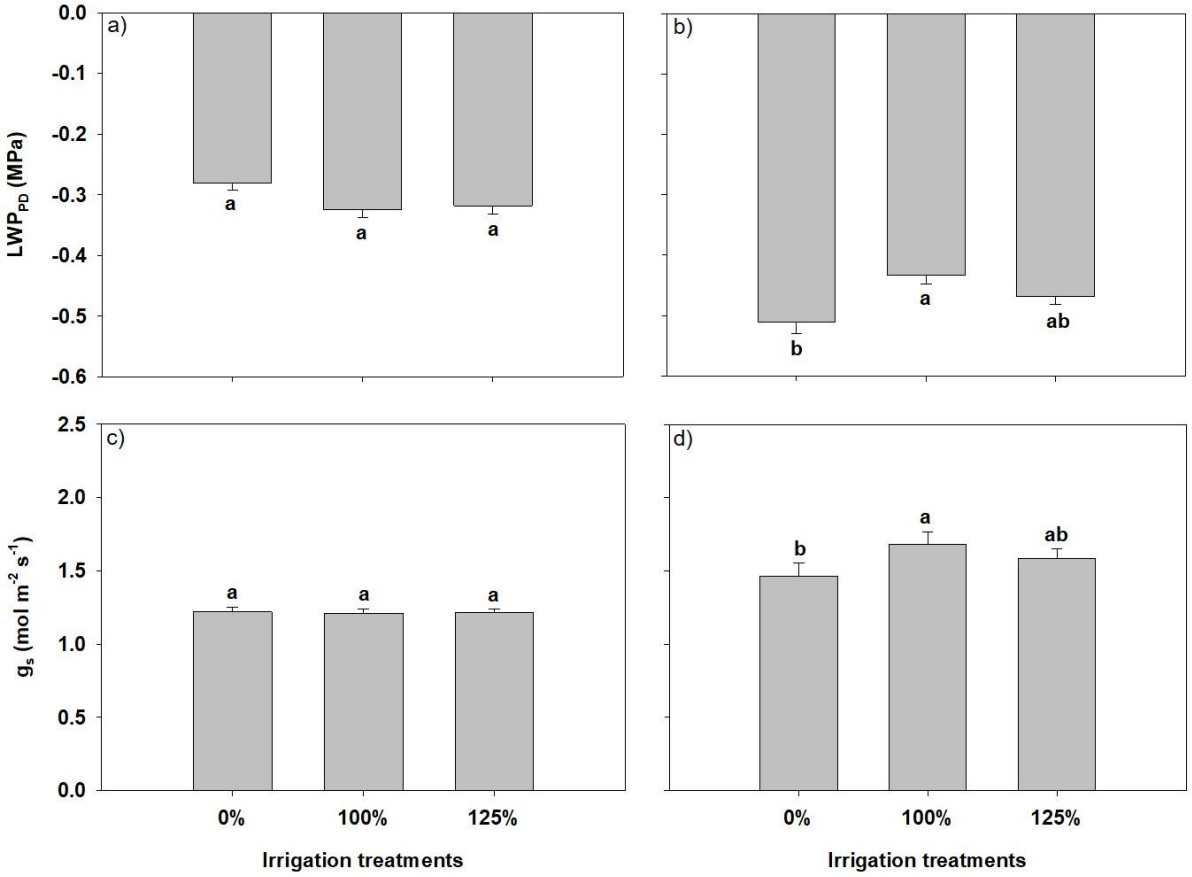

Figure 2.8. Season-long irrigation treatment predawn leaf water potential (LWP_{PD}) (a) and stomata conductance (g_s) (b) averages for cotton grown in Camilla, GA. Left panel shows data from 2018, and right panel from 2020. Bars with the same letters are not significantly different ($p<0.05$). Data represent means ± SE (2018; n = 8, 2020; n = 5).

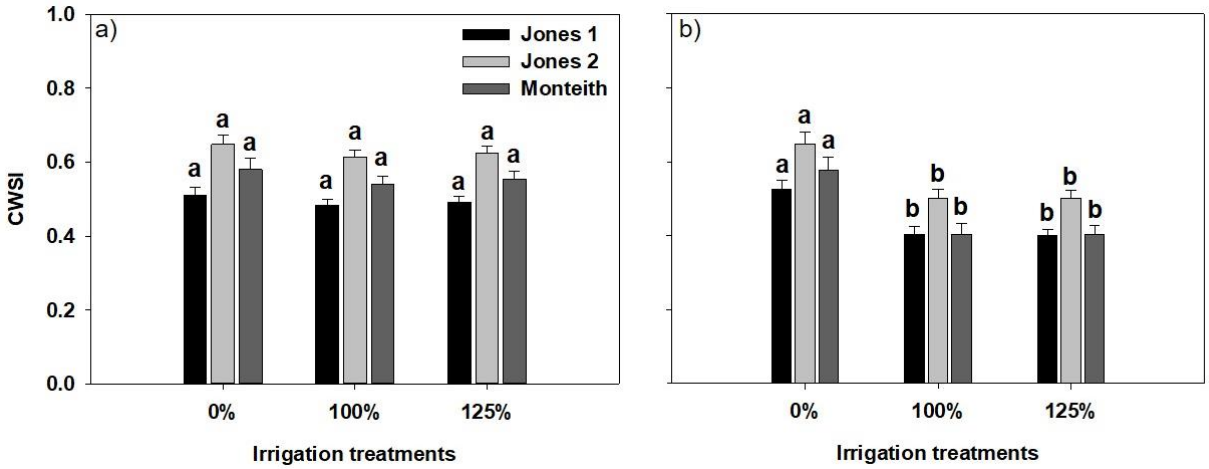

Figure 2.9. Season-long irrigation treatments crop water stress index (CWSI) averages for cotton grown in Camilla, GA. Left panel shows data from 2018, and right panel from 2020. Letters were used to compare treatment averages within each method. Bars with the same letters are not significantly different ($p<0.05$). Data represent means ± SE (2018; n = 12, 2020; n = 9).

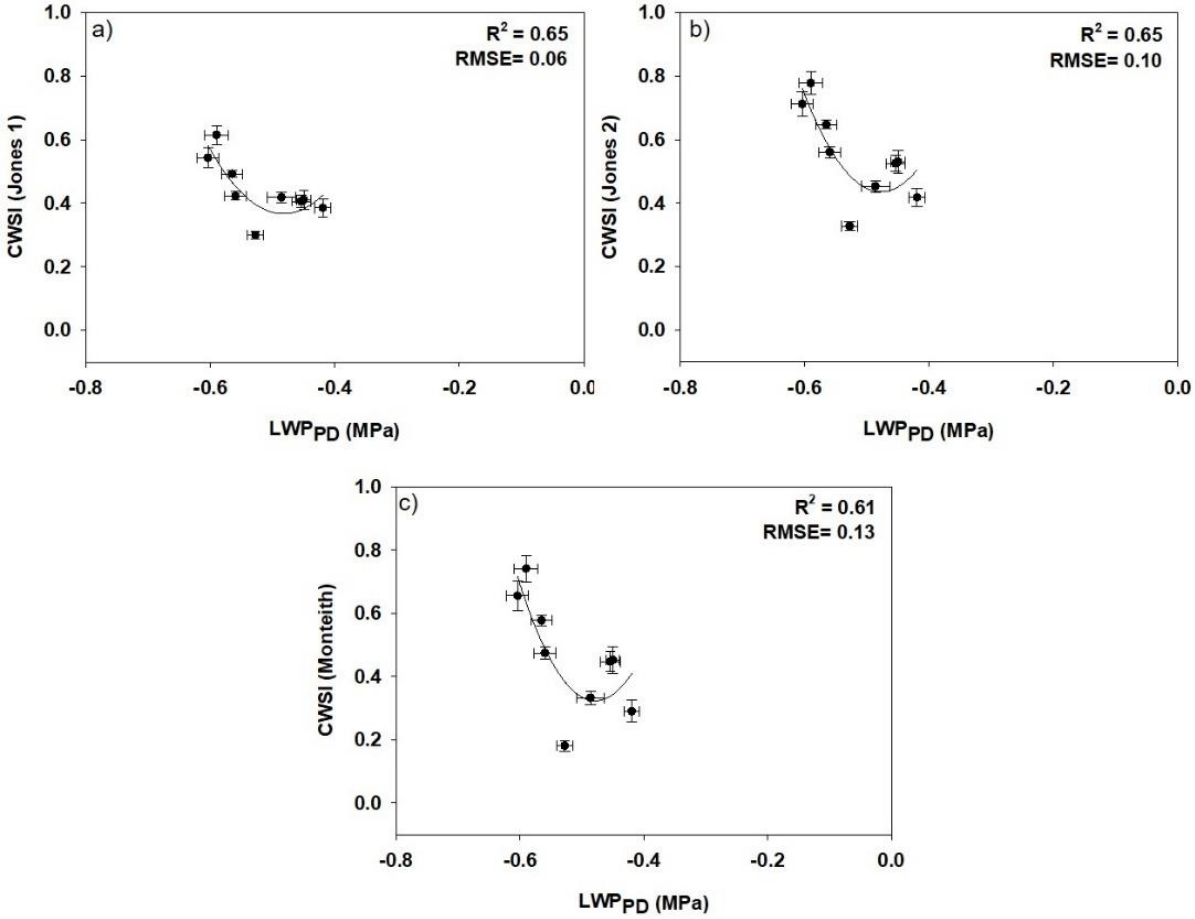

Figure 2.10. Relationship between season-long crop water stress index (CWSI) from Jones 1, Jones 2, and Monteith and predawn leaf water potential (LWP_{PD}) during the 2020 cotton growing season. Second-order polynomial was fitted between the variables ($p < 0.05$).

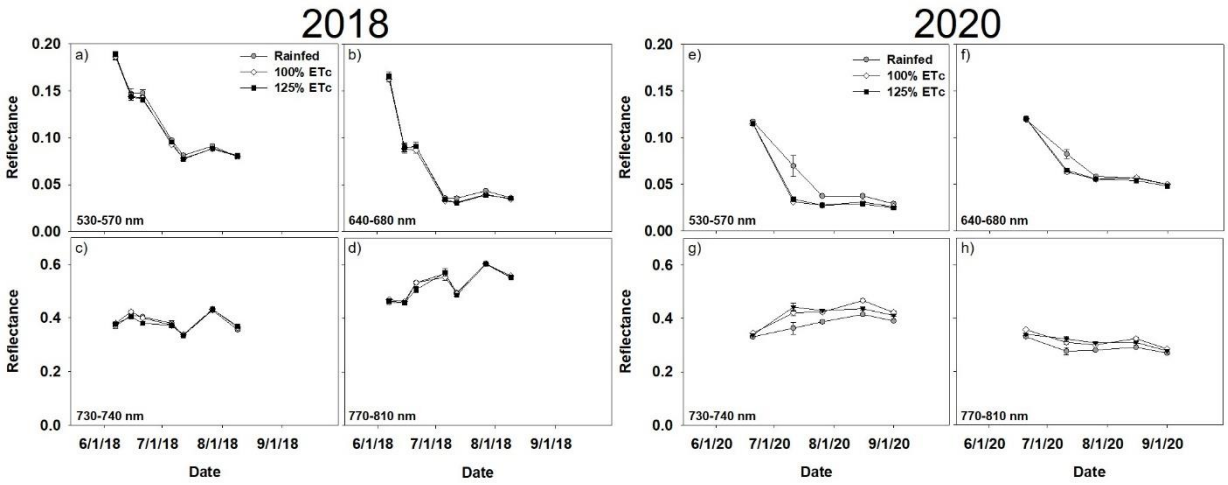

Figure 2.11. Individual band reflectance seasonal trends in Camila, GA. Bands included are green (530-570 nm) (a,e), red (640-680 nm)(b,f), red edge (730-740 nm)(c,g), and NIR (770-810 nm)(d,h). The 2018 growing season is represented on the left panel and the 2020 in the right panel. Data represent means ± SE (2018; n = 18, 2020; n = 9).

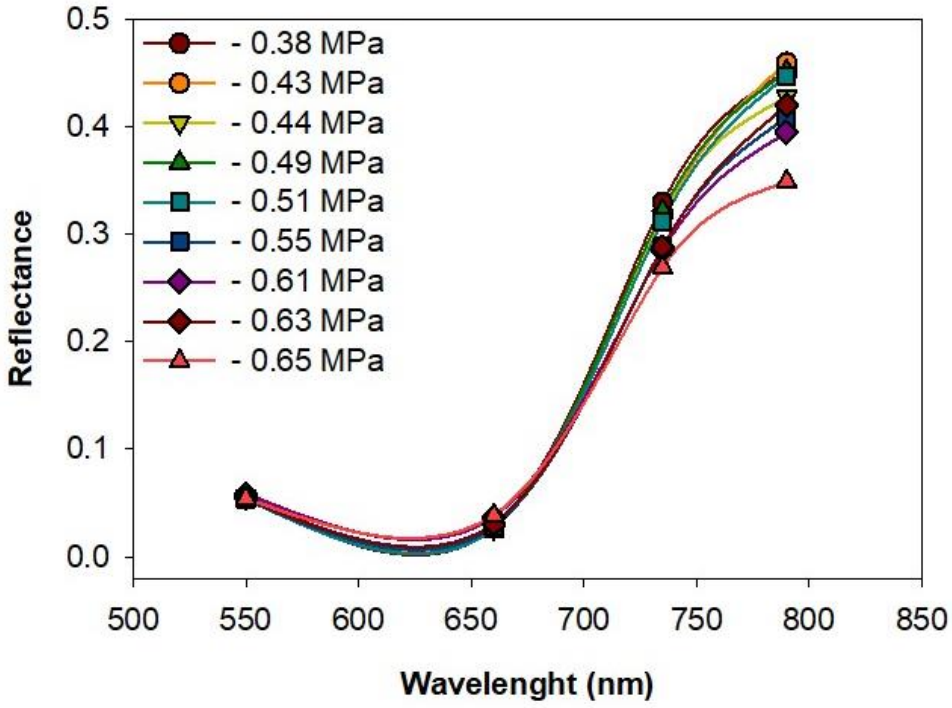

Figure 2.12. Representative average canopy reflectance with different LWP_{PD} values in the four spectral bands. Data is from 2020 at 74 days after planting (DAP). Data represent means ± SE (n = 9).

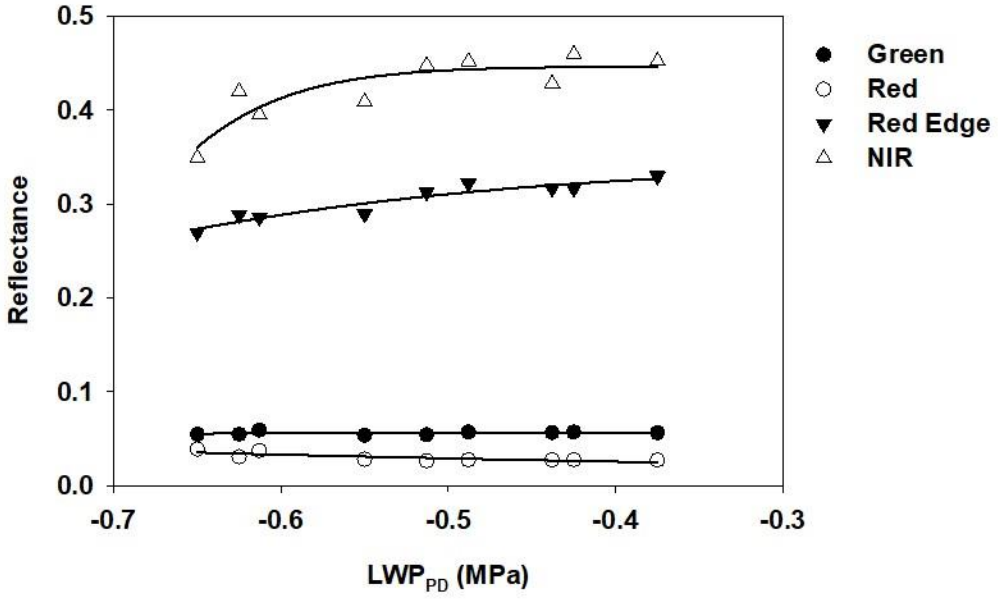

Figure 2.13. Sigmoid curve of average reflectance in the green, red, red edge, and NIR wavebands versus LWP_{PD} values.

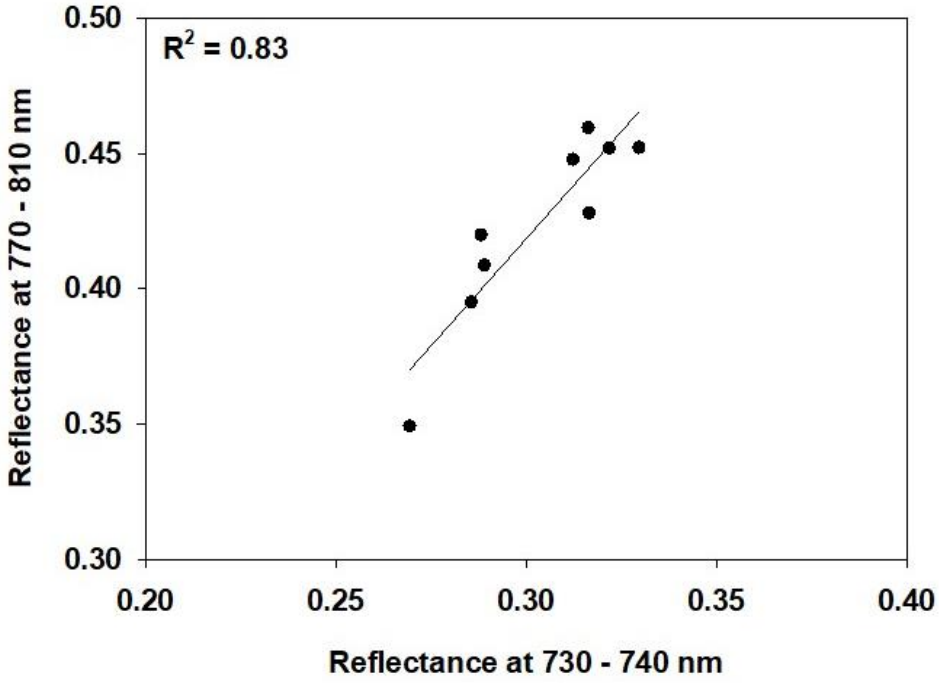

Figure 2.14. Linear regression between reflectance in the NIR (790 nm) and red edge (735 nm) bands.

CHAPTER 3

CORRELATION OF UAV AND SATELLITE-DERIVED VEGETATION INDICES WITH COTTON PHYSIOLOGICAL PARAMETERS AND THEIR USE AS A TOOL FOR SCHEDULING VARIABLE RATE IRRIGATION IN COTTON[2]

[2] Lacerda, LN., Snider, J., Cohen, Y, Liakos, V., Levi, M., and Vellidis, G. To be submitted to the *Precision Agriculture* Journal.

Abstract

Current irrigation management zones (IMZs) for variable rate irrigation (VRI) systems are static. They are delineated in the beginning of the season and used thereafter. However, recent research has shown that IMZ boundaries are transient and change with time during the growing season. The goals of this study were to explore the potential of using vegetation indices (VIs) developed from UAV and satellite images to predict cotton physiological parameters that are indicative of plant water status, to delineate dynamic boundaries of IMZs based on predicted maps, and to compare performance of VRI to conventional irrigation. A two-year study was conducted in a 38 ha commercial cotton field in southern Georgia, USA. The field was divided into alternating parallel strips (conventional, and VRI). The conventional strips were irrigated using the farmer's standard method and the VRI strips were irrigated based on soil water tension. IMZs were created based on soil texture, apparent soil electrical conductivity, and yield maps and satellite images from previous years. Throughout the growing season, VIs were calculated from UAV, PlanetScope and Sentinel-2 images. Pre-dawn Leaf water potential (LWP_{PD}) and plant height were measured at 37 locations in the field on the same day as the flights and correlated with UAV and satellite based-VIs. GNDVI (Green normalized difference vegetation index) was the best predictor of plant height with correlation values of 0.7 ($p<.0001$) and 0.84 ($p<.0001$) for 2019 and 2020, respectively. In 2019, the VRI system prescribed an average irrigation amount of 50.76 mm while the conventional irrigation applied and average of 58.42 mm. Average yield for VRI and conventional was 1247.82 and 1191.2 kg ha^{-1}, respectively. In 2020, the VRI system resulted in average yield 4.64% higher than conventional irrigation, while applying 14.03% less water.

3.1. Introduction

Cotton is an economically important fiber crop in the United States (Chastain et al., 2014). Cotton is originally a tropical crop and therefore adapted to higher temperatures, and it is often considered drought tolerant. Nevertheless, drought negatively affects seed germination and seedling establishment (Bradow and Bauer, 2010), root system growth (McMichael et al., 2010), plant height and node development (Marani et al., 1985; Wells et al., 2010), and lint yield (Wanjura et al., 2002). These negative effects are observed even in regions where average precipitation during the growing season meets crop demands (Bednarz et al., 2002). Episodic drought caused by irregular distribution of precipitation can lead to slower crop development and lower yield and water use efficiency (WUE) (Bednarz et al., 2002, Chastain et al., 2014). Additionally, crop water requirements can vary within a field due to different soil characteristics such as soil texture, moisture, and slope (Vellidis et al., 2016).

Precision irrigation consists of site-specific application of irrigation water to crops and soils based on the conditions of irrigation management zones (IMZs) (Jiang et al., 2011). In this context, variable rate irrigation (VRI) is an important practice that aims to optimize WUE in crops by applying varied rates of water in a timely manner to individual IMZs. VRI can help mitigate the effects of the spatial variability in soils and drought stress, increasing yield and maximizing WUE. In most cases, the application rates assigned to individual IMZs do not change during the growing season and therefore, do not take into account environmental changes and differences in crop growth rates. Dynamic VRI is the process of using real-time data from individual IMZs to determine the amount of irrigation water that should be applied to that zone rather than applying a constant, predetermined amount. Liakos et al. (2017) developed and demonstrated a soil moisture sensor-based dynamic VRI system. Their system installed a soil

moisture sensor node with sensors at three depths within each IMZ and used the data from the sensors to drive an irrigation scheduling decision support tool (DST) (Liakos et al., 2015; Liang et al., 2016). Thus, each IMZ received a unique prescription based on the soil moisture in that zone. Their system resulted in WUE gains ranging from 15% to 40% and yield gains of up to 4% in peanut when compared to farmer standard methods (Liakos et al., 2017). Currently, the boundaries of IMZs used for VRI systems are static. They are usually delineated when a VRI system is installed and used thereafter, ignoring temporal changes in crop water requirements during the growing season caused by the interaction between soil, plant, and environment (O'Shaughnessy et al., 2015).

Recent research has shown that it may be possible to adjust in-season IMZ boundaries using crop water status data (O'Shaughnessy et al., 2015, Cohen et al., 2017). Leaf water potential (LWP) has been identified as a reliable indicator of plant water stress (Bellvert et al., 2016; Paço et al., 2013; Argyrokastritis et al., 2015). A season-long LWP threshold of -0.5 MPa was shown to increase water productivity and yield (Chastain et al., 2016) for cotton in the southeastern US. In addition, LWP has been reported to directly affect other cotton physiological parameters that affect growth and yield such as photosynthetic assimilation rate, leaf conductance (Turner et al. 1986), and mainstem height (Chastain et al. 2016), and these parameters can in turn be used to indicate field variability in water stress. Collecting LWP data in large fields at a scale that can characterize spatial variability and be used to implement VRI is time consuming and has high labor costs. The goal of this study was to evaluate whether remote sensing can be used to estimate LWP and use those estimates to delineate irrigation management zones (IMZs). Specific objectives were to 1) explore the potential of using vegetation indices (VIs) developed from UAV and satellite images to predict cotton physiological parameters that

are indicative of plant water status, 2) delineate dynamic boundaries of IMZs based on plant parameters that addresses in-season temporal variability, and 3) compare performance of dynamic VRI to conventional irrigation.

3.2. Materials and Methods

3.2.1. Study Area

The study was conducted during the 2019 and 2020 growing seasons in a 38 ha commercial cotton field located in Miller County, Georgia, USA (31°11'21"N, 84°45'42"W). The state of Georgia has a humid subtropical climate (Kottek et al., 2006) with an average temperature ranging from 7.8°C in January to 26.5°C in July (Knox and Mogil, 2020). Precipitation is well distributed year-round with the driest months (April and October) receiving 85.3 mm and 86.6 mm, respectively, and the wettest months (July and March) receiving 133.9 mm and 122.2 mm, respectively. In Miller County, the 20-year minimum and maximum average temperatures between April and November were 17.3°C and 29.7°C, respectively (NOAA, 2021).

The field was irrigated by a center pivot system equipped with FarmScan (Advanced Ag Systems, Dothan, AL, USA) VRI controls. In both years, the field was divided into four parallel strips with two strips irrigated uniformly (conventional) and two irrigated using the dynamic VRI system described earlier (Figure 3.1). The conventional strips were irrigated using the farmer's standard irrigation method which was to apply 15 mm at each irrigation event. The strips that were irrigated using dynamic VRI in 2019 were irrigated uniformly in 2020, and the strips irrigated uniformly in 2019 were irrigated using dynamic VRI in 2020 (Figure 3.1).

Cotton was planted on May 31st in 2019 and on June 2nd in 2020. UGA Smart Sensor Array (UGA SSA) nodes were installed in 37 different locations in the field approximately 30

days after planting. The UGA SSA is a smart, wireless soil moisture sensing system that measures soil moisture at three depths that vary depending on the crop (Vellidis et al., 2013). A UGA SSA node consists of the probe used to soil moisture and the electronics package used to transmit the data to a cloud server. In this study, sensors were at depths of 15, 30 and 45 cm on the soil moisture probe. Soil moisture was measured in terms of soil water tension (SWT), which is an indicator of the energy a plant must expend to extract water from the soil matrix. Each IMZ had at least one UGA SSA node, with a total of 31 nodes installed in the VRI strips. For monitoring purposes, three UGA SSA nodes were installed in each of the two conventional strips. Nodes were installed within the row between plants about two weeks after emergence. Nodes were removed from the field a few days before harvest (Figure 3.2). SWT data were collected hourly for the duration of the growing season.

Irrigation thresholds of 50 kPa prior to first flower and 40 kPa after first flower were used to initiate irrigation (Chastain et al. 2016, Meeks et al. 2017). The daily weighted average SWT of the three sensors at each node at 07:00 AM was used to determine if an IMZ required irrigation. The weighting factors used to calculate the weighted average SWT characterize the estimated distribution of roots at the three sensor depths. Eq. 1 shows the weighting factors used after canopy closure (ACC). The dynamic VRI DST was used to determine the amount of irrigation water needed to bring the soil profile in that IMZ back to the desired soil moisture

condition using the weighted average SWT. In this study, the desired soil moisture condition was 80% of field capacity which leaves "room" for the soil profile to absorb precipitation events.

$$\textit{Weighted avg SWT} = (0.5 \times \textit{SWT at 0.15 m}) + (0.2 \times \textit{SWT at 0.3 m}) + (0.3 \times \textit{SWT at 0.45 m}) \quad (1)$$

3.2.2. Irrigation Management Zones delineation

The VRI strips were divided into 25 IMZs in 2019 and 29 in 2020. The IMZ delineation was based on five data layers that included apparent soil electrical conductivity (EC_a), elevation, NDVI, yield maps from previous years, and soil texture data (Figure 3.3). EC_a was measured at 0-0.3 m (shallow) and 0-0.9 m (deep) using the Veris 3100 instrument (Veris, Salinas, KS, USA). Because deep EC_a measurements integrate the entire root zone, deep EC_a data were used to create an EC_a map of the whole field and used as a layer for IMZ delineation in both years. A digital elevation model (DEM) of the field was developed from elevation data collected from a tractor equipped with RTK GPS with approximately 2 cm x, y, and z accuracy. In 2019, 75 soil core samples were collected from the field and analyzed. Each core sample was divided into one superficial layer of 7.6 cm and three additional layers of approximately 15 cm. Percent clay content from 38 to 53 cm was used to create a percent clay content map of the field that was used in both years to delineate IMZs. Kriging was used to interpolate between sampling locations. Yield and NDVI maps from 2017 were used as data layers in 2019, while in 2020, yield and NDVI maps from 2019 were used. PlanetScope CubeSat (Planet Labs, San Francisco, CA, USA) satellite images from July 2017 and July 2019 were used to develop the NDVI maps.

The IMZ delineation process was done manually using ArcGIS (ESRI, Redlands, CA, USA) after visual analysis of all data layers to identify areas of variability. A manual process

was performed with the aim to capture as much variability as possible in the field within individual IMZs – something that was not achievable when using common statistical methods for IMZ delineation. The larger numbers of zones resulted in the installation of a dense network of sensor nodes in the VRI strips. In 2020, a second IMZ map was delineated mid-season based on plant development maps generated before the flowering stage.

3.2.3. Field measurements

Physiological measurements of cotton plants were carried out weekly from July until the last week of irrigation in late September in both years at the location of the UGA SSA nodes. There were 9 sampling days in 2019 and 10 in 2020. Predawn LWP (LWP_{PD}) was collected using a model 615 Scholander pressure chamber (PMS Instruments, Albany, OR) from two plants at 31 node locations in in 2019, and in all 37 nodes in 2020. Measurements were taken between 03:00 AM and 06:00 AM. A leaf including the petiole was cut from two plants and LWP_{PD} was measured for each leaf. Selected plants were adjacent to the UGA SSA node. The dates of field measurements and the number of each measurement made are shown in Table 1.1.

Plant height measured from the ground to the apical meristem was collected from five plants adjacent to the UGA SSA nodes. The same five plants were used throughout the growing season. A LI-6800 portable photosynthesis system (LI-COR, Lincoln, NE, USA) was used to collect midday photosynthetic assimilation rate (A_n) and stomata conductance to H_2O (g_s). Leaf chamber settings included a flow rate of 600 µmol s^{-1}, reference CO_2 = 400 µmol mol^{-1}, air temperature = ambient temperature, relative humidity = 60 ± 15%, and chamber light intensity = 1500 µmol m^{-2} s^{-1} photosynthetically active radiation (PAR). The leaf was clamped into the chamber until steady-state conditions were reached (60 to 120 seconds per sample). Midday measurements were performed from 11:30 AM to 2:30 PM on the fourth mainstem node below

the terminal for two plants adjacent to the sensor node. Because of the time needed to make these measurements, they were limited to the two southern strips (Figure 3.1). Measurements were made at 18 sensor node locations in 2019 and at 15 sensor node locations in 2020. Yield data was collected at the time of harvest in the whole field with a cotton picker equipped with a yield monitor. Yield data was cleaned and processed using ArcGIS (ESRI, Redlands, CA, USA) to create yield maps for both years.

3.2.4. UAV and satellite imagery acquisition and processing

Remote sensing data was collected in two ways. An UAV equipped with a multispectral camera was flown weekly on the same days as field data collection. Satellite images acquired from the day field data were collected and three days before and after field data were collected were downloaded from two different satellite system platforms. The additional days were downloaded to ensure the availability of a cloud-free image. Images were used to calculate a variety of vegetation indices (VIs). The PlanetScope satellite constellation is one of the three constellations operated by Planet Labs (San Francisco, CA, USA). It currently has approximately 130 satellites imaging the earth's land surface daily at a spatial resolution of 3.7 m and a temporal resolution of less than one day (Planet labs, 2020). The second satellite platform used was Sentinel-2 operated by the European Space Agency (ESA). Sentinel-2 is a two-satellite platform operating in the same orbit 180° apart providing data in 13 spectral bands with bandwidths ranging from 490 nm to 1375 nm. Sentinel-2 has a revisit time of 5 days and spatial resolution of 10, 30, and 60 m.

PlanetScope images provide data in the blue (455-515 nm), green (500-590 nm), red (590-670 nm) and NIR (780-860 nm) regions of the spectrum. Surface reflectance data were downloaded directly from the Planet Labs website (https://www.planet.com) and a factor

(10,000) was applied to obtain correct reflectance data (Planet Labs, 2019). Sentinel-2 images were downloaded from the United States geological Survey (USGS) Earth Explorer website (https://earthexplorer.usgs.gov/) and bands 2 (490 nm), 3 (560 nm), 4 (665 nm) and 8 (842 nm) at 10 m spatial resolution, and 11 (1,610 nm), and 12 (2,190 nm) at 20 m resolution were used to calculate VIs. The Semi-Automatic Classification Plugin (SCP) in QGIS 3.14.0 (QGIS Development Team, 2020) was used to perform atmospheric correction on all Sentinel-2 images.

The UAV was a 3DR Solo quadcopter (3D Robotics, Berkeley, CA, USA) equipped with a Parrot Sequoia (MicaSense, Seattle, WA, USA) camera that acquires images in four spectral bands: Green (530-570 nm), Red (640-680 nm), NIR (770-810 nm) and Red Edge (730-740 nm). UAV flights were performed at 120 m altitude with 75% front and side lap resulting in a resolution of approximately 12.5 cm per pixel. UAV image processing was performed using Pix4Dmapper software (Pix4D SA, Lausanne, Switzerland) version 4.4.12. Single images were stitched to create reflectance map mosaics of all four bands. During the stitching process, geographic correction was performed using six ground control points with known coordinates distributed around the perimeter of the field. Calibration panel images taken after each flight were used to perform radiometric calibration of the final reflectance maps.

ArcGIS (ESRI, Redlands, CA, USA) software was used for remote sensing data extraction. Images from the UAV and satellite platforms were used to calculate the VIs shown in Table 3.2 that were selected based on their ability to quantify specific plant growth parameters. The VIs used were also a function of the spectral bands available. Average VI values were extracted from the 10 m radius area around each soil moisture sensor node and from the delineated IMZs. A 5 m buffer was created between zones, and images from all 3 platforms were overlapped to minimize potential data extraction errors due to geographic accuracy. Pearson

correlation ($p<.0001$) was used to study correlation between VIs and LWP and plant height, and a sigmoid curve with 4 parameters was used to explore VIs response to changes in plant height during the whole season.

3.3. Results and Discussion

3.3.1. Meteorological data

The two growing seasons that were included in this study presented sharply differing weather conditions (Figure 3.4). Precipitation during the 2019 growing season was 485 mm and skewed towards the beginning of the growing season. Precipitation was higher and more evenly distributed during the 2020 growing season with 699 mm received. In 2020, the field received 180 mm of precipitation from planting to first flower, 394 mm from first flower to first open boll, and 125 mm from first open boll to harvest. In 2019, precipitation was similar from planting to first flower (165 mm), 206 mm from first flower to first open boll, and an extended period without any precipitation in September and October. In the last weeks before harvest, 114 mm of precipitation were observed. Cotton plants' sensitivity to water stress increases during squaring (Wrona et al., 1999) and reaches its maximum during the flowering stage (Snowden et al., 2014). Consequently, without irrigation, cotton would have experienced significant stress during the latter part of the 2019 growing season.

Minimum and maximum temperatures were similar during the first three months of the season in both years. Maximum temperatures from June to September in 2019 were 33.6 °C with the highest average temperatures in September (34.4 °C). During 2020, maximum temperature for the same period averaged 32.3 °C with the warmest temperatures observed in August. October was the coolest month in both years with minimum and maximum temperatures of 16.9 and 29.4 °C in 2019 and 12.1 and 24.7 °C in 2020.

3.3.2. Spatial and temporal variability in SWT and crop parameters

Figure 3.5 shows the season-long SWT, $LWP_{PD,}$ A_n, and g_s distributions among the IMZs delineated in 2019 and 2020. Data analysis was divided into before canopy closure (BCC) and after canopy closure (ACC) due to saturation of the NIR-based indices at full canopy (Hunsaker et al. 2003) and the differences in the cotton plant physiological responses between the vegetative and reproductive stages.

3.3.2.1. 2019

In 2019, five field-measurement days took place during the BCC period and four during the ACC period (Figure 3.5a). Canopy closure was achieved approximately 100 days after planting (DAP) between the last week of August and first week of September. All four measurements exhibited within-season and within- and between-zone variability. SWT was significantly higher ACC than BCC. During early plant development, the soil profile in IMZs 1, 4, 6, 7, 10, 12, 15, 17, 20 and 25 maintained adequate soil moisture from precipitation alone with SWT values averaging 33 kPa. As indicated earlier, the pre-bloom irrigation scheduling threshold was 50 kPa. Zone 7 was drier with an average SWT of approximately 70 kPa despite irrigation. The highest within-zone variability in soil moisture was observed in zones 3, 5, 8, 18, 23 and 24. The SWT in these zones varied by more than 80 kPa suggesting that for one or more days during pre-bloom, rainfall and irrigation together were not sufficient to keep the soil profile within the desirable SWT range. This is indicative of sandier soils where SWT can increase sharply because of the soil's low water holding capacity. SWT greater than 70 kPa at the pre-bloom stage may result in slower plant growth and significant yield loss (Collins et al., 2011; Meeks et al. 2017). The remaining IMZs exhibited moderate variability with SWT values all below 70 kPa, indicating that in these zones soil moisture was adequate to ensure good growth.

With the onset of the reproductive stage, cotton slows its vegetative growth but increases its water requirements. As indicated earlier, the irrigation threshold during the reproductive stage is 40 kPa. Increased water demand coupled with decreased rainfall from September onwards should have resulted in more irrigation. Instead, the grower who managed this field decreased the frequency of irrigation because of disease pressure caused by the frequent rains earlier in the season. As a result, during the latter half of the reproductive period, soils were drier and higher SWT was recorded in most of the field. Of the 25 IMZs, only zones 4 and 25 had average SWT below 40 kPa ACC. There was high soil moisture variability between these zones at this stage, and high within zone variability in at least 12 IMZs with SWT values varying from 40 to 60 kPa.

Spatial and temporal variability was also seen in the plant's physiological indicators. There was a significant decrease in LWP_{PD} inverse of the trend shown by the SWT data with a strong negative correlation between these two variables. Prior to bloom, LWP_{PD} in all zones varied between 0 and -0.6 MPa which is above the threshold (-0.8 MPa) for mainstem growth inhibition (Chastain et al. 2016). ACC, LWP_{PD} values decreased significantly below -0.6 MPa displaying varied levels of stress. The same trends were observed in stomatal conductance and photosynthetic assimilation rate. The water stress observed after bloom caused a decrease in g_s that in turn affected the A_n. The largest difference in average assimilation rate was observed between zones 20 and 23 with values of 30.8 and 14.5 µmol $m^{-2}s^{-1}$, respectively. Turner et al. (1986) observed a decrease in photosynthetic rates of 20 µmol $m^{-2}s^{-1}$ when LWP decreased from -0.4 to -1.6 MPa. The changes in photosynthetic rates were associated with decreased leaf conductance.

3.3.2.2. 2020

In 2020, new IMZ boundaries were delineated at the end of the vegetative stage based on predicted plant height map. At the ACC stage IMZ boundaries followed map 2 (Figure 3.5 (b)). Soil moisture was consistently higher during 2020 growing season than the 2019 growing season (Figure 3.5b). This was especially true for ACC. In contrast to 2019, SWT between- and within-zone variability was higher BCC with zones 1, 3, 6, 7, 9, 14, 17 22, and 24 showing values at field capacity or below with little change over time, and zones 23, 27 and 28 showing a greater range of values from wet soil (< 33 kPa) to very dry soil (>100 kPa). During September and October 2020, there were frequent precipitation events associated with tropical storms which led to very low SWT values in all IMZs (Figure 3.5b). This was reflected in the physiological measurements. LWP, g_s and A_n were similar to 2019 BCC but much higher ACC. Although the measurements were higher ACC in 2020 than in 2019, in some areas of the field, the plants were damaged from the high winds associated with the tropical storms and this likely depressed the photosynthetic rate.

3.3.3. Relationships among yield, plant height, SWT and physiological parameters

Regression analyses were used to evaluate the relationship between soil moisture and plant water status and how the water status related to leaf stomatal conductance and assimilation rate of CO_2 in both years. Second-order polynomial regressions were developed between SWT, LWP_{PD}, A_n, and g_s (Figure 3.6). Average values of the measurements taken at each sensor node at each sampling date were used in all regressions. Measurements were taken at 31 nodes on 9 dates in 2019 and 37 nodes on 10 dates in 2020. A strong non-linear relationship (R^2= 0.7, p<.0001) between SWT and LWP_{PD} was observed in 2019. A strong non-linear relationship was also observed between LWP_{PD} and A_n (R^2= 0.62, p<.0001) and g_s (R^2= 0.60, p<.0001). In 2020,

relationships between SWT and $LWP_{PD,}$ LWP_{PD} and A_n, and LWP_{PD} and g_s were all weak with coefficients of determination of 0.07, 0.18 and 0.12, respectively. This is primarily because the measurements were relatively consistent in 2020 because the soil moisture did not vary as much as in 2019. The data point cluster observed in the regression between SWT and LWP_{PD} when SWT values were low may be related to the inability of the soil moisture sensors used in the UGA SSA probes to accurately measure SWT at near saturation conditions.

The difference in the relationship between LWP_{PD} and the other two physiological parameters indicated a limiting effect of varying degrees of water stress in the cotton photosynthetic rate in 2019. The absence of water stress in 2020 indicated that the variability in g_s and A_n were caused by other factors. In addition, most data points furthest from the curve in 2019 were from plots 22, and 23 that were located in the lower eroded parts of the field where plant growth was limited.

Higher average plant growth was generally observed in IMZs that received a higher total amount of water during the growing season except for IMZs located in eroded areas of the field (see Figure 3.1). In these areas, plant growth was limited irrespective of the amount of water received. In 2019, IMZs that received less than 700 mm of precipitation and irrigation presented an average height of 1.07 m, while IMZs that received more than 700 mm of water had an average height of 1.14 m. In 2020, all IMZs received a total water amount higher than 700 mm. IMZs with average total water between 700 and 750 had an average height of 0.87 m, and IMZs that received more than 750 mm had an average height of 0.99 m.

Plant height averages from each IMZ for the entire growing season were plotted against final yield (Figure 3.7) to determine the relationship between the two variables. In 2019, a strong relationship between height and yield was observed ($R^2 = 0.65$, $p<.0001$) with taller plants

achieving higher yields. A weaker relationship was observed in 2020 ($R^2 = 0.56$, $p<.0001$) due to a decreased yield observed in plants taller than 1 m. The decrease in yield can be attributed to the damage caused in the plants during the tropical storms. Taller plants suffered from strong winds were blown over and lodging was observed in these areas of the field. As a result, these plants were not harvested as efficiently. High soil moisture may also have resulted in additional vegetative growth. In spite of a weaker relationship in 2020, results from this study were similar to those of Sui et al. (2013) in which they observed higher plant heights and yield in plots with more available water (irrigated) when compared to dryland.

3.3.4. Comparison of VIs, plant height and LWP_{PD}

Pearson's correlation was used to compare the response of VIs developed from UAV imagery to plant height for 2019 and 2020 (Table 3.3). The overall correlation of the entire season indicated that all VIs showed high positive correlation with plant height during both years. GNDVI had the strongest overall correlation with values of 0.72 ($p<.0001$) and 0.84 ($p<.0001$) for 2019 and 2020, respectively, followed by CIgreen with values of 0.72 ($p<.0001$) for 2019, and 0.82 ($p<.0001$) for 2020. The lowest overall correlation observed in both years was between plant height and GRVI with values of 0.51 ($p<.0001$) in 2019, and 0.70 ($p<.0001$) in 2020. Within-season correlations from 60 to 77 days after planting (DAP) in 2019, and from 64 to 71 DAP were the highest with all values above 0.7 ($p<.0001$). VIs developed from PlanetScope images showed similar correlations to plant height as VIs from the UAV. However, due to lower spatial resolution UAV results were preferred.

Overall VI values calculated from UAV, PlanetScope and Sentinel-2 were correlated with LWP_{PD} measurements in both years (Table 3.4). The majority of VIs had significant correlation with LWP_{PD} except GRVI, OSAVI and NLI calculated from UAV images in 2019 and CIgreen

and GNDVI calculated from Sentinel-2 images in 2020. Although significant, correlations were weak to moderate for the majority of indices from the three remote sensing platforms. The strongest correlations were observed in 2019 for CIgreen and GNDVI (-0.63 and -0.61, p<.0001, respectively) calculated from Sentinel-2 images, followed by GBNI (-0.56, p<.0001) calculated from Planet Scope, NDVI (-0.55, p<.0001), OSAVI and NLI (-0.52, p<.0001), NDWI (-0.49) and NMDI (-0.47, p<.0001) from Sentinel- 2. In 2020 only OSAVI (-0.49, p<.0001) calculated from PlanetScope and GBNI (0.42, p<.0001) calculated from Sentinel-2 showed moderate correlation with LWP_{PD}.

In contrast to the results from this study, Beeri et al. (2018) found that GBNI, NDWI and NMDI were strongly correlated with LWP (R^2 = 0.71, 0.71, 0.53 p<.0001, respectively) in cotton fields in Israel and Australia. The higher correlations in the Beeri et al. (2018) study can be attributed to the fact that LWP values were collected from the wettest and driest parts of the field, while in the current study, LWP data from the whole field were used independently of the level of stress. The low LWP_{PD} can also explain why correlations were low in 2020 across almost all VIs analyzed. Additional results from Beeri et al. (2018) reported strong correlations between LWP and vigor VIs such as NDVI (R^2 = 0.69), which corroborates present results. The correlations observed in this study were not strong enough to develop LWP prediction models with high accuracy. This is likely because the range of LWP_{PD} measured was small compared to studies conducted in semiarid or arid environments.

3.3.5. Plant height prediction

A strong positive relationship between plant height and GNDVI was observed in both years, with GNDVI values increasing with increased plant growth. A logistic model was used to quantify this relationship (Figure 3.8). Plant height prediction using GNDVI was better in 2020

with an R^2 value of 0.72 and RMSE of 15.27. In 2019, the weaker relationship between the two variables was most likely caused by the higher number of dates collected at the end of the season when increased assimilate demands by the fruit causes vegetative growth to significantly decrease or to cease completely (Wells et al., 2010). Therefore, changes in the VI values at this stage are not associated with plant growth.

Lower and upper asymptote parameters in 2019 ranged from 40.07 to 147.48 and from 44.08 to 123.72 in 2020, while the inflection point in both years was at 0.74 in 2019, and 0.72 in 2020. The similar lower asymptote indicated that GNDVI and plant height have a weak relationship when the crop is in the initial development stage and would not result in a high accuracy prediction model, once changes in plant growth at this stage are not detected by GNDVI. Similar analysis can be made when plant height was higher than 147.48 in 2019, and 123.72 in 2020. The upper asymptote represented the point of saturation, in which the VI was not able to sense the small changes in height. The range between lower and upper asymptotes represents the period in which it would be more suitable to predict plant height using UAV. The point of highest increase in growth is represented by the inflection point when GNDVI values were around 0.74 and 0.72 in 2019 and 2020, respectively. Based on results, the most indicated period to the development of height prediction models for IMZ delineation would be between 60 and 80 days after planting. Similar results were observed by Raper & Varco (2015). NDVI and GNDVI showed a strong relationship with plant height during the period from bud formation to first flower, which commonly occurs around 60 to 70 days after planting (Robertson et al., 2007).

In 2020, a predicted plant height map was created using a linear model fitted between GNDVI and measured plant height at 64 DAP (Figure 3.9). A strong relationship between the

two variables (R^2 =0.72, p<.0001) was observed in this period, as indicated by the logistic model (see Figure 3.8), with a root mean square error (RMSE) of 11.2 cm. The predicted map (Figure 3.10a) shows great similarity to the final yield map (Figure 3.10b). A strong non-linear relationship (R^2 =0.58, p<.0001) was observed between zones height and yield averages. This relationship increases to 0.77 when zones 15, 19 and 23, that did not follow the same relationship, are excluded from the regression.

The correlation between plant growth and LWP_{PD} and between plant growth and cotton yield can serve as an indicator of plant status at the beginning of the season during the vegetative stage and enable the delineation of new IMZs that address temporal changes caused by the interaction of plant, soil, and environment.

3.3.6. Comparison between irrigation methods

The precipitation difference between the two growing seasons can be illustrated by the difference in irrigation applied and irrigation events (Table 3.5). A total of 7 irrigation events occurred in 2019 to compliment the 485 mm of precipitation. Irrigation was triggered mainly during September when precipitation was low. The VRI strips received an average of 86 mm of water from irrigation and an average of 87 mm was prescribed to the uniform strips. As described earlier, in 2019, the crop experienced water stress in September and October as the grower reduced the frequency of irrigation because of disease pressure (see Figure 4). Although there were no significant differences in the overall water applied across the field, the amount of water applied to individual IMZs differed at every irrigation event and was determined by the dynamic VRI DST. The average yield for the conventional strips was 1890 kg ha^{-1} while yield of the VRI strips averaged 1794 kg ha^{-1} which is a 5.21% difference in yield. IWUE for the VRI strips was 20.74 kg/mm and 21.67 for the conventional. This finding contradicts other dynamic

VRI studies conducted in southern Georgia where applying the UGA SSA-based dynamic VRI system to peanut resulted in yield increases of up to 4% and IWUE gains of up to 40% (Liakos et al., 2017). The lower dynamic VRI yields may have been affected by the IMZs the included a highly eroded area of the field (Figure 1) and where yields in 2019 were very low (Figure 2).

Because there were regular precipitation events throughout the 2020 growing season, the field was irrigated only four times, three of which took place in October. The dynamic VRI system prescribed an average irrigation amount of 51 mm while the conventional irrigation applied and average of 58 mm. Average yield for VRI and conventional was 1,248 and 1,191 kg ha^{-1}, respectively. In 2020, the VRI system resulted in an average yield 4.6% higher than conventional irrigation, while applying 14.0% less water. IWUE was 24.57 kg/mm in the VRI and 20.39 kg/mm in the conventional strips. As in 2019, the average yields may be affected by the highly eroded area in the field.

3.4. Conclusion

Results from this study show that management zones change spatially and temporarily (within and between growing seasons). This temporal variation within a growing season caused by the interaction of soil, plant and environment can be addressed by monitoring plant growth patterns and physiological responses. Remotely sensed data in the visible and NIR regions of the spectrum can be used in the form of VIs to estimate plant height in cotton with high accuracy between 50 and 80 days after planting when cotton plants are close to the flowering stage. The ability to predict plant height for the whole field at high spatial resolution facilitates the identification of cotton growing patterns in the field during crop development. IMZ boundaries can then be adjusted according to within season plant feedback during the vegetative stage.

Results showed that VIs were also significantly correlated with LWP however, the correlations observed were not strong enough to develop LWP prediction models with high accuracy.

The 2019 and 2020 growing seasons were used to evaluate the potential advantages for Georgia cotton growers to irrigate using variable rates that respond in real time to crop requirements. The second year of the study (2020) was used to evaluate the feasibility of using multispectral images to delineate dynamic IMZs if and when needed. Although in this field, soil and landscape variability play a major role in affecting yield, results from the second year suggest that VRI can help reduce the amount of water applied without decreasing yield and consequently increasing irrigation water use efficiency.

Further research is needed to explore the advantages of VRI and the delineation of IMZs that change during the season. The relationship between visible and Infrared-based VIs and water status needs to be further evaluated. A larger data set from different fields exposed to different conditions can help test stability of these correlations. The potential of estimating LWP from remotely sensed multispectral data can make dynamic IMZ delineation feasible provided that images are available at low cost for use by farm consultants.

3.5. References

Argyrokastritis I.G., Papastylianou, P.T., Alexandris, S. (2015). Leaf water potential and crop water stress index variation for full and deficit irrigated cotton in Mediterranean conditions. *Agriculture and Agricultural Science Procedia* 2: 463-470.

Beeri, O., Mey-tal, S., Raz, Y., Rud, R., Pelta, R. (2018). Detecting variability in plant water potential with multi-spectral satellite imagery. In: The 14th International Conference on Precision Agriculture. https://www.ispag.org/Proceedings

Bednarz, C.W., Richie, G., Hook, J., Yager, R., Cromer, S., Cook, D., and Griner, I. (2002). Cotton crop water use and irrigation scheduling. In: A.S. Culpepper, editor, 2002 Georgia Cotton Research-Extension Report. Univ. of Georgia, Athens, GA. P. 61-64.

Bradow J.M., and P.J. Bauer. (2010). Germination and Seedling Development. In: Stewart J.M., Oosterhuis D.M., Heitholt J.J., Mauney J.R. (eds) Physiology of Cotton. Springer, Dordrecht.

Chastain D.R., Snider J.L., Collins G.D., Perry C.D., Whitaker J., and Byrd S.A. (2014). Water deficit in field-grown *Gossypium hirsutum* primarily limits net photosynthesis by decreasing stomatal conductance, increasing photorespiration, and increasing the ratio of dark respiration to gross photosynthesis. *Journal of Plant Physiology* 171, 1576-1585.

Chastain D.R., J.L. Snider., G.D. Collins, C.D. Perry, J. Whitaker, S.A. Byrd, D.M. Oosterhuis, W. Porter. (2016). Irrigation Scheduling using predawn leaf water potential improves water productivity in drip-irrigated cotton. *Crop Science* 56: 3185-3195.

Cohen Y., Alchanatis, V., Saranga, Y., Rosenberg, O., Sela, E., and Bosak, A. (2017). Mapping water status based on aerial thermal imagery: comparison of methodologies for upscaling from a single leaf to commercial fields. *Precision Agriculture* 18: 801-822.

Collins, G.D., J. Whitaker, C. Meeks, and C. Perry. (2011). Management of cotton using subsurface drip irrigation. In: G.D. Culpepper, editor, 2011 Georgia Cotton Research-Extension Report. Univ. of Georgia, Athens, GA. p. 10–13.

Gao, B.C. (1996). NDWI–A normalized difference water index for remote sensing of vegetation liquid water from space. *Remote Sensing of Environment* 58, 257-266.

Gitelson, A.A., Kaufman, Y.J., and Merzlyak, M.N. (1996). Use of a green channel in remote sensing of global vegetation from EOS-MODIS. *Remote Sensing of Environment* 58, 289–298.

Gitelson, A.A., Viña, A., Arkebauer, T.J., Rundquist, D.C., Keydan, G., and Leavitt, B. (2003). Remote estimation of leaf area index and green leaf biomass in maize canopies. *Geophysical Research Letters* 30, 1248.

Goel, N. S. and Qi, W. (1994). Influences of canopy architecture on relationships between various vegetation indices and LAI and FPAR: A computer simulation. *Remote Sensing Review* 10, 309–347.

Hunsaker, D.J., Pinter, P.J. Jr., Barnes, E.M. and Kimball, B.A. (2003). Estimating cotton evapotranspiration crop coefficients with a multispectral vegetation index. *Irrigation Science* 22:95-104.

Jiang, Q., Fu, Q., and Wang, Z. (2011). Delineating site-specific irrigation management zones. *Irrigation and Drainage* 60: 464-472.

Liang X., Liakos, V., Wendroth, O.,Vellidis, G. (2016). Scheduling irrigation using an approach based on the van Genuchten model. *Agricultural Water Management* 176: 170-179.

Liakos, V., Porter, W., Liang, X., Tucker, M.A., McLendon, A., Vellidis, G. (2017). Dynamic variable rate irrigation – a tool for greatly improving water use efficiency. *Advances in Animal Biosciences* 8(02):557-563.

Liakos, V., Vellidis, G., Tucker, M., Lowrance, C., & Liang Xi (2015). A decision support tool for managing precision irrigation with center pivots. In: J.V. Stafford (Ed.), Precision Agriculture '15 - Papers Presented the 10th European Conference on Precision Agriculture (10ECPA), Tel Aviv, Israel, p677-683

Knox, P. and Mogil, M. (2020). The Weather and Climate of Georgia: Georgia's "Peachy" Weather and Climate: Something for Everyone. *Weatherwise*, 73:5, 40-41.

Kottek, M., Grieser, J., Beck, C., Rudolf, B., Rubel, F. (2006). World Map of the Köppen-Geiger climate classification updated. *Meteorologische Zeitschrift* 15, 259-263.

Marani, A., Baker, D.N., Reddy, V.R., J.M. McKinion. (1985). Effect of Water Stress on Canopy Senescence and Carbon Exchange Rates in Cotton. *Crop Science*, 25, 798-802.

McMichael B.L., Oosterhuis, D.M. , Zak, J.C., and Beyrouty, C.A. (2010). Growth and Development of Root Systems. In: Stewart J.M., Oosterhuis D.M., Heitholt J.J., Mauney J.R. (eds) Physiology of Cotton. Springer, Dordrecht.

Meeks, C.D., Snider, J.L., Porter, W.M., Vellidis, G., Hawkins, G., and Howland, D. (2017). Assessing the Utility of Primed Acclimation for Improving Water Savings in Cotton using a Sensor-Based Irrigation Scheduling System. *Crop Science* 57, 2117-2129.

NOAA- National Oceanic and Atmospheric Administration. (2021). https://www.ncdc.noaa.gov/climate-monitoring/. Accessed 06 January 2021.

O'Shaughnessy S.A., Evett, S.R., Colaizzi, P.D. (2015). Dynamic prescription maps for site-specific variable rate irrigation of cotton. *Agriculture Water Management* 159: 123-138.

Planet (2020). Planet Imagery Product Specification. Accessed 07 January 2021.

Planet (2019). Planet Surface reflectance Version 2.0. Accessed 07 January 2021.

Paço T.A., Ferreira, M.I., Pacheco, C.A. (2013). Scheduling peach orchard irrigation in water stress conditions: use of relative transpiration and predawn leaf water potential. *Fruits*, 68(2): 147-158.

QGIS Development Team. (2020). QGIS Geographic Information System; Open Source Geospatial Foundation.

Raper, T.B., and Varco, J.J. (2015). Canopy-scale wavelength and vegetative index sensitivities to cotton growth parameters and nitrogen status. *Precision Agriculture* 16, 62-76.

Robertson, B., Bednarz, C., Burmester, C. (2007). Growth and Development – First 60 days. Cotton Physiology Today Newsletter, National Cotton Council, vol. 13 (2).

Rouse, J., Haas, R., Schell, J., and Deering, D. (1974). Monitoring vegetation systems in the Great Plains with ERTS. NASA SP-351, Washington, DC, pp. 309-317.

Rondeaux, G., Steven, M., Baret, F. (1996). Optimization of soil-adjusted vegetation indices. *Remote Sensing of Environment* 55, 95-107.

Snowden, M.C., Ritchie, G.L., Simao, F.R., and Bordovsky, J.P. (2014). Timing of Episodic Drought Can Be Critical in Cotton. *Agronomy Journal* 106, 452-458.

Sui, R., Fisher, D.K., and Reddy, K.N. (2013). Cotton Yield Assessment Using Plant Height Mapping System. *Journal of Agricultural Science* 5:23.

Tucker, C.J. (1979). Red and photographic infrared linear combinations for monitoring vegetation. *Remote Sensing of Environment* 8, 127-150.

Turner N.C., Hearn, A.B., Begg, J.E., and Constable, G.A. (1986). Cotton (*Gossypium Hirsutum L.*): Physiological and morphological responses to water deficits and their relationship to yield. *Field Crops Research* 14, 153-170.

Vellidis G., Liakos, V., Porter, W., Tucker, M., Liang, X. (2016). A dynamic variable rate irrigation control system. 13th International Conference on Precision Agriculture. St. Louis, Missouri.

Vellidis, G., Tucker, M., Perry, C., Reckford, D., Butts, C., Henry, H., Liakos, V., Hill, R.W., & Edwards, W. (2013). A soil moisture sensor-based variable rate irrigation scheduling system. In: J.V. Stafford (Ed.), Precision Agriculture 2013 – Proceedings of the 9th European Conference on Precision Agriculture (9ECPA), Lleida, Spain, pp.713-720.

Wang, L. and Qu, J.J. (2007). NMDI: A normalized multi-band drought index for monitoring soil and vegetation moisture with satellite remote sensing. *Geophysical Research Letters* vol. 24, L20405.

Wanjura D.F., Upchurch, D.R., Mahan, J.R., and Burke, J.J. (2002). Cotton yield and applied water relationships under drip irrigation. *Agricultural Water Management* 55(3):217-237.

Wells R. and Stewart A.M. (2010). Morphological Alterations in Response to Management and Environment. In: Stewart J.M., Oosterhuis D.M., Heitholt J.J., Mauney J.R. (eds) Physiology of Cotton. Springer, Dordrecht.

Wrona, A.F., Krieg, D.R., Baker, D., Bednarz, C., and Hutmacher, R. (1999). Cotton water use. National Cotton Council Cotton Physiology Today, vol. 10, n.2.

TABLES AND FIGURES

Table 3.1. Sampling dates and number of physiological parameter measurements made per date.

Sampling Date	DAP	Canopy Status	Number of Measurements per Sampling Date			
			LWP_{PD}	Plant Height	A_n	g_s
2019						
30 Jul	60	BCC	31	31	18	18
07 Aug	68	BCC	31	31	18	18
16 Aug	77	BCC	31	31	18	18
21 Aug	82	BCC	31	31	18	18
28 Aug	89	BCC	31	31	18	18
05 Sept	99	ACC	31	31	18	18
11 Sept	103	ACC	31	31	18	18
19 Sept	111	ACC	31	31	18	18
27 Sept	119	ACC	31	31	18	18
2020						
15 Jul	43	BCC	37	37	15	15
22 Jul	50	BCC	37	37	15	15
31 Jul	59	BCC	37	36	0	0
05 Aug	64	BCC	37	37	15	15
12 Aug	71	BCC	37	37	15	15
26 Aug	85	BCC	37	37	15	15
02 Sept	92	ACC	37	37	15	15
09 Sept	99	ACC	37	37	15	15
23 Sept	113	ACC	37	36	15	15
30 Sept	120	ACC	37	37	15	15

Table 3.2. Vegetation indices calculated from UAV, PlanetScope and Sentinel-2 images.

VI	Formula	Reference
	UAV, PlanetScope and Sentinel-2	
CIgreen	(NIR / Green) -1	Gitelson et al. (2003)
GNDVI	(NIR – Green) / (NIR + Green)	Gitelson et al. (1996)
GRVI	(Green - Red) / (Green + Red)	Tucker (1979)
NDVI	(NIR – Red) / (NIR + Red)	Rouse et al. (1974)
OSAVI	(1 + 0.16) (NIR – Red) / (NIR + Red +0.16)	Rondeaux et al. (1996)
NLI	(NIR^2 – Red) / (NIR^2 + Red)	Goel and Qin (1994)
	PlanetScope and Sentinel-2	
GBNI	(Green – Blue) / (Green + Blue)	Beeri et al. (2018)
	Sentinel-2	
NDWI	(NIR – SWIR 11)/(NIR+SWIR 11)	Gao et al.(1996)
NMDI	NIR – (SWIR 11 - SWIR 12) / NIR + (SWIR 11 - SWIR 12)	Wang and Qu (2007)

Table 3.3. Pearson (p<.0001) correlation between plant height and VIs developed from UAV imagery.

----- 2019-----										
VI	DAP									
	60	68	77	82	89	99	103	-	119	Overall
CIgreen	0.85	0.80	0.72	0.62	0.55	0.59	0.39	-	0.64	0.72
GNDVI	0.86	0.80	0.72	0.62	0.53	0.62	0.43	-	0.65	0.72
GRVI	0.79	0.80	0.83	0.77	0.65	0.73	0.59	-	0.78	0.51
NDVI	0.87	0.82	0.81	0.73	0.60	0.70	0.49	-	0.72	0.70
OSAVI	0.87	0.82	0.78	0.71	0.67	0.72	0.44	-	0.71	0.61
NLI	0.87	0.82	0.79	0.72	0.66	0.73	0.46	-	0.71	0.61
----- 2020 -----										
VI	DAP									
	43	50	64	71	85	92	-	113	120	Overall
CIgreen	0.59	0.65	0.72	0.74	0.57	0.49	-	0.73	0.79	0.82
GNDVI	0.60	0.66	0.75	0.76	0.61	0.56	-	0.74	0.65	0.84
GRVI	0.44	0.45	0.78	0.79	0.36	0.71	-	0.55	0.71	0.70
NDVI	0.71	0.60	0.80	0.75	0.58	0.58	-	0.68	0.65	0.80
OSAVI	0.70	0.64	0.76	0.78	0.50	0.53	-	0.63	0.66	0.77
NLI	0.67	0.64	0.79	0.79	0.55	0.59	-	0.66	0.72	0.80

Table 3.4. Pearson correlation (p<.0001) between UAV and satellite-based VIs and predawn LWP_{PD}.

VI	--UAV--		--PlanetScope--		--Sentinel-2--	
	2019	**2020**	**2019**	**2020**	**2019**	**2020**
CIgreen	-0.26	-0.24	-0.37	-0.46	-0.63	-0.07^{ns}
GNDVI	-0.30	-0.24	-0.40	-0.37	-0.61	-0.12^{ns}
GRVI	0.11^{ns}	-0.30	-0.29	-0.45	-0.38	-0.21
NDVI	-0.19	-0.25	-0.40	-0.41	-0.55	-0.15
OSAVI	0.02^{ns}	-0.28	-0.37	-0.49	-0.52	-0.23
NLI	-0.01^{ns}	-0.28	-0.37	-0.46	-0.52	-0.20
GBNI	-	-	0.26	-0.56	0.37	0.42
NDWI	-	-	-	-	-0.49	-0.22
NMDI	-	-	-	-	-0.47	-0.25

^{ns} not significant

Table 3.5. Irrigation amounts, final cotton yield and irrigation water use efficiency for VRI and conventional irrigation treatment in 2019 and 2020.

Irrigation	**2019**				**2020**			
	Yield (kg ha^{-1})	Irrigation (mm)	IWUE (kg/mm)	Irrigation events	Yield (kg ha^{-1})	Irrigation (mm)	IWUE (kg/mm)	Irrigation events
VRI	1,794	86.5	20.74	7	1,248	50.8	24.57	4
Conventional	1,890	87.2	21.67		1,191	58.4	20.39	

Table 3.6. Irrigation management zones (IMZs) average plant height and yield. IMZs are listed in order of lowest to highest for both variables.

Zones	Height (cm)	Zones	Yield (kg/ha)
25	82.9	9	869.0
7	85.6	25	873.0
9	85.7	15	956.9
14	87.5	7	1041.0
4	88.1	14	1068.5
1	88.4	16	1106.2
24	88.7	1	1131.9
19	89.1	24	1160.2
28	90.2	5	1192.4
15	90.2	4	1200.6
23	91.0	29	1208.5
27	91.1	27	1213.3
16	91.4	28	1221.7
17	91.7	2	1256.1
29	91.8	13	1280.5
22	91.8	17	1325.5
21	92.0	21	1332.2
20	92.0	20	1333.6
26	92.2	6	1355.3
5	92.2	11	1360.3
8	92.4	3	1360.7
13	92.6	8	1372.2
18	92.7	10	1381.9
2	93.4	18	1382.4
12	93.6	12	1403.6
11	94.0	26	1408.9
3	94.5	19	1417.3
6	95.2	22	1452.1
10	95.7	23	1521.5

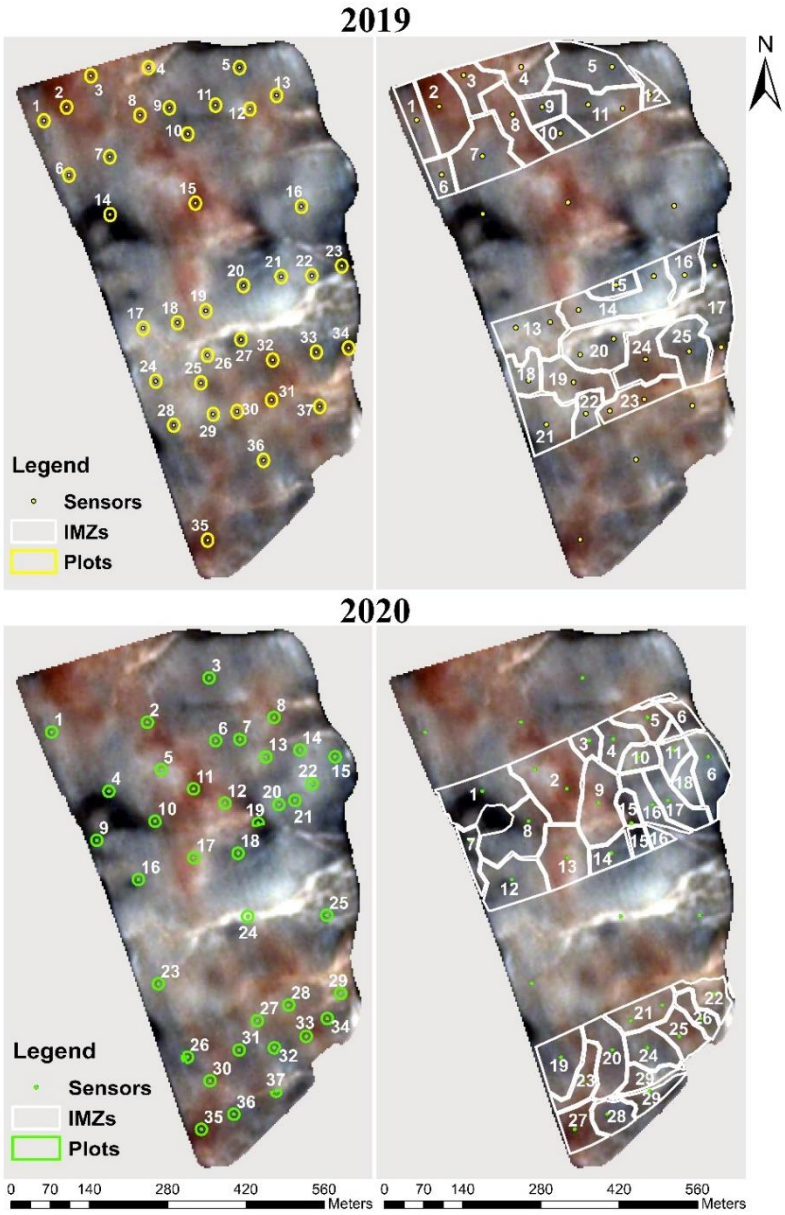

Figure 3.1. Field location and conventional and VRI strips layout in 2019 and 2020. Location of soil moisture sensors, IMZs delineated and 10 m radius circle plots around sensor location. In 2019 and 2020, IMZ maps shown are the initial IMZ developed. Second IMZ map created in 2020 is shown in the results section.

Figure 3.2. Field installation of UGA Soil Sensor Array (SSA) node.

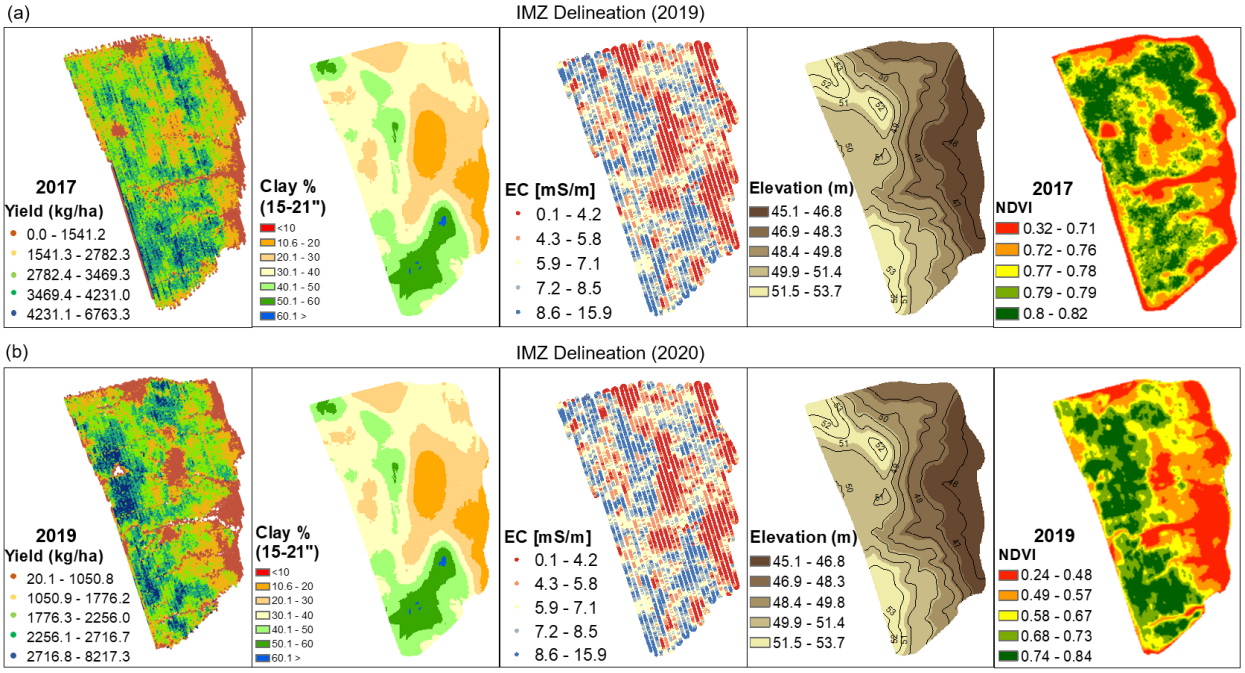

Figure 3.3. Data layers used for IMZ delineation in (a) 2019 and (b) 2020.

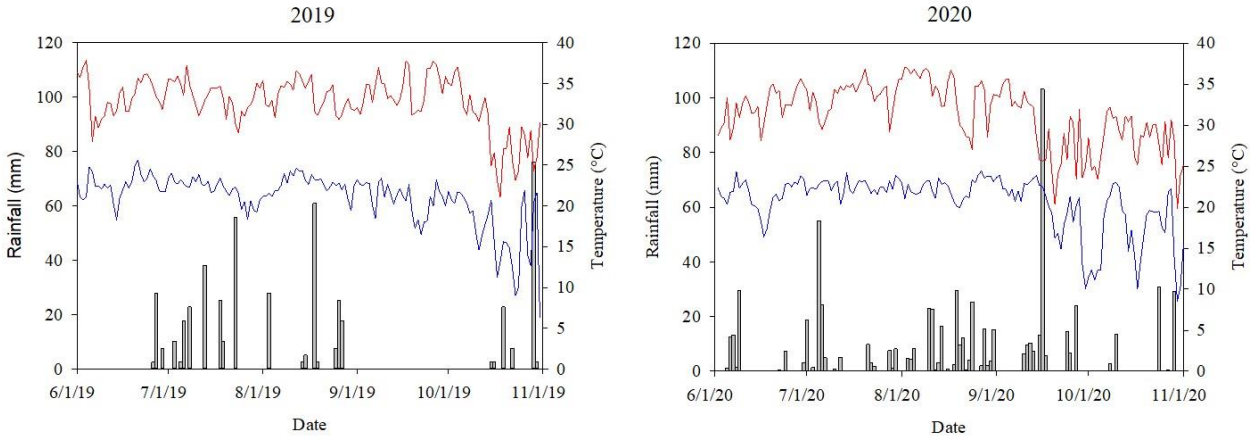

Figure 3.4. Weather conditions in the field during the growing seasons. Precipitation data and minimum and maximum temperature from (a) 2019 and (b) 2020.

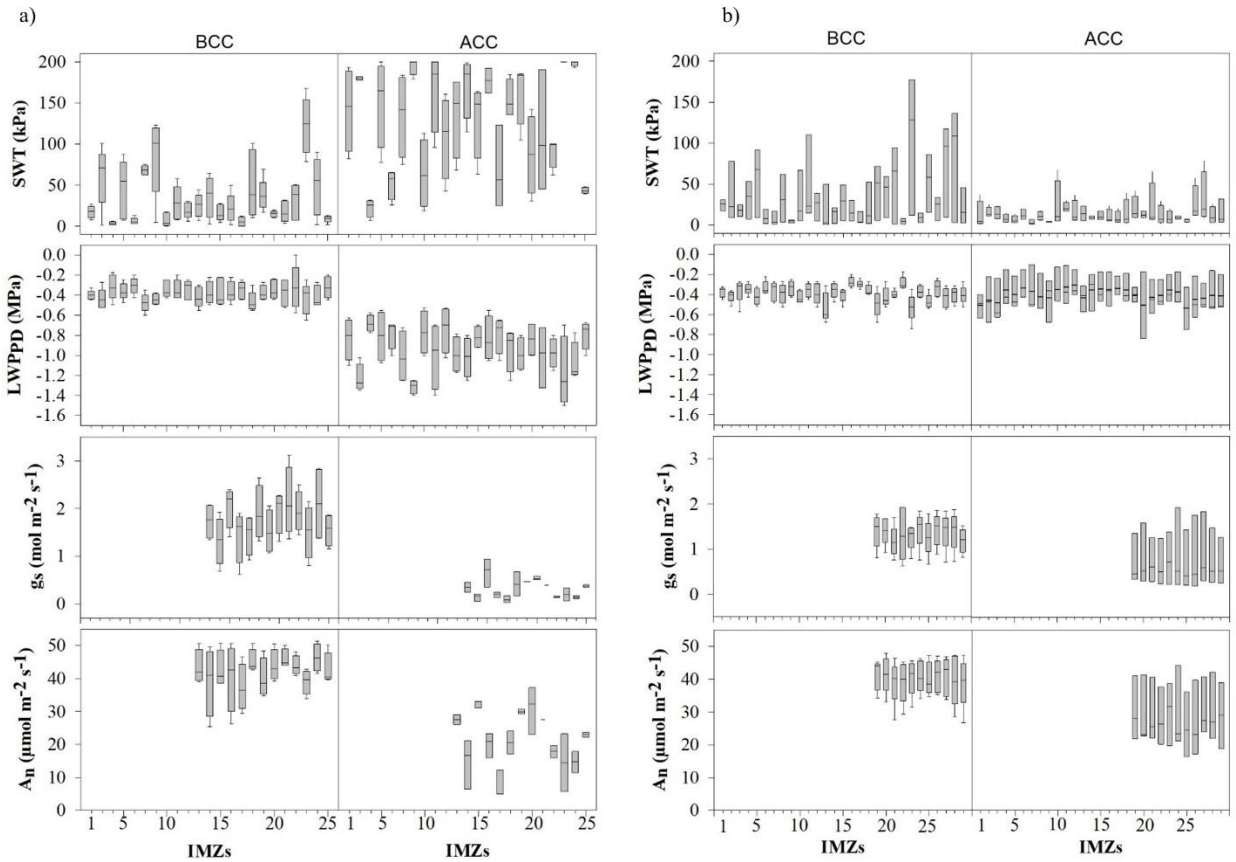

Figure 3.5. SWT and physiological parameters distribution in two different stages (BCC and ACC) among the IMZs delineated in (a) 2019, and (b) 2020. In 2020, data at the ACC stage refers to IMZ map 2, when IMZ boundaries was adjusted based on predicted crop height map.

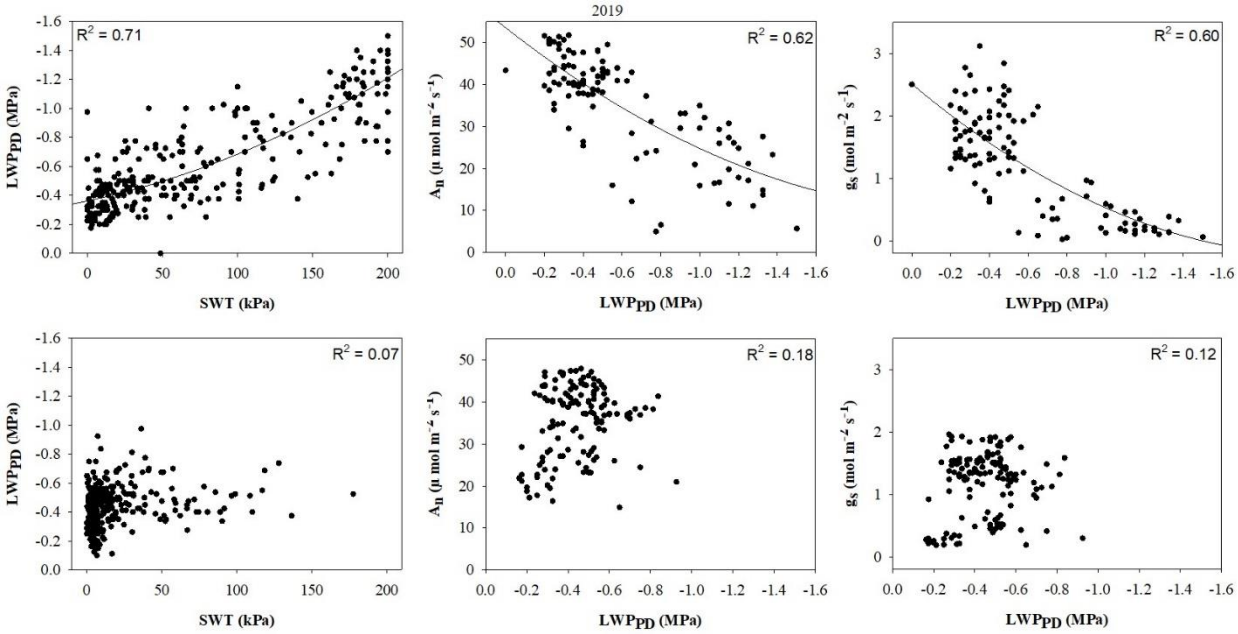

Figure 3.6. Relationship between plot SWT, and LWP_{PD} (2019; *n* = 279, 2020; *n* = 370), LWP_{PD} (2019; *n* = 162, 2020; *n* = 135) and A_n, and LWP_{PD} and g_s (2019; *n* = 162, 2020; *n* = 135) for cotton grown in (a) 2019 and (b) 2020.

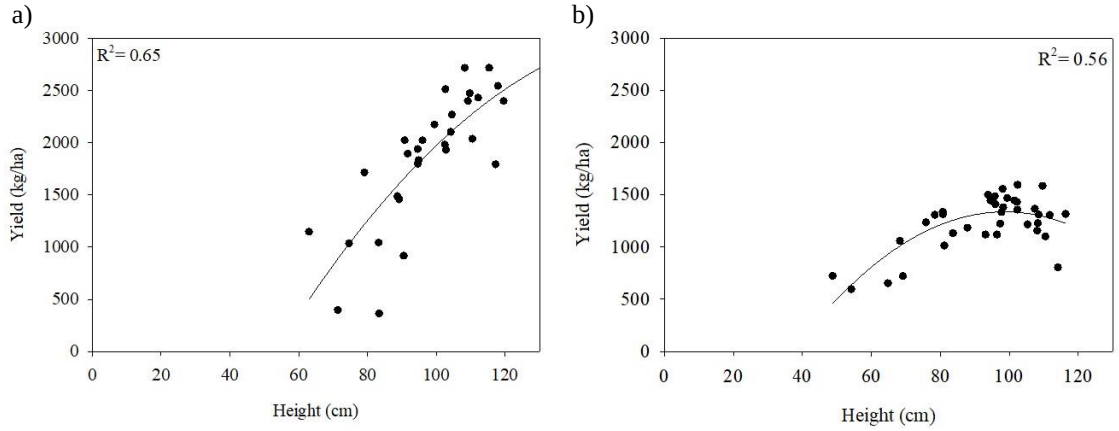

Figure 3.7. Relationship between plant height plot averages and end of the season yield for a) 2019 and b) 2020.

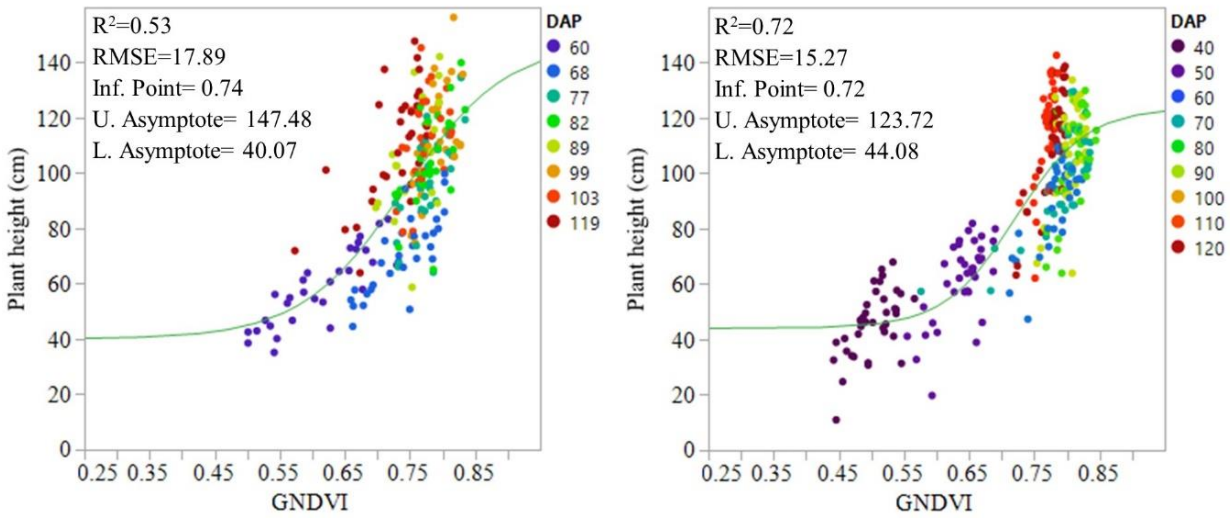

Figure 3.8. Logistic (sigmoid) curve of plant height response to GNDVI in 2019 and 2020. Plant height plot measurements and GNDVI plot averages were used to build model (2019; *n* =229, 2020;*n* = 290).

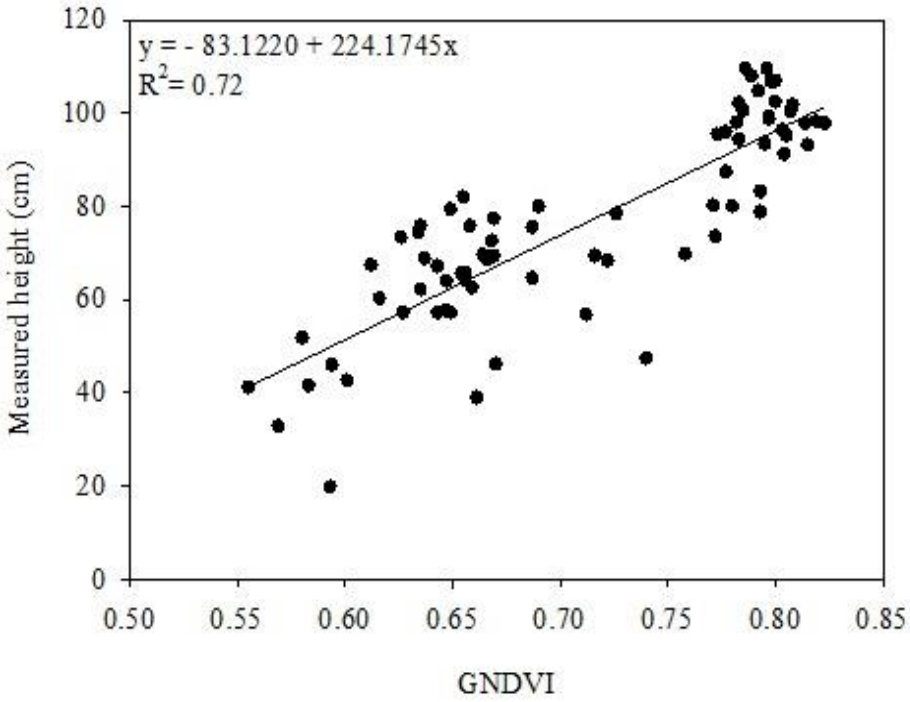

Figure 3.9. Development of predicted plant height using linear regression model between GDNVI and measured plant height.

a) b)

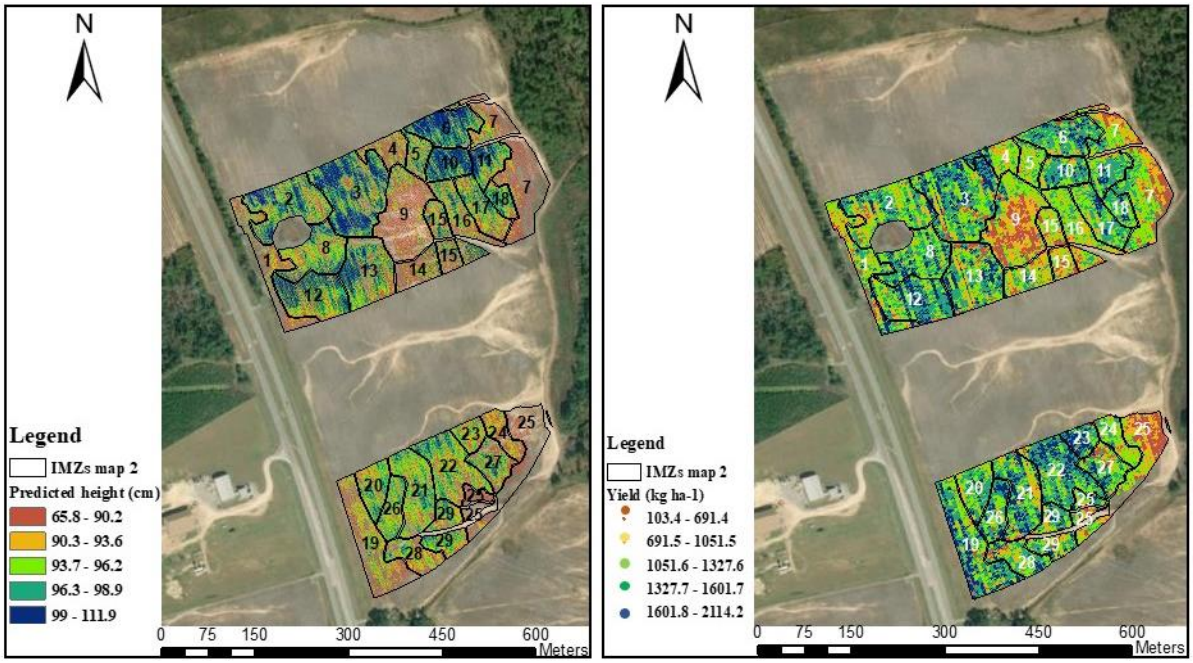

Figure 3.10. Second IMZ map delineated based on b) predicted height and IMZs boundaries over c) final cotton yield map. Quantile classification method was used in both maps.

CHAPTER 4

FIELD SCALE ASSESSMENT OF THE TsHARP TECHNIQUE FOR THERMAL SHARPENING OF MODIS SATELLITE IMAGES USING VENμS AND SENTINEL-2 DERIVED NDVI[3]

[3] Lacerda, L., Cohen, Y., Snider, J., Huryna, H., Liakos, V., and Vellidis, G. To be submitted to *Remote Sensing MDPI*.

Abstract

Remotely sensed-based surface temperature is an important tool for crop monitoring and has great potential for improving irrigation management. However, current thermal satellite platforms do not display the fine spatial resolution required for identifying crop water status patterns at the field scale. The thermal sharpening (TsHARP) utility provides a technique for downscaling coarse thermal images to match the finer resolution of images acquired in the visible and near infrared bandwidths. This sharpening method is based on the inverse linear relationship between vegetation fraction calculated from the normalized difference vegetation index (NDVI) and land surface temperature (LST). The current study used the TsHARP method to sharpen low-resolution thermal data from the Moderate Resolution Imaging Spectrometer MODIS (1 km) to the finer resolution of Sentinel-2 (10 m) and Vegetation and Environment New micro-Spacecraft (VENμS) (5 m) visible-near infrared images. The sharpening methodology was evaluated at scene and field scales in southern Georgia and northern Mississippi, USA. A comparison of sharpened temperature was made with reference temperatures from Landsat-8 Operational Land Imager (OLI) in four different spatial resolutions (30, 60, 120, and 240 m) for method validation. Coarse resolution comparison on the dates in which imagery from both sensors were acquired on the same day resulted in average observed mean absolute error (MAE) of 1.63 °C, and R^2 variation from 0.34 to 0.74. Temperature errors at the field scale ranged from 0.25 to 3.11 °C using both Sentinel-2 and VENμS. Sharpened maps at 120 and 60 m resolution showed the highest consistency for all fields and dates. Maps sharpened using VENμS images showed comparable or higher accuracy than maps sharpened using Sentinel-2. The superior performance coupled with the better revisit time indicates that the VENμS platform has high potential for frequent in-season crop monitoring. Further research

with ground data collection is needed to explore field use limitations of this methodology, but these results give useful insights of potential benefits of implementing the TsHARP technique as a tool for crop stress monitoring.

4.1. Introduction

Thermal remote sensing uses thermal infrared (TIR) bands in the 8 to 14 μm region of the electromagnetic spectrum in which atmospheric absorption effects are attenuated (Ishimwe et al. 2014). At the molecular level, plant absorption in the TIR bands is influenced by the absorption properties of leaf tissues driven by molecular vibration (Ribeiro da Luz et al. 2006). At the physiological level, absorption is directly influenced by the transpiration rate (Hsiao 1973). In drought conditions, plants that exhibit isohydric behavior tend to close their stomata to maintain leaf water potential (LWP). This decreases their transpiration rate significantly, leading to an increase in leaf temperature (Bodner et al. 2015). The direct relationship between changes in leaf temperature resulting from changes in LWP makes TIR bands more sensitive to detecting water stress than other regions of the electromagnetic spectrum. Because of this, thermal imagery has become increasingly important in monitoring of water status for irrigation management (Falkenberg et al. 2007) in crops such as coffee (Costa et al. 2020), cereals (Panigada et al 2014), Elsayed et al. 2017), and soybean and cotton (O'Shaughnessy et al. 2011).

Thermal infrared temperature maps can be used to estimate LWP and create LWP maps at the field scale. In turn, the LWP maps may be used to delineate LWP-based irrigation management zones (IMZs) for site-specific irrigation (Cohen et al. 2017b). The spatial resolution of currently available satellite-based thermal imagery is not fine enough to identify crop water status patterns at the field scale. Satellite platforms such as Terra MODIS (Moderate Resolution Imaging Spectroradiometer) and NOAA-AVHRR (National Oceanic and Atmospheric

Administration–Advanced Very High-Resolution Radiometer) have a very high temporal resolution (1 day), but a coarse spatial resolution of 1 km (Agam et al. 2007b). Conversely, Landsat Thematic Mapper—TM, Landsat Enhanced Thematic Mapper Plus—ETM^{+}, and Landsat Operational Land Imager—OLI, have higher spatial resolution of 120, 60, and 100 m respectively, but a low revisit time of 16 days. While Landsat datasets have a finer resolution, its low temporal resolution is not adequate for frequent monitoring required during the growing season for irrigation decisions. The occurrence of clouds can further decrease the availability of usable images.

To address this tradeoff problem between low-resolution images with high revisit time and high-resolution images with low revisit time, sharpening methodologies to downscale TIR coarse resolution have been proposed (Cohen et al. 2017a). These techniques to disaggregate land surface temperature (LST) are found in the literature under a variety of terms, such as thermal sharpening, subpixel temperature estimation, downscaling LST, component temperature retrieval, spatial enhancement of LST, and others (Zhan et al., 2013), but they can be classified into two main categories, called temperature unmixing and thermal sharpening. The main difference between these two groups is that in temperature unmixing, the goal is to decompose the coarse mixed pixel temperature into its existing elements through temporal, spatial, and spectral observations, while thermal sharpening aims to enhance the thermal image by exploring the correlation between LST and auxiliary data such as vegetation cover (Bisquert et al. 2016).

Thermal sharpening is the category most frequently used for downscaling thermal images. One of the earliest works using spatial sharpening dates back to 1985, wherein Landsat-4 Thematic Mapper (TM) thermal imagery was sharpened to 30 m resolution using a multiband least squares method (Tom et al. 1985). This approach was possible due to the high correlation

between the TM bands in agricultural scenes. A thermal image estimate was created using a coefficient predicted from Landsat-4 TM visible and infrared bands that was then used to enhance the spatial resolution on the original thermal band.

Over the last 30 years, a variety of new sharpening algorithms have been suggested including the thermal sharpening (TsHARP) technique that was improved from the Disaggregation procedure for radiometric surface temperature (DisTrad) algorithm developed by Kustas et al. (2003). The DisTrad method uses the relationship between radiometric surface temperature and the Normalized Difference Vegetation Index (NDVI) to disaggregate temperature data at the NDVI finer image resolution. The NDVI resolution is first aggregated to the coarser resolution of the brightness temperature (BT) image and a second degree polynomial least-squares regression is fitted between the two variables. In this study, airborne images were used to estimate temperatures over the southern Great Plains by sharpening MODIS images to 200 m and provided temperature errors of ~1.5 °C. Agam et al. (2007b) proposed an improvement from the DisTrad algorithm by using vegetation fraction as the dependent variable instead of NDVI. Different types of land cover in a scene can cause increased number of outliers in the two ends of NDVI values.

A summary study published in 2013 (Zhan et al. 2013) indicated that Landsat TM and Terra Advanced Spaceborne Thermal Emission and Reflection Radiometer (ASTER) were the satellite platforms most frequently used for LST disaggregation. At the time, MODIS was a much younger platform, and since then has become widely utilized in downscaling approaches due to the high temporal frequency in which images are made available. With MODIS images collected on a daily basis, the availability of datasets for sharpening during the growing season depends on the satellite platforms used to derive visual and NIR (VNIR) data. Landsat 7 ETM^{+}

(Bisquert et al. 2016, Bindhu et al. 2013) and Landsat-8 OLI (Wang et al. 2020)] are commonly used to build the LST-NDVI regression and can generate roughly two sharpened images. Sentinel-2 has a higher revisit time and offers the potential of more sharpened images during the season. Clouds may greatly reduce the availability of useable images, especially in areas with frequent cloud cover.

Sentinel-2 is a two-satellite platform operated by the European Space Agency (ESA) as part of the Copernicus earth observation program which became operational (Huryna et al. 2019) in 2015. The two satellites are in the same orbit but spaced 180° apart. They provide data in 13 different spectral bands (443–2190 nm) with spatial resolutions of 10, 30, and 60 m and a revisit time of 5 days. Sanchez et al. (2020) used Sentinel-2 VNIR data to sharpen MODIS images to a 10 m resolution over experimental fields in southeastern Spain. Over a period of 2 months, they sharpened LST images on 6 different days.

In 2017, a super-spectral micro-satellite resulting from a partnership between the Israel Space Agency (ISA) and the French National Centre for Space Studies (CNES) was launched (Ferrier et al. 2010, VENµS, 2020). The Vegetation and Environment New micro-Spacecraft (VENµS) was intended to increase land data acquisition to, among other purposes, improve modeling of vegetation processes. This minisatellite has a revisit time of 2 days, a spatial resolution of 5.3 m, and a spectral resolution of 12 bands (420–910 nm). Although the unique features of this low-orbit satellite show great potential for increased dataset frequency, to our knowledge, no studies have explored the use of VENµS in thermal sharpening methodologies.

The majority of sharpening studies cited above explored the use of sharpening for large scene scales. However, very few studies have been conducted exploring the feasibility of using this technique in crop fields to aid in management decisions. In this context, the main goal of this

work was to assess the use of the TsHARP technique to sharpen MODIS images using Sentinel-2 and VENμS in the southeastern USA at field scale and to assess if sharpened images have the potential to be used at the field scale for delineating irrigation management zones (IMZs) for variable rate irrigation in cotton. Applying this technique to this region is especially challenging because of frequent cloud cover during the growing season. The TsHARP use at scene scale was also assessed. Specific objectives were to compare the performance of the TsHARP technique using data from the two satellite platforms on overlapping dates.

4.2. Materials and Methods

4.2.1. Study Sites

This study was conducted in three different locations of the southeastern USA in which cotton is an important crop (Figure 4.1) using imagery from the 2019 growing season. The first and second study sites are located in southwestern Georgia and centered around 84°44′28 W, 31°11′28″ N, and 84°33′7″ W, 31°26′42″ N. The third study site is located in northeastern Mississippi centered around 88°51′42″ W, 34°31′58″ N. The Miller County scene (hereafter referred as to scene 1) is mostly composed of cotton fields, followed by woody wetlands, pine forest, and peanut fields. Land cover in scene 2, located in Baker County, Georgia, was 40% woody wetlands followed by pine forest, and cotton and peanut fields. The land cover in scene 3, located around Union County, Mississippi, was composed mostly of various types of forest, followed by pasture and soybean fields. All locations have similar subtropical climates with high humidity and hot summers, with the average air temperature of the hottest month (July) being equal to or greater than 22 °C (Kottek et al. 2006, Beck et al. 2018). The minimum and maximum average temperatures from July to November in the last 20 years were 15.6 and 27.4°C (NOAA, 2020).

The United States Department of Agriculture (USDA) National Agricultural Statistics Service's (NASS) Cropland Data Layer (CDL) hosted by CropScape (https://nassgeodata.gmu.edu/CropScape/ (accessed on July 9th, 2020)) was used to identify fields that were planted with cotton during the 2019 growing season. Extensive agricultural ground truth data acquired from the Common Land Unit (CLU) data from the USDA Farm Services Agency (FSA) is coupled with moderate resolution satellite images to create yearly crop-specific land cover maps of the whole continental United States (Boryan et al. 2011). A total of 22 cotton fields were identified for this study, with field sizes ranging from 14 ha to 164 ha (Table 4.1).

4.2.2. Satellite images acquisition and processing

Thermal images from MODIS and Landsat-8 Operational Land Imager (OLI) were acquired in all three locations on dates within the cotton growing period ranging from August to November 2019 (Table 4.2). The MODIS product used was MODIS/Thermal Bands Daily L2B-Lite Global (MODTBGA), and it was download from the National Aeronautics and Space Administration (NASA) Earth Data Search website (https://search.earthdata.nasa.gov/search (accessed on April 15th, 2020)). MODTBGA version 6 is available daily with a spatial resolution of 1 km (km) with sinusoidal projection, and it consists of brightness temperature data from three MODIS bands (bands 20, 31, and 32) (USGS, 2020). After download, MODIS images were pre-processed using ArcGIS (Esri, Redlands, CA, USA). In ArcMap version 10.2.2 (Esri, Redlands, CA, USA), MODIS band 31 was re-projected to the World Geodetic System (WGS) 1984 zone 16, and a scale factor of 0.01 was used to obtain brightness temperature values. Landsat-8 OLI images were downloaded directly from the United States Geological Survey (USGS) Earth Explorer website (https://earthexplorer.usgs.gov/ (accessed on April 20th, 2020)). Landsat-8

provides images with 15 (panchromatic), 30, and 100 m (thermal) spatial resolution. However, thermal bands are disaggregated to 30 m resolution images by the Landsat Science team and are made publicly available. Landsat-8 pre-processing was performed by using the Semi-Automatic Classification Plugin (SCP) in QGIS 3.14.0 (QGIS Development Team, 2020) (QGIS, 2020). SCP offers pre-processing and post-processing tools for a variety of satellite images (Leroux et al. 2018). Radiometric calibration was performed on Landsat-8 thermal infrared band 10 (10.6–11.19 μm), where the DOS1 (Dark Object Subtraction) atmospheric correction technique was used to convert data to Top of Atmosphere (TOA), and correct for solar irradiance effects. SCP was also used to convert values to brightness temperature in Celsius.

Visual-near infrared (VNIR) data from Sentinel-2 was used for sharpening in all three locations. Images were downloaded from the USGS Earth Explorer website. SCP was used to perform atmospheric correction in all Sentinel-2A images. The SCP used DOS1 atmospheric correction for Sentinel-2 images as well. Band 8 (842 nm) and band 4 (665 nm) were used to calculate NDVI. VNIR images from VENμS were also utilized for thermal sharpening of MODIS. VENμS data were only available for the scenes in Georgia (Miller and Baker counties). Images were download from the Theia Data and Services Center for continental surfaces (https://www.theia-land.fr/en/data-and-services-for-the-land/ (accessed on April 20th, 2020)). VENμS-based NDVI was calculated using bands 11 (865 nm) and 5 (620 nm) from the level 2 product. VENμS level 2 product provides fine cloud and shadow mask, and it is already atmospherically corrected.

Due to the differences in satellite temporal resolution, and frequent cloud coverage during the summer in the study areas, the difference in acquisition date among the satellites used

for TsHARP implementation (MODIS, Sentinel-2, and VENμS) was up to one day and up to five days for validation (MODIS and Landsat-8).

4.2.3. TsHARP methodology

As described previously, the TsHARP technique is based on the inverse relationship between LST and vegetation cover. The fractional vegetation cover (*f*c) is estimated from NDVI using Equation (1) (Choudhury et al. 1994)

$$fc = 1 - \left(\frac{\mathrm{NDVI_{max}} - \mathrm{NDVI}}{\mathrm{NDVI_{max}} - NDVI_{min}}\right)^{0.625} \quad (1)$$

where $\mathrm{NDVI_{max}}$ and $\mathrm{NDVI_{min}}$ are the maximum and minimum NDVI values in the scene and NDVI is the index value in an individual pixel.

The *f*c image is aggregated to a coarser resolution to match with the coarse resolution of the LST image, and an empirical linear regression model is fitted as shown by Equation(2).

$$LST_{coarse} = \mathrm{a} + \mathrm{b}fc_{coarse} \quad (2)$$

where a and b are the intercept and slope resulting from the linear regression between LST and fc at coarse resolution.

Coefficients a and b are then applied to the fine resolution *f*c data (fc_{fine}) and fine resolution NDVI to predict LST at a finer resolution (Equation (3)) (Huryna et al. 2019). Coefficients a and b are also applied to the *f*c image at coarse resolution to derive a new LST image. The difference between the original LST image and the newly derived image is used to calculate the residual error image at coarse resolution. The residual error image is then disaggregated to a fine resolution and applied to the LST at finer resolution to increase the prediction accuracy (Equation (4)). A detailed explanation of the TsHARP algorithm was provided by Agam et al. (2007b).

$$LST_{fine} = \mathrm{a} + \mathrm{b}fc_{fine} \quad (3)$$

$$LST_{predicted} = LST_{fine} + residual\ error \quad (4)$$

4.2.4. TsHARP validation and assessment

The complete workflow of the TsHARP technique can be divided into two steps (Figure 4.3). The first step is the sharpening of MODIS images using Sentinel-2- and VENµS-derived NDVI to finer resolutions. The second step is the validation of the method by comparing the sharpened temperature with a reference temperature from Landsat-8 images at 30, 60, 120, and 240 m spatial resolution. The TsHARP validation was performed by fitting a linear regression model to MODIS BT and Landsat-8 BT images in the coarse and finer resolutions. The validation was performed at the scene scale for all dates for which images were downloaded and for selected dates at the field scale (See Table 4.2).

The methodology performance assessment was estimated using different quantitative statistics approaches (Willmott et al. 1982). Coefficient of determination (R^2), root mean square error (RMSE), mean absolute error (MAE) and bias (Equations (5)-(8)) were calculated to estimate the level of agreement between predicted and reference temperatures.

$$R^2 = 1 - \frac{\sum\left(T_{sharp} - T_{ref}\right)^2}{\sum\left(T_{sharp} - T_{ref\_mean}\right)^2} \quad (5)$$

$$RMSE = \left[n^{-1}\sum_{i=1}^{n}\left(T_{sharp} - T_{ref}\right)^2\right]^{1/2} \quad (6)$$

$$MAE = \left[n^{-1}\sum_{i=1}^{n}\left(T_{sharp} - T_{ref}\right)\right] \quad (7)$$

$$bias = \frac{\sum_i^n 1(T_{sharp} - T_{ref})}{n} \quad (8)$$

4.3. Results and Discussion

4.3.1. Scene Scale

The thermal sharpening validation was performed for a total of 14 dates using the MODIS/Sentinel-2 and MODIS/VENµS BT-NDVI regressions (Table 4.2).

4.3.1.1. Sensors Comparison at Coarse Resolution

The correlations between MODIS brightness temperature (BT) and aggregated Landsat-8 BT at coarse resolution are shown in Figure 4.4. Results showed that the correlations between the BT of the two sensors were similar towards the end of the season (end of October and beginning of November) when average temperatures were in the low 20 °C or below, with coefficients of determination (R^2) ranging from 0.68 in scene 1 to 0.74 in scene 3. The regression model coefficients, however, were different. Despite having the highest R^2 among the three scenes, the sensor comparison of scene 3 presented the highest RMS error and positive bias of 3.54 °C. In scenes 1 and 2, the RMS errors in this period were below 1.25 °C, with a negative bias lower than 0.95.

In the months of August and September, correlations were overall lower, and varied with location. The lowest R^2 values were observed in scene 1 (0.31) followed by the third date in scene 3 (0.41) and first date in scene 2 (0.44). The low relationship in these three dates can be attributed to cloud coverage in one or more images. Parts of the respective scenes were cropped to exclude areas affected by the clouds, substantially decreasing the number of pixels. In addition, methods utilized to mask clouds were not effective in removing areas under the clouds' shadow. The combination of reduced number of pixels and BT values affected by cloud shadow led to a weaker relationship between sensor responses.

A negative bias was observed in 7 out of 9 dates and indicates that temperatures extracted from MODIS scene were cooler when compared to Landsat-8. The comparison between these two sensors yielded RMS errors no higher than 1.92 °C in 6 out of 9 dates. In the second date of scene 2, and the first and last dates in scene 3, the RMSE values observed were higher, with errors ranging from 2.75 to 3.45 °C. In 2 out of these 3 dates, the bias was positive and not negative like in most of the dates. No clear factors were found that can explain these deviations.

Similar results were observed in the selected dates for VENµS analysis (Figure 4.5). As mentioned earlier, VENµS images were only available for the two scenes in Georgia. The relationship between MODIS BT and Landsat BT was strong at the end of October when temperatures were lower, and weaker in the months of August and September. In the remaining dates, R^2 values in scene 2 were again stronger than the ones observed in scene 1. The RMS errors varied between 1.03 to 2.14 °C in both locations. Similar to MODIS/Sentinel-2 sharpening, a negative bias was observed for 3 out of 5 dates, while a positive bias was obtained for the other 2 dates.

A study conducted in 2014 (Weng et al. 2014) reported differences between MODIS and Landsat satellite LST spatial distribution. Maximum temperatures showed a difference of about 15 °C. The range between minimum and maximum temperatures from Landsat were always wider than observed in MODIS (Table 4.3). In the study described here, towards the end of October, most of the crops were already harvested and fields had exposed soil, causing a more evident BT difference between dense vegetation and exposed soil, which could be more easily detected by the coarse spatial resolution from MODIS. During the months of August, September, and mid-October, most fields in the scenes still had vegetation cover from the crops, thus temperature changes were more subtle across different land covers. These subtle changes were

depicted in the finer resolution from Landsat, leading to a wider range of temperature values compared to the smaller range from MODIS, resulting in a lower R^2.

Coarse resolution sensor comparison showed that the BT range values of Landsat were always wider than observed in MODIS (Table 4.3). At one date (8/29), the Landsat BT range was double the MODIS BT and the max difference was as high as 6.4 °C. Similar results were observed by Weng et al. (2014) when comparing Landsat TM LST to MODIS. In the two dates used in their study, similarities were observed only between minimum surface temperatures. Landsat TM maximum temperatures were considerably higher than in MODIS, causing great discrepancies in LST spatial patterns. Essa et al. (2017) stated that surface temperature from MODIS were substantially lower than Landsat 7 ETM^+ temperatures. A 5 °C mean temperature difference between the two sensors was achieved on six occasions. The results from 10 out of 14 dates examined in this paper showed a similar trend, where a negative bias was found between the two sensors. This consistently lower temperature presented by MODIS when comparing with Landsat sensors can be described as a systematic bias. Yet, the fact that some occasions showed different trends casts a shadow over this determination. The concept of systematic bias was discussed by Liu et al. (2006). A consistent bias between two satellites could be introduced by sensor measurement errors such as random noise. Satellite sensor-specific characteristics such as bandwidth, acquisition time, and orbit parameters are further causes of bias (Weng et al. 2014).

4.3.1.2. TsHARP validation

Landsat-8 thermal images were aggregated to 60, 120, and 240 m to perform validation at the four spatial resolutions proposed, including Landsat's original resolution of 30 m. Tables 4.4 and 4.5 show the statistics of sharpened images compared to reference maps in all the scenes studied using both VENμS- and Sentinel-2-based NDVI, respectively. Validation of thermal

sharpening resulted in an overall higher R^2 than only comparing sensor brightness temperatures at coarse resolution. Sharpened accuracy was higher in coarser resolutions (120 and 240 m) in 10 of the 14 dates analyzed. In most remaining dates in which accuracy at 240 m was slightly lower than finer resolutions, portions of the scene had to be excluded prior to the analysis due to cloud cover. The decrease in the number of pixels in the 240 m resolution could have affected the sharpening accuracy. Based on the results, sharpening efficiency tended to decrease with increased targeted resolution. These findings are corroborated by results observed by Huryna et al. (2019). In their study, Landsat-8 and Sentinel-3 thermal imagery were resampled and then sharpened to 240, 120, and 60 m resolutions using Landsat-8 and Sentinel-2, respectively. In both cases, R^2 values decreased and temperature uncertainty values increased as resolution increased, with highest error values of 1.17 and 1.45 °C for Landsat and Sentinel-3, respectively.

The coefficient of determination for Sentinel-2 validation dates in scene 1 ranged from 0.55 at 30 m resolution to 0.76 at 240 m, with highest values occurring on 28 October, while for VENµS dates, the lowest value was 0.48 at 30 m, and the highest value was 0.8 at 240 m (Table 4.5). In scene 2, the method's accuracy in dates available tended to be higher than achieved in scene 1 for both Sentinel-2 and VENµS dates, with only three R^2 values below 0.6. Remaining values for Sentinel-2 varied from 0.6 to 0.8 and for VENµS, from 0.63 to 0.79. In this scene (scene 1), the three weakest relationships were observed at the finer resolutions of 30 and 60 m. Scene 3 displayed a similar performance as the two previous scenes, with values ranging from 0.50 to 0.77, except on 3 October, wherein the Landsat-8 image had large areas in the middle of the scene covered by clouds and cloud shadow that were difficult to remove. The remaining affected pixels that were not excluded by the masking process affected the accuracy of validation. A 3 days difference in acquisition time between sharpened and reference images was

observed and could have also been a cause of higher error, although no trend between error magnitude and time lag between satellites was observed.

Validation of sharpened maps had slightly higher RMS errors than the sensors' BT comparison at coarse resolution, with uncertainty increasing as the aimed resolution became finer. The highest errors were observed in the first and third dates of scene 3, with error values around 3.04 and 3.78 °C. It is worth emphasizing that MODIS and Landsat had a 1-day difference in acquisition time when the highest error of almost 4 °C was observed. Lowest overall errors were observed in the last date of scene 2 for both Sentinel-2 and VENµS selected dates, with uncertainty around 1 °C at 240 m spatial resolution. Although MAE values also tended to increase with increased resolution, its response was not the same as RMSE. Images sharpened to 120 and 240 m resulted in MAEs similar or even lower than the mean errors from the temperature comparison at coarse resolution.

Figure 4.6 shows the temperature error (sharpened T (°C) − reference T (°C)) maps at 60 m resolution at the three individual scenes and their respective land cover types. Error maps were created from MODIS/Sentinel-2 from 27 October in scene 1, 28 October in scene 2, and 29 August in scene 3. Error maps were selected from dates in which there was a maximum of 1-day lag between images. In general, the sharpened BT was lower than the reference temperature. This corresponds with the systematic bias found with the sensor comparison in this paper. Scene 3 is composed in its majority by various types of forests with a lower percentage of grassland and small areas of sparse vegetation (crop fields) (Figure 4.6 (g)). The low variability in land cover type in this scene led to a more homogeneous temperature error distribution (Figure 4.6(h)). Brightness temperatures were underestimated across the whole scene, with forest areas presenting the biggest differences in temperature between sharpened and reference maps. The

land cover distribution in scenes 1 and 2 are more varied between dense and sparse vegetation (Figure 4.6 (a),(d)). Differently from scene 3, sharpened temperatures in scenes 1 and 2 were frequently overestimated in woody wetlands and underestimated in cultivated fields with sparse vegetation and/or exposed soil. The higher variability in temperature errors across different land covers resulted in a lower accuracy of sharpening in these two scenes in Georgia when compared to the scene in Mississippi.

Highest errors were observed in areas covered by wetland and bare soil. Huryna et al. (2019) achieved conflicting results when sharpening Sentinel-3 images, with temperatures being underestimated over dense vegetation and overestimated over agricultural fields, with errors of 1.5 to 3 °C in riparian areas. The bias between original MODIS and Landsat-8 images at coarse resolution were similar to errors seen at finer resolution and might help explain the conflicting results between the two studies.

Great variability in the TsHARP performance was observed among the scenes and dates. LST–NDVI relationships were higher in the scenes with more homogenous land cover, resulting in overall higher accuracy. A high-temperature sharpening performance can be achieved when there is a good correlation between LST and vegetation cover (Chen et al. 2014). Nevertheless, the linear relationship expected between LST and vegetation fraction does not always hold, leading to increased sharpening errors. Factors such as albedo and soil moisture can cause great variations in LST in areas with low NDVI (Agam et al. 2007b). The different moisture levels in these areas cause great variability in evaporation that drives surface temperatures to be lower or higher (Chen et al. 2014, Sandholt et al. 2002). This temperature variation is hardly detected by the vegetation index, resulting in a triangular shape in the NDVI–LST feature space. Further causes of error can be associated to situations that do not follow the LST–NDVI inverse

relationship. When in high air temperature and sunlight conditions with limited water availability, low LST values are expected in high NDVI areas such as dense vegetation due to high transpiration (Anderson et al. 2012, Karnieli et al. 2010). However, in a scenario in which energy is the limiting factor, transpiration and evaporation are decreased, leading to an often-positive correlation between NDVI and LST. These findings suggest that the LST–NDVI relationship is geographically variable. The use of geographically weighted regression-based algorithms might be beneficial to address local variations in LST–NDVI correlation (Li et al. 2017).

4.3.1.3. TsHARP Validation comparison between VENµS and Sentinel-2

The validation results of MODIS coarse images' thermal sharpening using VENµS VNIR was compared to results from sharpening using Setninel-2 on 28 October at scenes 1 and 2 (Figure 4.7). The sharpening performance using both satellites was comparable for both scenes, yielding similar temperature errors, accuracy, and bias. The relationship between sharpened and reference temperatures was strong in all instances with values ranging from 0.68 to 0.80, and temperature uncertainty ranging from 1 to 1.47 °C. Although similar, MODIS/Sentinel-2 performance was slightly higher at 120 and 240 m in scene 2 when compared to scene 1, with R^2 values of 0.77 and 0.8, while VENµS sharpening showed higher accuracy in scene 1 at all four different spatial resolutions. MODIS/VENµS was also slightly more accurate than MODIS/Sentinel-2 in scene 1 in all spatial resolutions, with R^2 values of 0.71 and 0.69 at 30 m, 0.75 and 0.72 at 60 m, 0.78 and 0.75 at 120 m, and 0.80 and 0.76 at 240 m resolutions for MODIS/VENµS and MODIS/Sentinel-2 respectively, while in scene 2, both models had the same R^2 at 30 and 60 m, with Sentinel-2 achieving higher R^2 at 120 and 240 m. Overall, scene 2

showed lower RMSE, MAE, and bias than scene 1 in both models, with highest values of 1.16, 0.93, and −0.80 for VENμS, and 1.18, 0.96, and −0.80 for Sentinel-2, respectively.

4.3.2. Field Scale

Field boundaries were extracted from sharpened and reference images at 30, 60, 120 and 240 m to perform validation at a field scale for each individual field. The field selection criteria relied solely on the crop cultivated. Cotton fields were identified using USDA-NASS CropScape data layer from 2019.

4.3.2.1. MODIS/Sentinel-2 TsHARP validation

The validation of the sharpening algorithm in scene 2 was performed in eight fields on 9 September (Figure 4.8). An overall strong relationship between sharpened and reference temperatures was observed in fields 1 and 3 across all spatial resolutions, with R^2 values ranging from 0.60 at 30 m to 0.94 at 240 m, and 0.64 at 30 m to 0.88 at 120 m, respectively. The weakest relationships were observed for fields 8 and 4, wherein the model's accuracy was below 0.5 in all resolutions. Remaining fields showed strong relationships at 60, 120, and 240 m, with the exception of field 5, in which higher accuracy was obtained only at coarser resolutions of 120 and 240 m. Only three fields showed moderate to strong relationships at the finest targeted resolution, while for the other resolutions, temperature estimation results were more reliable, with most fields having higher accuracy maps. Temperature uncertainty of higher than 2 °C was obtained for fields 1, 2, and 5, while field 6 resulted in errors lower than 1 °C (Figure 4.8 (b)).

The negative bias shown in all areas indicated an underestimation of BT when compared to reference data and it is consistent with the results obtained for the scene scale. The residual errors resulted from the linear regression between BT and NDVI showed errors ranging from −0.5 to 1 °C in the areas that fields were located. Nevertheless, temperature underestimation in

sharpened maps was as high as 2.5 °C in some fields, likely due to a discrepancy in temperatures collected by both thermal sensors in these specific areas, rather than due to a weak relationship between BT and NDVI. This temperature difference can be a result of biases caused by sensor parameters such as bandwidth, acquisition time, and geolocation errors (Weng et al. 2014).

The field scale validation results for scene 3 are shown in Figure 4.9. Due to the lower number of cotton fields in this scene and their smaller size, only five fields were selected for analysis. Nevertheless, a higher number of dates throughout the growing season were available for validation. High performances were observed in September (Figure 4.9 (b),(e)) and October (Figure 4.9 (c),(f)), in which most fields showed a strong relationship between sharpened and reference temperatures coupled with the low-temperature errors. A positive bias in September indicates that temperatures were overestimated at an average of 0.95 °C in all fields. Despite the high agreement between sharpened and reference temperatures observed for all fields in August, in one or more resolutions, temperature error was higher than in subsequent months (Figure 4.9 (a),(d)). Spatial resolutions of 60 and 120 m displayed the most consistent results along the three dates, with strong relationships in most fields. High R^2 values were observed in four out of five fields at 60 m resolution on the second and third dates, and two fields on the first date, while at 120 m, all five fields had strong relationships on the first date, four on the third, and three on the second. Sharpened maps at 30 m had the weakest performance, with a maximum of 2 fields presenting moderate relationships and overall temperature errors higher than coarser resolutions. Maps at 240 m had weaker performance in this scene due to the low or insufficient number of pixels for correlation caused by the smaller field sizes.

The resulting statistics indicated that the thermal sharpening of coarse MODIS images at the four finer resolutions are field-specific. The accuracy of sharpened temperatures in field 5

was high at all resolutions on the first date and was consistently high at 60 and 120 m in subsequent months. High-temperature maps' accuracy was observed in at least three resolutions at fields 2 and 3 in September and October, and at 240 m in the first month. The weakest performance was observed in field 4, in which sharpened maps had very low accuracy among all dates in most spatial resolutions when compared to Landsat reference temperatures. The fields that showed the strongest (field 5) and the weakest performances (field 4) were located side by side in the scene, suggesting that the sharpening results might be affected by field individual characteristics, planting date, and management practices.

High agreement between sharpened and reference maps at 60 m resolution was observed in field 1 for all three dates (Figure 4.10). Despite the higher temperature difference between sharpened and reference maps in August, the BT distribution patterns still showed great similarities. A high correlation between sharpened and reference maps was also shown on the subsequent dates. The high agreement between sharpened and reference maps shown in the validation process evidences great consistency in the TsHARP results. The robust results from the use of Sentinel-2 VNIR for sharpening presented in this study are corroborated by studies previously mentioned (Huryna et al. 2019, Sánchez et al. 2020).

4.3.2.2. MODIS/VENµS TsHARP validation

Figure 4.11 shows the quantitative statistics for TsHARP validation at two different dates in scene 1. The algorithm's performance presented variability between dates and areas, as previously observed. The model's accuracy was consistent across three out of the nine fields selected, with strong relationships in all resolutions in field 6 at both dates, and at the second date for fields 2 and 5. On 29 August, high-accuracy sharpened maps for fields 2 and 5 were observed at 60 and 120 m only. Fields 7 and 8 showed high R^2 values between sharpened and

reference temperatures only at the coarser resolutions of 120 and 240 m, while in remaining fields, the overall accuracy was low either on all or one of the dates. Disaggregated maps at 120, 240, and 60 m resolutions were the most consistent in terms of correlation with reference temperature maps. Temperature uncertainty was relatively low in most fields at both dates, with values ranging from 1.25 to 2.17 °C in August and 0.66 to 2.13 °C in September. An overestimation of sharpened temperatures was observed in August with a positive bias of 2.17 °C, while in September, sharpened temperatures were up to 2.01 °C lower than reference temperatures. On this date, temperature overestimation was observed only in field 4, in which sharpened temperatures were on average 0.66 °C higher than the reference.

In scene 2, the MODIS images' sharpening using VENμS NDVI was validated on one date in the beginning of September, with three days difference from the MODIS/Sentinel-2-derived sharpened image (Figure 4.12). A field scale comparison between these two sharpened maps was not performed because of the time difference, however similarities in the results were observed. Fields 8 and 4 had weak relationships between sharpened and reference temperatures in all spatial resolutions, repeating the weak performance seen in the MODIS/Sentinel-2 scene. These results suggest that the poor accuracy of the sharpened maps was caused by subfield land cover variability that was not depicted in the coarse MODIS pixel resolution, such as a mix of exposed soil and canopy cover. The possible effects of different field conditions will be discussed in the next subsection.

Overall, sharpening accuracy was high at 60, 120, and 240 m, with at least half of the fields showing R^2 values higher than 0.62. Only three fields had moderate to strong relationship at 30 m, with the highest value of 0.68. Overall, RMS errors were below 1.73 at all four resolutions. Temperature uncertainty as low as 0.25 °C was achieved at 240 m in field 2 and as

low as 0.38 °C at 30 m. Bias indicated that sharpened temperatures were overestimated in all fields (Figure 4.12 (b)). High-accuracy sharpened maps were achieved for all resolutions in field 3 (Figure 4.13). Sharpened map with 30 m pixel size provided the most detailed insight in the BT distribution in the field (Figure 4.13 (a)). The same BT patterns were maintained when pixel size was doubled, and sharpening accuracy increased from 0.68 to 0.8 (Figure 4.13 (e),(f)). The two coarser maps presented even higher accuracy of 0.89 and 0.86, but temperature distribution patterns in the field became harder to identify (Figure 4.13 (c),(d)). Exposed soil at the northern part and in the middle of the lower half of the field, most likely caused by erosion processes over the years, resulted in an overestimation of sharpened temperatures in those pixels. In these areas, sharpened temperatures were around 30.8 °C, while in the reference image, the same pixels varied from 28 to 29 °C, causing a decrease in the overall accuracy at 30 m. Background soil reflectance can also affect the sharpening performance throughout the season, once the low vegetation cover in the first stages of crop development can lead to high amounts of mixed pixel reflectance and consequently, an overestimation of canopy sharpened temperatures.

Disaggregation methods are often studied in large scene scales. Few authors have attempted to use this methodology for small agricultural areas. Sánchez et al. (2020) used Sentinel-2 to sharpen MODIS coarse thermal images to 10 m resolutions over a semi-arid agricultural area in southeast Spain. An average temperature uncertainty of 2 °C was observed. Temperature errors between 2 and 3 °C were observed by Bisquert et al. (2016). In a simulated experiment, Landsat 7 thermal images were aggregated to coarse resolution and then sharpened, achieving temperature uncertainty of ~1 °C (Agam et al. 2007a). In the present study, temperature errors for field scale ranged from 0.25 to 3.11 °C using both Sentinel-2 and VENμS, following results found by the other authors. Furthermore, it has been reported that absolute

temperature errors of up to 1.5 °K are suitable for agricultural management decisions (Sobrino et al. 2016, Ghent et al. 2017, Sánchez et al. 2020). Results from this paper are encouraging. A great number of fields presented low errors at 240 and 120 m, and at the finer resolutions of 60 m and in lesser cases of 30 m. The high-accuracy maps generated from this methodology with relatively low errors show a great potential in the use of TsHARP in MODIS/Sentinel-2 and MODIS/VENµS combinations for field scale.

Figure 4.14 shows field 3 sharpened temperature distribution in relation to air temperature on 5 days throughout the growing season from June to September at 60 m resolution. Air-canopy temperature difference is a well-recognized indicator of water stress in cotton (Jackson et al. 1981, Wanjura et al. 2000). Field canopy temperatures in June were less than 3 °C below air temperature, while in August and September, this difference was as high as 5 °C. Air-canopy temperature distribution was very similar throughout the field in the first and last dates. In the dates from mid-June to early September, a slight variability in air-canopy temperature distribution is observed. The use of a high spatial resolution satellite such as VENµS with high revisit time to sharpen coarse thermal images presents great potential to enable a more frequent monitoring of canopy temperature changes across the field throughout the growing season, with a fine resolution with the aim to identify crop water stress patterns in the field for management zone delineation. It is important to note that for a better estimation of plant water status, the sharpened BT values should be converted to LST.

4.3.2.3. Effects of in-field land cover variability on TsHARP performance

Two fields from scene 1 in Miller county were selected to demonstrate how different field conditions can positively or negatively affect the accuracy of resulting sharpened maps in a field scale. Figure 4.15 shows an example of the comparison between before and after exclusion

of selected areas within fields 3 and 9. Land patches covered by vegetation other than the cultivated crop, roads, flow channels caused by erosion, exposed soil, and waterlogged areas were extracted from the field boundaries for validation (Figure 4.15(e)-(h)). These areas were usually responsible for decreasing the level of accuracy between reference (Figure 4.15(a),(c)) and sharpened (Figure 4.15(b),(d)) maps. This difference was likely caused by the sharpening technique reliance on the BT–NDVI relationship, once many of these land cover types mentioned have low NDVI values resulting in high sharpened temperatures, while reference images are dependent on the temperature variability itself and not on the NDVI patterns throughout the area.

Reference and sharpened maps after the pixel removal process of fields 3 and 9 are shown in Figure 4.15(i)-(l). Note that the temperature distribution at sharpened and reference maps appear to become more alike in field 3 after removal of unwanted pixels. A circular area around the pivot, a narrow road, and a waterlogged area were excluded in this field, increasing the sharpening accuracy. This stronger relationship between the two maps was likely due to two factors: (1) exposed soil pixels from the road had low NDVI values, resulting in finer pixels with overestimated temperature at the sharpened map, and (2) the two remaining excluded areas had high moisture, which explains the lower temperature relative to the rest of the field in the reference map, while in the sharpened map, pixel temperatures were higher in these areas than in the remaining field due to the low NDVI values of water patches and wet soil. Conversely, the extraction process did not yield the same results for field 9 once BT pattern differences were still evident in the remainder of the field. Based on the temperature range in the reference image and on the premise that stressed cotton plants are usually up to 5 °C above air temperature (Idso et al. 1981, Cohen et al. 2005), it is possible to infer that the whole field was well-watered either due

to rain or irrigation events. The TsHARP algorithm may not detect the moisture variability caused by irrigation, since it accounts for the subpixel temperature variability related to the vegetation fraction, thus making irrigation events a common source of error (Agam et al. 2007a).

Although little information about most of the fields studied is known, it can be assumed that field-specific conditions are a determinant factor in the accuracy of sharpened temperatures. For instance, different authors have pointed out the limitations of thermal disaggregation in irrigated fields (Bisquert et al. 2016, Merlin et al. 2010). Surface temperature can rapidly respond to water stress, while NDVI has a slower response after initial stress (Sandholt et al. 2002). Agam et al. (2007a) discussed the importance of excluding selected pixels that do not conform to the inverse linear relationship between LST and vegetation fraction, such as water bodies that present both low NDVI and surface temperature. Furthermore, areas that have high NDVI variability may be a source of errors once this variability cannot be depicted by the coarse resolution pixels of MODIS images.

Temperature data from field 9 collected with Landsat resulted in higher temperature along the entire west edge of the field, potentially due to a mixed pixel response between the crop and the grassed area adjacent to the field. However, vegetation cover in the same area was high, leading to an opposing result in the sharpened image. The observations on the effect of undesirable pixels' removal on the thermal pixel disaggregation performance are reinforced by statistics shown in Figure 4.16. A higher level of agreement between the sharpened and reference temperatures was displayed after pixel extraction in field 3 on both dates, as well as a decrease in temperature errors, whereas in field 9, the accuracy decreased at 30 and 120 m, despite slightly lower errors being achieved.

4.4. Conclusions

Corroborating findings found in the literature, results from this study highlighted the differences in coarse-resolution BT between MODIS and Landsat. For the five dates for which imagery from both sensors were acquired on the same day, observed average MAE was 1.63 °C. Coefficient of determination within the same dates varied from 0.34 to 0.74, with scene MODIS BT frequently being cooler than Landsat-8. Further research can benefit from implementation of intercalibration between MODIS and Landsat-8 before sharpening validation to attenuate errors caused by the sensors' individual characteristics. Despite the inconsistent correlations in coarse resolution caused by these differences and the presence of clouds in one or both images, relationships between sharpened MODIS and Landsat were stronger at all finer resolutions.

Field-scale agreement between sharpened and reference temperatures showed some level of independence from the scene scale. Agricultural fields located in regions of the scene with smaller residual errors or not affected by cloud cover can show higher temperature accuracy than other areas. These findings suggest that sharpened maps can be used with caution for small scales even if coarse comparison between sensors in the scene scale shows weaker relationships.

Sharpened maps at 120 and 60 m resolution showed the highest consistency within all fields and dates using both VENµS and Sentinel-2. Maps sharpened to 240 m showed high accuracy, but greatly depended on the field size because of the lack of pixels available in smaller areas. Resolutions finer than 60 m presented the least consistent relationships, with accurate maps being very field-specific.

Very few studies have explored the performance of thermal sharpening in field scales, and the use of VENµS multispectral data. Findings from this research show that considering the combination of pixel size, and temperature estimation accuracy and error, sharpened MODIS at

60 m are the most reliable for season-long cotton monitoring. The comparison between sharpened images using VENµS and Sentinel-2 was performed to evaluate a potential agreement between results, due to the lack of information available in the use of VENµS for thermal disaggregation. VENµS results showed comparable or higher accuracy than Sentinel-2. The superior performance coupled with the better revisit time evidences the great potential of using VENµS for frequent in-season crop monitoring for IMZ delineation.

This work is the first to report the use of VENµS images for thermal sharpening. Nevertheless, only an initial study was performed to explore the possibility of using sharpening at field scale for monitoring purposes. Further research with ground data collection is needed to explore field use limitations of this methodology, but these results give useful insights of potential benefits of implementing the TsHARP technique as a tool for crop stress monitoring.

4.5. References

Ishimwe, R., Abutaleb, K., and Ahmed, F. (2014). Applications of Thermal Imaging in Agriculture- A review. *Advances in Remote Sensing* 3, 128-140.

Ribeiro da Luz, B. (2006). Attenuated total reflectance spectroscopy of plant leaves: a tool for ecological and botanical studies. *New Phytologist* 172, 305-318.

Hsiao, T. (1973). Plant Responses to water stress. *Annual Review of Plant Physiology* 24, 519-570.

Bodner, G., Nakhforoosh, A., and Kaul, H-P. (2015). Management of crop water under drought: a review. *Agronomy for Sustainable Development* 35, 401-442.

Falkenberg, N.R., Piccinni, G., Cothren, J.T., Leskovar, D.I., and Rush, C.M. (2007). Remote sensing of biotic and abiotic stress for irrigation management of cotton. *Agricultural Water Management* 87, 23-31.

Costa, J.O., Coelho, R.D., Barros, T.H.S., Junior, E.F.F., and Fernandes, A.L.T. (2020). Canopy thermal responses to water deficit of coffee plants under drip irrigation. *Irrigation and Drainage* 69, 472-482.

Panigada, C., Rossini, M., Meroni, M., Cilia, C., Busetto, L., Amaducci, S., Boschetti, M., et al. (2014). Fluorescence, PRI and canopy temperature for water stress detection in cereal crops. *International Journal of Applied Earth Observation and Geoinformation* 30, 167-178.

Elsayed, S., Elhoweity, M., Ibrahim, H.H., Dewir, Y.H., Migdadi, H.M., and Schmidhalter, U. (2017). Thermal imaging and passive reflectance sensing to estimate the water status and grain yield of wheat under different irrigation regimes. *Agricultural Water Management* 189, 98-110.

O'Shaughnessy, S.A., Evett, S.R., Colaizzi, P.D., and Howell, T.A. (2011). Using radiation thermography and thermometry to evaluate crop water stress in soybean and cotton. *Agricultural Water Management* 98, 1523-1535.

Cohen, Y., Alchanatis, V., Saranga, Y., Rosenberg, O., Sela, E., and Bosak, A. (2017). Mapping water status based on aerial thermal imagery: comparison of methodologies for upscaling from a single leaf to commercial fields. *Precision Agriculture* 18, 801-822.

Agam, N., Kustas, W.P., Anderson, M.C., Li, F. and Neale, C.M.U. (2007b). A vegetation index based technique for spatial sharpening of thermal imagery. *Remote Sensing of Environment* 107, 545-558.

Cohen, Y., Agam, M., Klapp, I., Karnieli, A., Beeri, O., Alchanatis, V., and Sochen, N. (2017). Future approaches to facilitate large-scale adoption of thermal based images as key input in the production of dynamic irrigation management zones. *Advances in Animal Bioscience* 8, 546-550.

Zhan, W., Chen, Y., Zhou, J., Wang, J., Liu, W., Voogt, J., Zhu, X., Quan, J., and Li, J. (2013) Disaggregation of remotely sensed land surface temperature: Literature survey, taxonomy, issues, and caveats. *Remote Sensing of Environment* 131, 119-139.

Bisquert, M., Sanchez, J.M., and Caselles, V. (2016). Evaluation of Disaggregation Methods for Downscalling MODIS Land Surface Temperature to Landsat Spatial Resolution in Barrax Test Site. *IEEE Journal of Selected Topics in Applied Earth Observations Remote Sensing* 9, 1430-1438.

Tom, V.T., Carlotto, M.J., and Scholten, D.K. (1985). Spatial Sharpening of Thematic Mapper Data Using a Multiband Approach. *Optical Engineering* 24, 1026-1029.

Kustas, W.P., Norman, J.M., Anderson, M.C., and French, A.N. (2003). Estimating subpixel surface temperatures and energy fluxes from the vegetation index-radiometric temperature relationship. *Remote Sensing of Environment* 85, 429-440.

Bindhu, V.M., Narasimhan, B., and Sudheer, K.P. (2013). Development and verification of a non-linear disaggregation method (NL-DisTrad) to downscale MODIS land surface temperature to the spatial scale of Landsat thermal data to estimate evapotranspiration. *Remote Sensing of Environment* 135, 118-129.

Wang, R., Gao, W., and Peng, W. (2020). Downscale MODIS Land Surface Temperature Based on Three Different Models to Analyze Surface Urban Heat Island: A Case Study of Hangzhou. *Remote Sensing* 12, 2134.

Sánchez, J.M., Galve, J.M., González-Piqueras, J., López-Urrea, R., Niclòs, R., and Calera, A. (2020). Monitoring 10-m LST from the Combination MODIS/Sentinel-2, Validation in a High Contrast Semi-Arid Agroecosystem. *Remote Sensing* 12, 1453.

Huryna, H., Cohen, Y., Karnieli, A., Panov, N., Kustas, W., and Agam, N. (2019). Evaluation of TsHARP Utility for Thermal Sharpening of Sentinel-3 Satellite Images Using Sentinel-2 Visual Imagery. *Remote Sensing* 11, 2304.

Ferrier, P., Crebassol, P., Dedieu, G., Hagolle, O., Meygret, A., Tinto, F., Yaniv, Y., and Herscovitz, J. (2020). VENµS (Vegetation and environment monitoring on a new micro satellite), in proceedings of the *IEEE International Geoscience Remote Sensing Symposium*, Honolulu, HI, USA, Jul. 2010, pp. 3736-3739.

Sharing Earth Obeservation Resources eoPortal Directory. Available online: https://directory.eoportal.org/web/eoportal/satellite-missions/v-w-x-y-z/venus. (accessed on August 25, 2020)

Kottek, M., Grieser, .J., Beck, C., Rudolf, B., and Rubel, F. (2006).World Map of the Köppen-Geiger climate classification updated. *Meteorologische Zeitschrift 15*, 259-263.

Beck, H., Zimmermann, N., McVicar, T., Vergopolan, N., Berg, A., and Wood, E. (2018). Present and future Köppen-Geiger climate classification maps at 1-km resolution. *Science Data* 5, 180214.

NOAA National Centers for Environmental information, Climate at a Glance: Regional Time Series, published December 2020. Available online: https://www.ncdc.noaa.gov/cag/ (accessed on December 23, 2020)

Boryan, C., Yang, Z., Mueller, R., and Craig, M. (2011). Monitoring US agriculture: the US Department of Agriculture, National Agricultural Statistics Service, Cropland Data Layer Program. *Geocarto International* 26, 341-358.

MODTBGA MODIS/Terra thermal bands daily L2G-Lite global 1 km SIN Grid V006. Available online: https://lpdaac.usgs.gov/products/modtbgav006/. (accessed on August 24, 2020)

QGIS Development Team. QGIS Geographic Information System; Open Source Geospatial Foundation , 2020.

Leroux, L., Congedo, L., Bellón, B., Gaetano, R., and Bégué, A. (2018). Land Cover Mapping Using Sentinel-2 Images and the Semi-Automatic Classification Plugin: A Northern Burkina Faso Case Study. In QGIS and application in agriculture and forest, Eds., Baghdadi, N., Mallet, C., Zribi, M., Wiley, Hoboken, NJ, USA, pp.119-151.

Choudhury, B., Ahmed, N., Idso, S., Reginato, R., and Daughtry, C. (1994). Relations between evaporation coefficients and vegetation indices studied by model simulations. *Remote Sensing of Environment 50*, 1-17.

Willmott, C.J. (1982). Some Comments on the Evaluation of Model Performance. *Bulletin of the American Meteorological Society 63*, 1309-1313.

Weng, Q., Fu, P., and Gao, F. (2014). Generating daily land surface temperature at Landsat resolution by fusing Landsat and MODIS data. *Remote Sensing of Environment* 145, 55-67.

Essa, W., Verbeiren, B., Van Der Kwast, J., and Batelaan, O. (2017). Improved DisTrad for Downscaling Thermal MODIS Imagery over Urban Areas. *Remote Sensing* 9, 1243.

Liu, Y., Hiyama, T., and Yamaguchi, Y. (2006). Scaling of land surface temperature using satellite data: A case examination on ASTER and MODIS products over a heterogenous terrain area. *Remote Sensing of Environment* 105, 115-128.

Chen, X., Li, W., Chen, J., Rao, Y., and Yamaguchi, Y. (2014). A Combination of TsHARP and Thin Plate Spline Interpolation for Spatial Sharpening of Thermal Imagery. *Remote Sensing* 6, 2845-2863.

Sandholt, I., Rasmussen, K., and Andersen, J. (2002). A simple interpretation of the surface temperature/vegetation index space for assessment of surface moisture status. *Remote Sensing Environment* 79, 213-224.

Anderson, M.C., Allen, R.G., Morse, A., and Kustas, W.P. (2012). Use of Landsat thermal imagery in monitoring evapotranspiration and managing water resources. *Remote Sensing of Environment* 122, 50-65.

Karnieli, A., Agam, N., Pinker, R.T., Anderson, M., Imhoff, M.L., Gutman, G.G., Panov, N., and Goldberg, A. (2010). Use of NDVI and Land Surface Temperature for Drought Assessment: Merits and Limitations. *Journal of Climate* 23, 618–633.

Li, X., Xin, X., Jiao, J., Peng, Z., Zhang, H., Shao, S., and Liu, Q. (2017). Estimating Subpixel Surface Heat Fluxes through Applying Temperature-Sharpening Methods to MODIS Data. *Remote Sensing* 9, 836.

Agam, N., Kustas, W.P., Anderson, M.C., Li, F., and Colaizzi, P.D. (2007). Utility of thermal sharpening over Texas high plains irrigated agricultural fields. *Journal of Geophysical Research* 112, D19110.

Sobrino, J.A., Jiménez-Muñoz, J.C., Sòria, G., Ruescas, A.B., Danne, O., Brockmann, C., Ghent, D., Remedios, J., North, P., Merchant, C. et al. (2016). Synergistic use of MERIS and AATSR as a proxy for estimating Land Surface Temperature from Sentinel-3 data. *Remote Sensing of Environment* 179, 149-161.

Ghent, D.J., Corlett, G.K., and Remedio, J.J. (2017). Global Land Surface Temperature From the Along-Track Scanning Radiometers. *Journal of Geophysical Research: Atmospheres* 122, 12167-12193.

Jackson, R.D., Idso, S.B., Reginato, R.J., and Pinter Jr., P.J. (1981). Canopy Temperature as a Crop Water Stress Indicator. *Water Resources Research* 17, 1133-1138.

Wanjura, D.F., and Upchurch, D.R. (2000). Canopy temperature characterizations of corn and cotton water stress. *Transactions of the ASAE* 43, 867-875.

Idso, S.B., Jackson R.D., Pinter, Jr, Reginato R.J., and Hatfield, J.L. (1981). Normalizing the stress-degree-day parameter for environmental variability. *Agricultural Meteorology* 24, 45-55.

Cohen, Y., Alchanatis, V., Meron, Y., Saranga, Y., and Tsipris, J. (2005). Estimation of leaf water potential by thermal imagery and spatial analysis. *Journal of Experimental Botany* 56, 1843-1852.

Merlin, O., Duchemin, B., Hagolle, O., Jacob, F., Coudert, B., Chehbouni, G., Dedieu, G., Garatuza, J., and Kerr, Y. (2010). Disaggregation of MODIS surface temperature over an

agricultural area using a time series of Formosat-2 images. *Remote Sensing of Environment* 114, 2500–2512.

TABLES AND FIGURES

Table 4.1. List of study sites and cotton fields for all three locations.

Location	Field ID	Coordinates	Area (ha)
Miller County, Georgia (scene 1)	1	31°11’53” N, 84°45’45” W	63.03
	2	31°13’3” N, 84°35’2” W	26.21
	3	31°05’55” N, 84°43’27” W	164.40
	4	31°06’37” N, 84°43’35” W	78.93
	5	31°08’31” N, 84°36’01” W	88.44
	6	31°07’06” N, 84°45’34” W	33.14
	7	31°07’50” N, 84°52’26” W	32.30
	8	31°06’21” N, 84°51’45” W	35.68
	9	31°11’20” N, 84°45’41” W	38.20

Baker County, Georgia (scene 2)	1	31°26’17” N, 84°36’02” W	66.80
	2	31°28’38” N, 84°39’46” W	59.07
	3	31°26’17” N, 84°36’38” W	63.11
	4	31°26’27” N, 84°34’34” W	48.30
	5	31°23’55” N, 84°32’53” W	58.45
	6	31°27’51” N, 84°28’08” W	56.74
	7	31°28’46” N, 84°29’30” W	33.47
	8	31°28’01” N, 84°33’24” W	90.91

Union County, Mississippi (scene 3)	1	34°21’40” N, 89°08’10” W	89.91
	2	34°48’05” N, 88°56’42” W	14.05
	3	34°24’07” N, 88°45’16” W	84.44
	4	34°20’04” N, 89°01’27” W	34.36
	5	34°19’57” N, 89°01’12” W	16.97

Table 4.2. Satellites' data acquisition dates for all three locations and selected dates for field scale validation of the Moderate Resolution Imaging Spectrometer MODIS for both Sentinel-2 and VENµS (gray).

Location	Landsat-8	MODIS	Sentinel-2	VENµS
	Acquisition Date			
Miller County	24 Aug -19	29 Aug-19	-	29 Aug-19
Georgia	09 Sept-19	10 Sept-19	-	10 Sept-19
(scene 1)	25 Sept-19	24 Sept-19	24 Sept-19	-
	27 Oct-19	28 Oct-19	27 Oct-19	28 Oct-19

Baker County	09 Sept-19	6 Sept-19	-	6 Sept-19
Georgia	09 Sept-19	09 Sept-19	09 Sept-19	-
(scene 2)	25 Sept-19	24 Sept-19	24 Sept-19	-
	27 Oct-19	28 Oct-19	27 Oct-19	28 Oct-19

Union, County	29 Aug-19	29 Aug-19	29 Aug-19	-
Mississippi	14 Sept-19	15 Sept-19	15 Sept-19	-
(scene 3)	30 Sept-19	3 Oct-19	3 Oct-19	-
	1 Nov-19	2 Nov-19	2 Nov-19	-

Table 4.3. Scene minimum, maximum, and temperature ranges for MODIS (1 km) and Landsat-8 (30 m) original images.

Satellite	Location	MODIS					Landsat-8			
		Date	Min	max	Range	Lag (days)	Date	min	max	Range
Sentinel-2	Scene 1	24 Sept	27.0	31.9	4.9	+1	25 Sept	27.6	35.9	8.3
		28 Oct	21.0	27.2	6.2	-1	27 Oct	21.0	29.5	8.5

	Scene 2	9 Sept	23.8	27.7	3.9	0	9 Sept	25.3	30.7	5.4
		24 Sept	24.5	32.4	7.9	+1	25 Sept	28.3	36.4	8.1
		28 Oct	20.1	25.0	4.9	-1	27 Oct	20.9	28.2	7.3

	Scene 3	29 Aug	21.7	26.0	4.3	0	29 Aug	23.6	32.4	8.8
		15 Sept	24.2	30.5	6.3	-1	14 Sept	21.9	29.9	8
		3 Oct	24.1	28.8	4.7	-3	30 Sept	23.0	30.9	7.9
		2 Nov	11.2	17.2	6.0	-1	1 Nov	7.3	14.5	7.2

VENμS	Scene 1	29 Aug	24.9	27.5	2.6	-5	24 Aug	23.0	26.5	3.5
		10 Sept	24.9	29.9	5.0	-1	9 Sept	26.3	33.6	7.3
		28 Oct	21.0	27.4	6.4	0	27 Oct	21.0	29.5	8.5

	Scene 2	06 Sept	27.3	31.3	4.0	+3	09 Sept	26.0	30.9	4.9
		28 Oct	20.1	25.0	4.9	-1	27 Oct	20.9	28.0	7.1

Landsat-8 acquisition time-scenes 1 and 2: 16:13 h, scene 3: 16:31 h; MODIS acquisition time: 100:05 h.

Table 4.4. Quantitative analysis of sharpened thermal maps using VENµS-derived normalized difference vegetation index (NDVI) in comparison to reference images from Landsat. Lag shows the difference in days between sharpened and Landsat-8 images.

Scene	Date	Lag	Resolution	VENµS			
				R^2	RMSE	MAE	bias
1	29 Aug-19	-5	30	0.48	1.70	1.57	1.48
			60	0.51	1.69	1.57	1.48
			120	0.52	1.67	1.56	1.48
			240	0.49	1.63	1.53	1.47
	10 Sept-19*	-1	30	0.52	2.37	2.12	-2.09
			60	0.54	2.31	2.07	-2.03
			120	0.53	2.26	2.02	-1.98
			240	0.49	2.20	1.98	-1.94
	28 Oct-19	0	30	0.71	1.43	1.13	-0.82
			60	0.75	1.36	1.07	-0.82
			120	0.78	1.29	1.01	-0.83
			240	0.80	1.23	0.98	-0.85

2	6 Sept-19*	+3	30	0.59	1.46	1.22	1.14
			60	0.63	1.41	1.20	1.14
			120	0.66	1.37	1.19	1.14
			240	0.67	1.32	1.17	1.13
	28 Oct-19	-1	30	0.68	1.16	0.93	-0.78
			60	0.72	1.11	0.90	-0.78
			120	0.76	1.06	0.87	-0.79
			240	0.79	1.01	0.85	-0.80

Table 4.5. Quantitative analysis of sharpened thermal maps using Sentinel-2 derived NDVI in comparison to reference images from Landsat. Lag shows the difference in days between sharpened and Landsat-8 images.

Scene	Date	Lag	Resolution	Sentinel-2			
				R^2	RMSE	MAE	bias
1	24 Sept-19*	+1	30	0.55	2.14	1.71	-1.44
			60	0.57	2.11	1.69	-1.45
			120	0.58	2.07	1.66	-1.45
			240	0.55	2.01	1.63	-1.48
	28 Oct-19	-1	30	0.69	1.47	1.15	-0.82
			60	0.72	1.41	1.10	-0.82
			120	0.75	1.35	1.05	-0.83
			240	0.76	1.29	1.02	-0.86

2	9 Sept-19*	0	30	0.60	1.96	1.78	-1.77
			60	0.64	1.94	1.77	-1.77
			120	0.64	1.93	1.77	-1.77
			240	0.63	1.91	1.78	-1.77
	24 Sept-19	+1	30	0.56	2.81	2.49	-2.43
			60	0.59	2.77	2.49	-2.43
			120	0.61	2.74	2.48	-2.44
			240	0.61	2.71	2.48	-2.46
	28 Oct-19	-1	30	0.68	1.18	0.96	-0.78
			60	0.72	1.12	0.91	-0.79
			120	0.77	1.05	0.87	-0.79
			240	0.80	1.00	0.85	-0.80

3	29 Aug-19	0	30	0.50	3.06	2.79	-2.79
			60	0.55	3.05	2.79	-2.79
			120	0.59	3.03	2.79	-2.79
			240	0.60	3.02	2.81	-2.81
	15 Sept-19*	-1	30	0.57	1.96	1.71	1.67
			60	0.62	1.92	1.70	1.67
			120	0.64	1.87	1.68	1.65
			240	0.66	1.81	1.65	1.62
	3 Oct-19*	-3	30	0.45	1.45	1.15	-0.52
			60	0.48	1.43	1.13	-0.50
			120	0.49	1.40	1.12	-0.48
			240	0.48	1.35	1.09	-0.45
	2 Nov-19	-1	30	0.64	3.85	3.67	3.67
			60	0.69	3.82	3.66	3.66
			120	0.74	3.76	3.65	3.65
			240	0.77	3.71	3.61	3.61

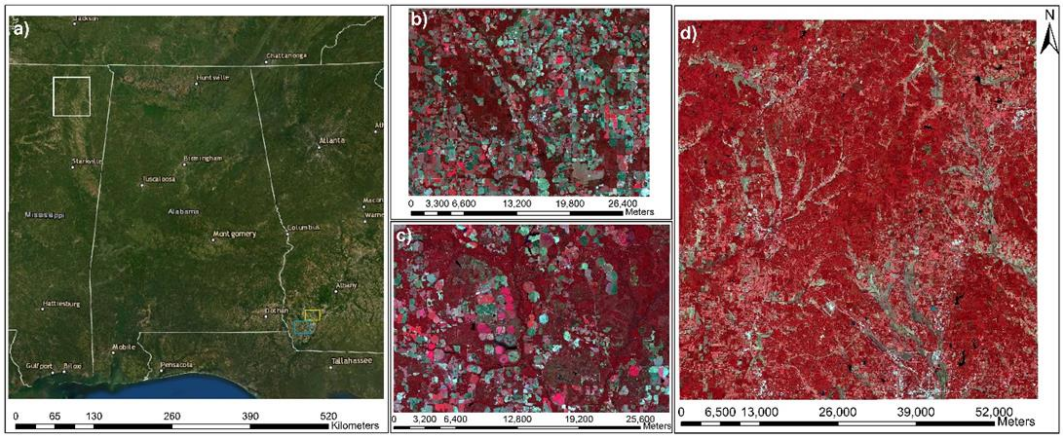

Figure 4.1. Study locations for (**a**) the polygons used to define the satellite scenes and Sentinel-2 false color composite of scenes used for thermal sharpening for study sites in (**b**) Miller County, Georgia (Scene 1) (**c**) Baker County, Georgia (Scene 2) and (**d**) Union County, Mississippi (Scene 3).

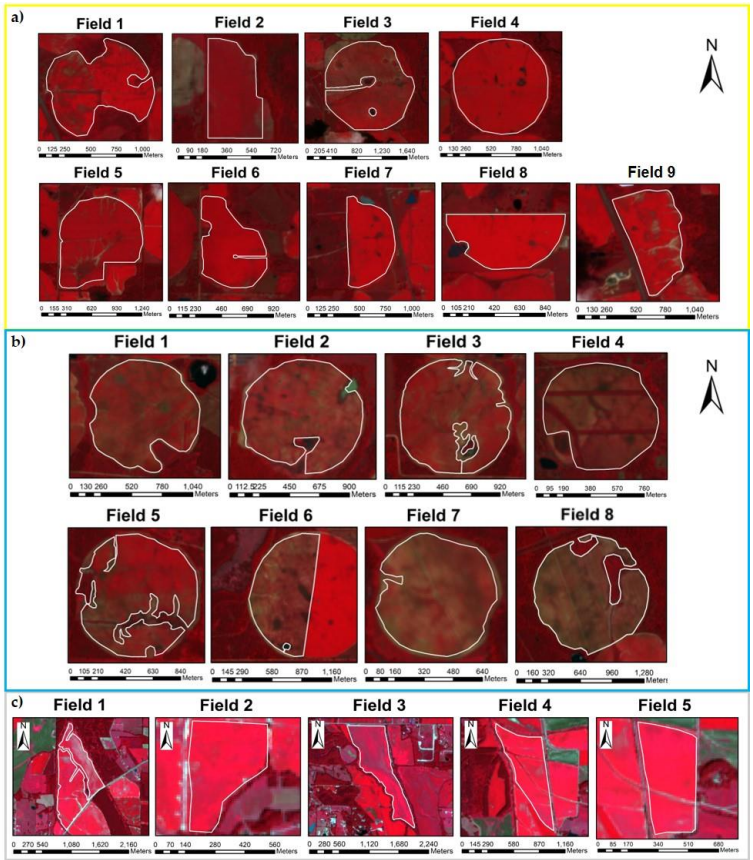

Figure 4.2. Individual fields assessed in **(a)** scene 1, **(b)** scene 2 and **(c)** scene 3. Field boundaries are overlaid on a Sentinel-2 false color composition from Sept. 9th, July 4th and Oct. 29th, 2019, respectively.

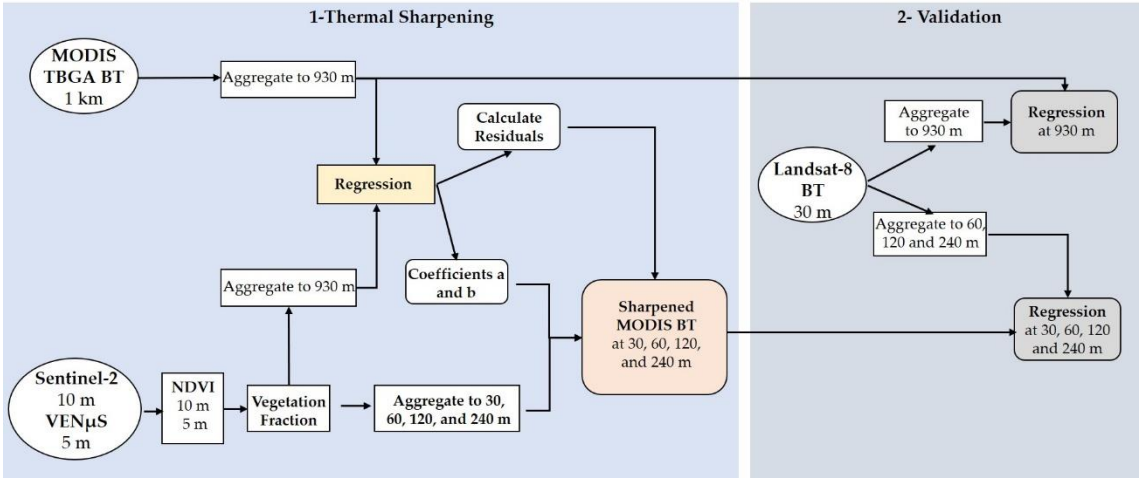

Figure 4.3. Flowchart of TsHARP methodology, including inputs, outputs and processing steps, and methodology validation using Landsat-8 images (modified after Huryna et al. (2019)).

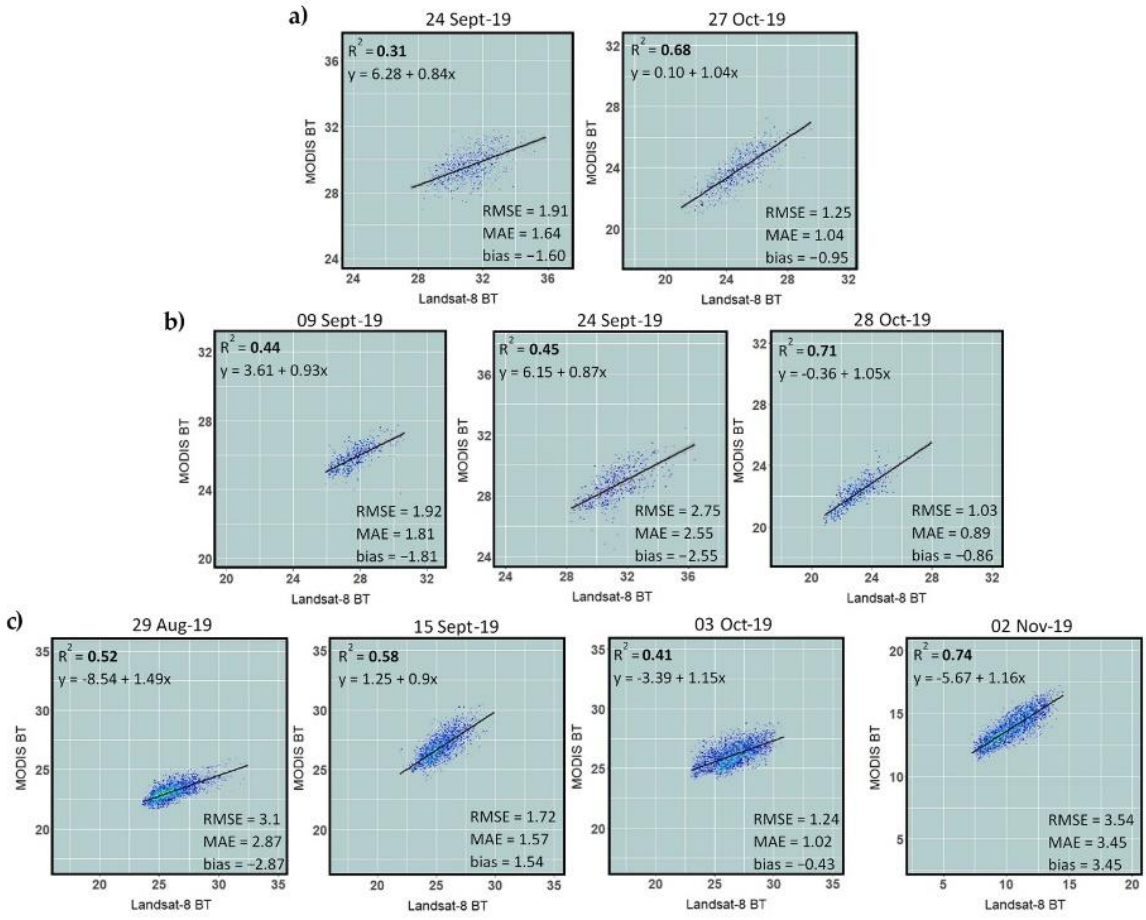

Figure 4.4. Relationship between MODIS BT and Landsat-8 BT at coarse resolution (930 m) in selected periods for Sentinel-2 at (**a**) scene 1 (Miller County, GA, USA), (**b**) scene 2 (Baker County, GA, USA), and (**c**) scene 3 (Union County, MS, USA). MODIS acquisition dates were used as the reference date.

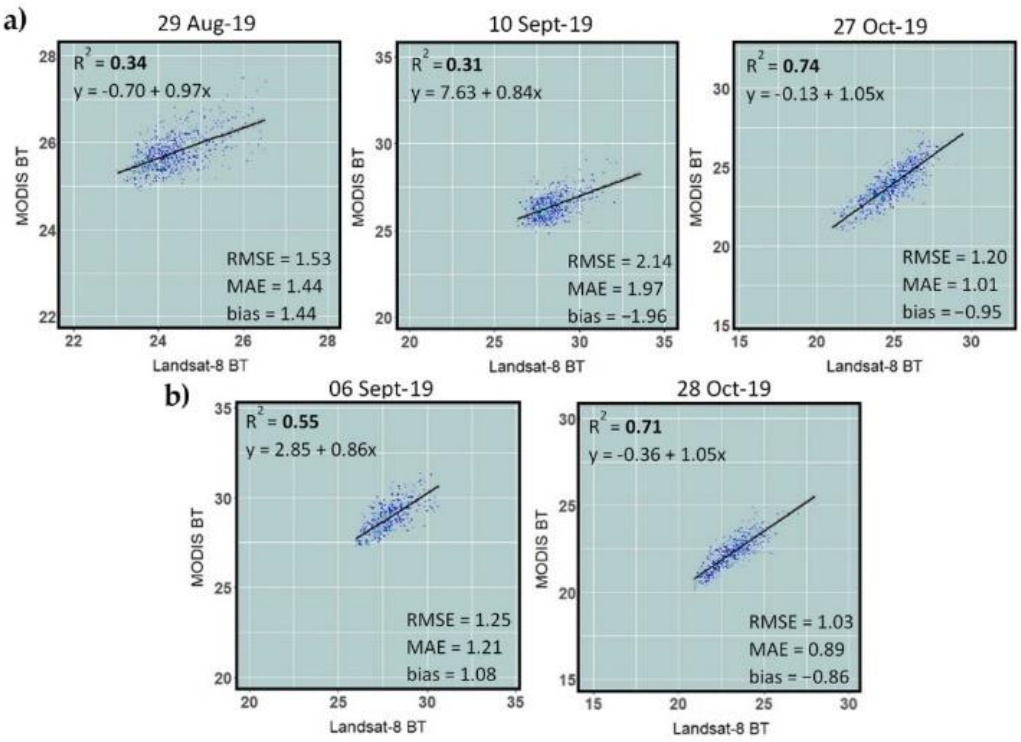

Figure 4.5. Relationship between MODIS BT and Landsat-8 BT at coarse resolution (930 m) in selected periods for VENµS at (**a**) scene 1 and (**b**) scene 2. MODIS acquisition dates were used as the reference date.

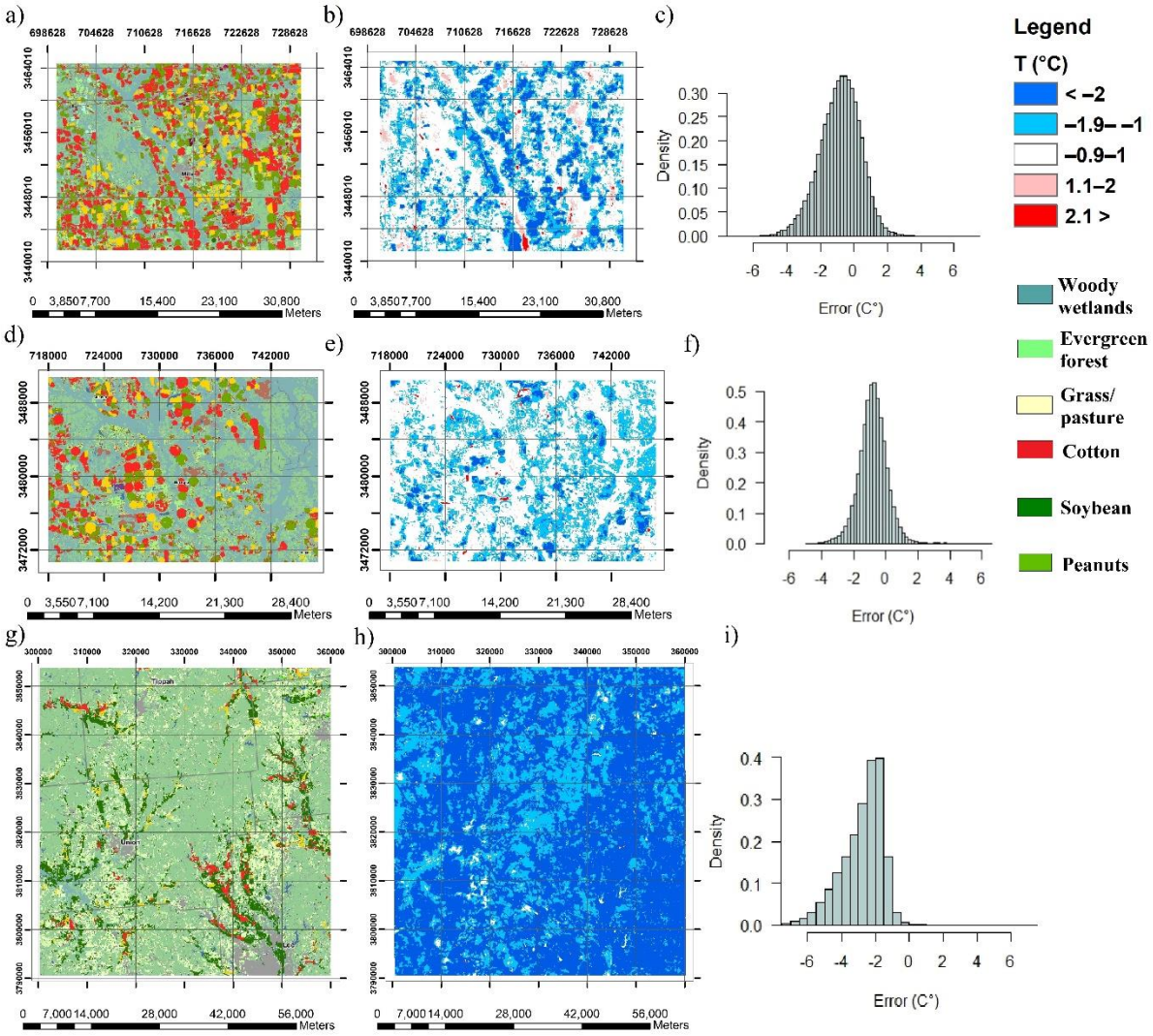

Figure 4.6. Land cover maps of (**a**) scene 1, (**d**) scene 2, and (**g**) scene 3, (**b**, **e**, **h**) are the respective temperature error maps (sharpened T (°C) − reference T (°C)) at 60 m resolution, and (**c**, **f**, **i**) are the respective error histograms. Error maps/histograms presented were created from MODIS/Sentinel-2 sharpening from the last date of scenes 1 and 2, and first date of scene 3.

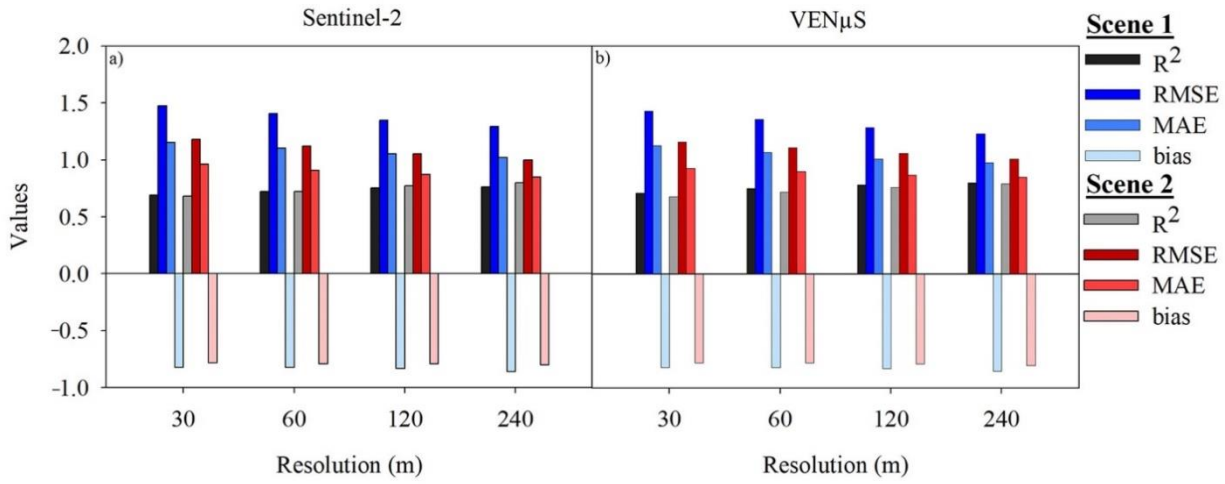

Figure 4.7. Quantitative statistics of TsHARP validation yielded by MODIS sharpening using **(a)** Sentinel-2 and **(b)** VENµS at scenes 1 and 2.

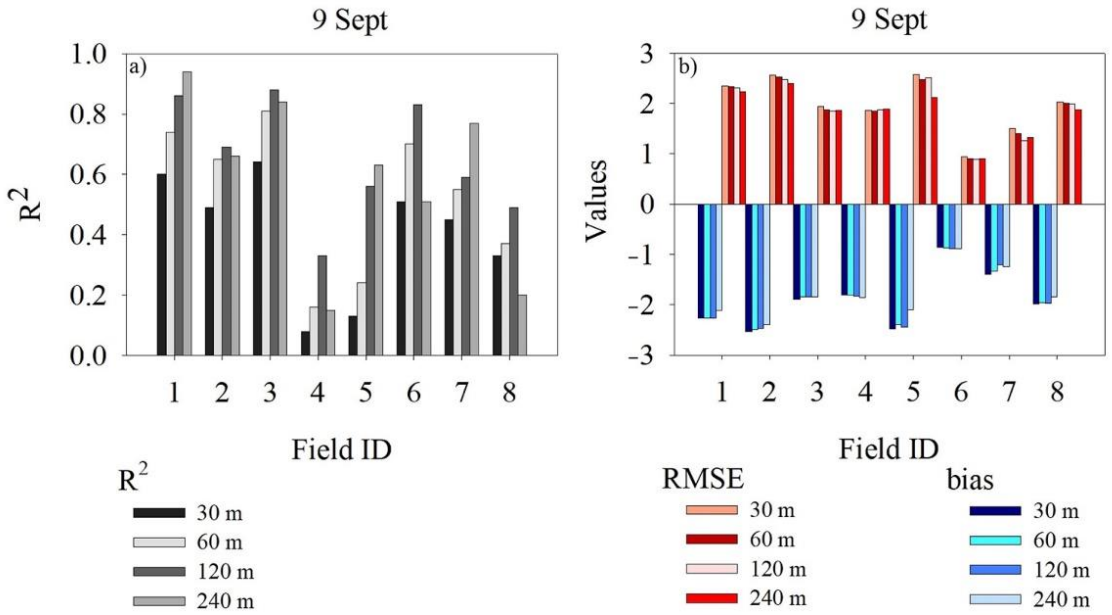

Figure 4.8. Quantitative statistics between sharpened and reference temperatures at field scale for fields selected in scene 2, including (**a**) coefficient of determination (**b**) RMSE, and bias.

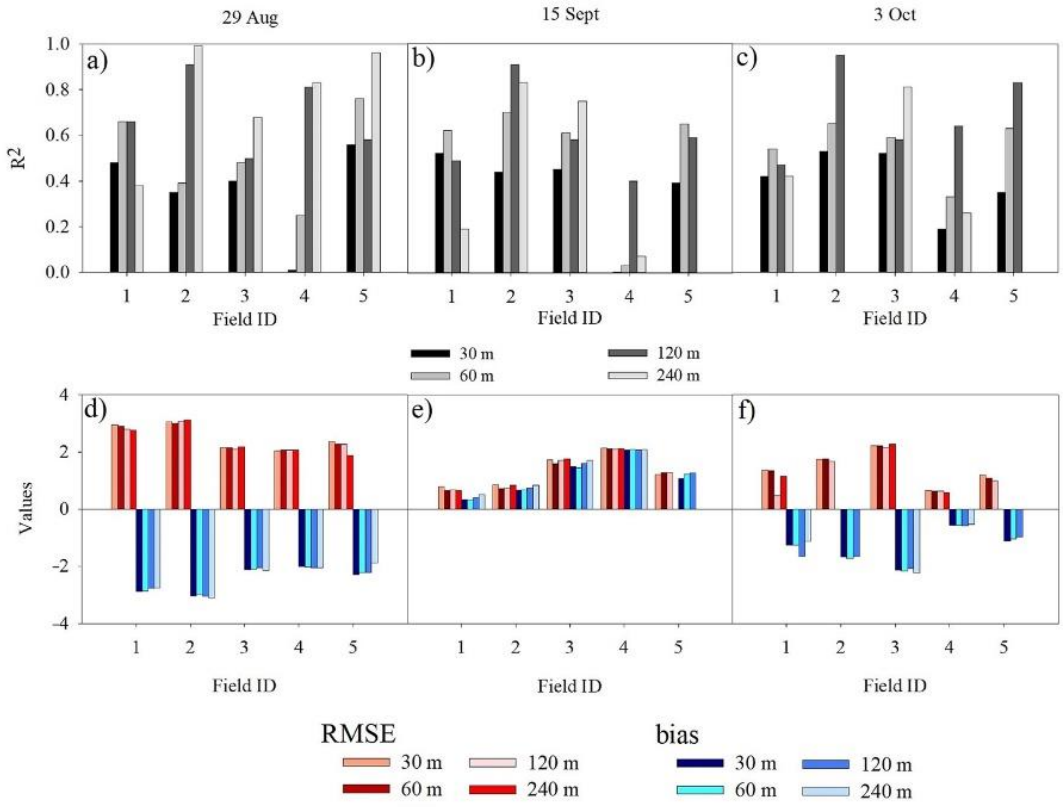

Figure 4.9. Quantitative statistics between sharpened and reference temperatures at field scale for fields selected in scene 3 on three different dates, including coefficient of determination on (**a**) 29 August (**b**) 15 September and (**c**) 3 October, and (**d**–**f**) RMSE and bias for the same dates, respectively.

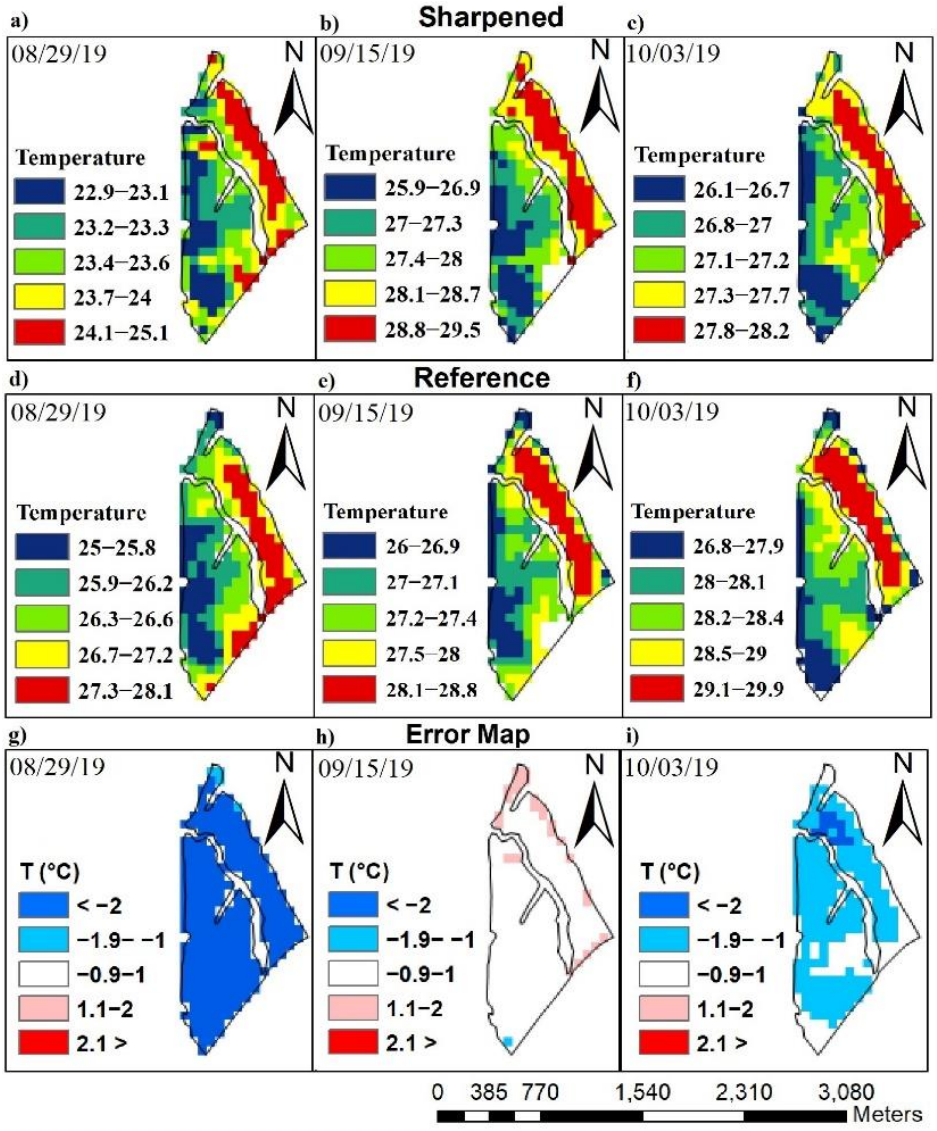

Figure 4.10. Field 1 sharpened temperature maps at 60 m resolution in Mississippi on (**a**) 29 August (**b**) 15 September and (**c**) 3 October, in comparison with respective (**d**–**f**) reference temperature maps. **(g-i)** Temperature error maps (sharpened T (°C) − reference T (°C)) for each date at 60 m resolution. Quantile method was used for classification.

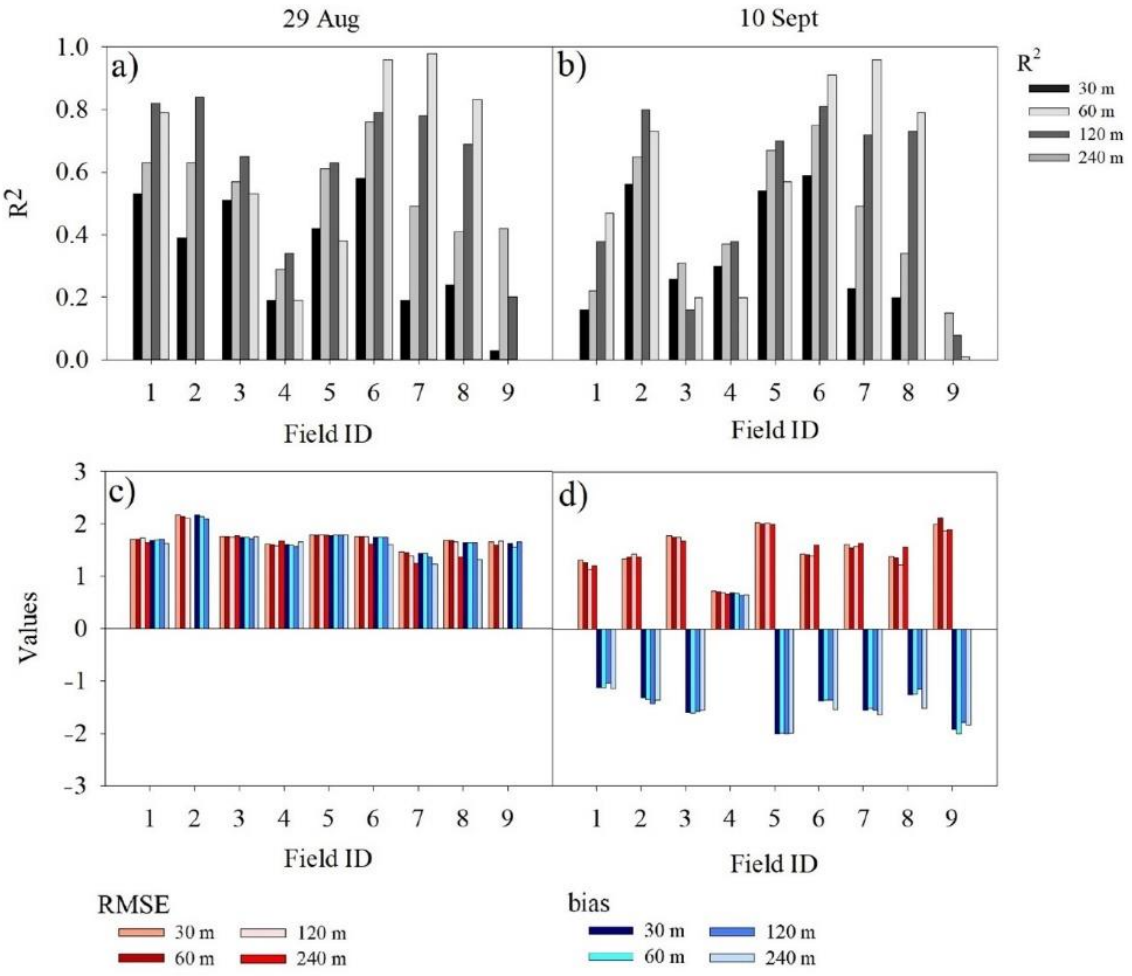

Figure 4.11. Quantitative statistics between sharpened and reference temperatures at field scale for fields selected in scene 1 including coefficient of determination, (**a**) 29 August and (**b**) 10 September, and (**c**–**d**) RMSE and bias for respective dates.

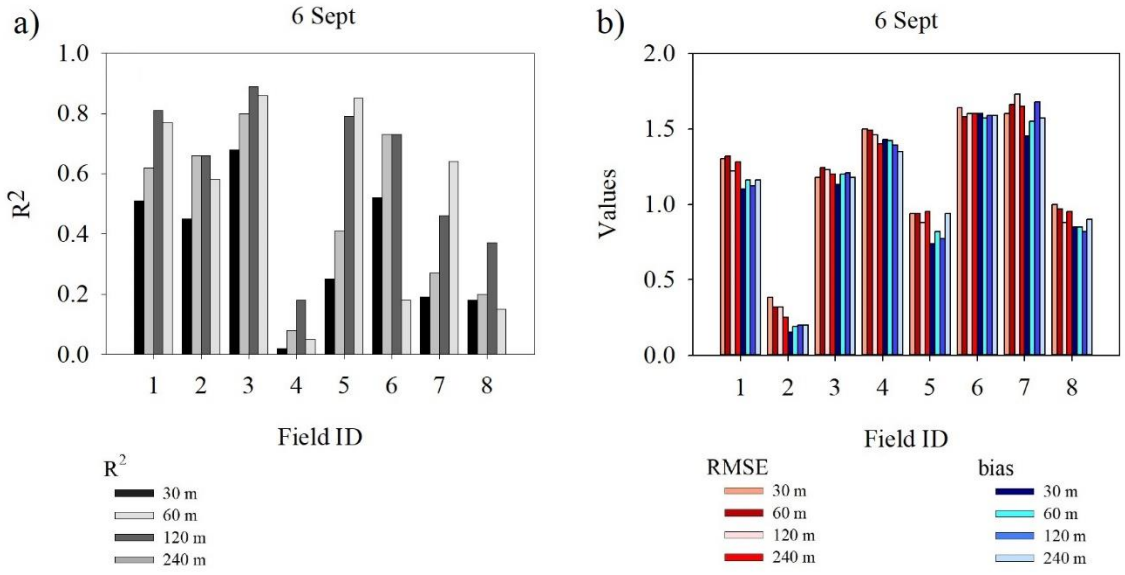

Figure 4.12. Quantitative statistics between sharpened and reference temperatures at field scale for fields selected in scene 2 including (**a**) coefficient of determination and (**b**) RMSE and bias.

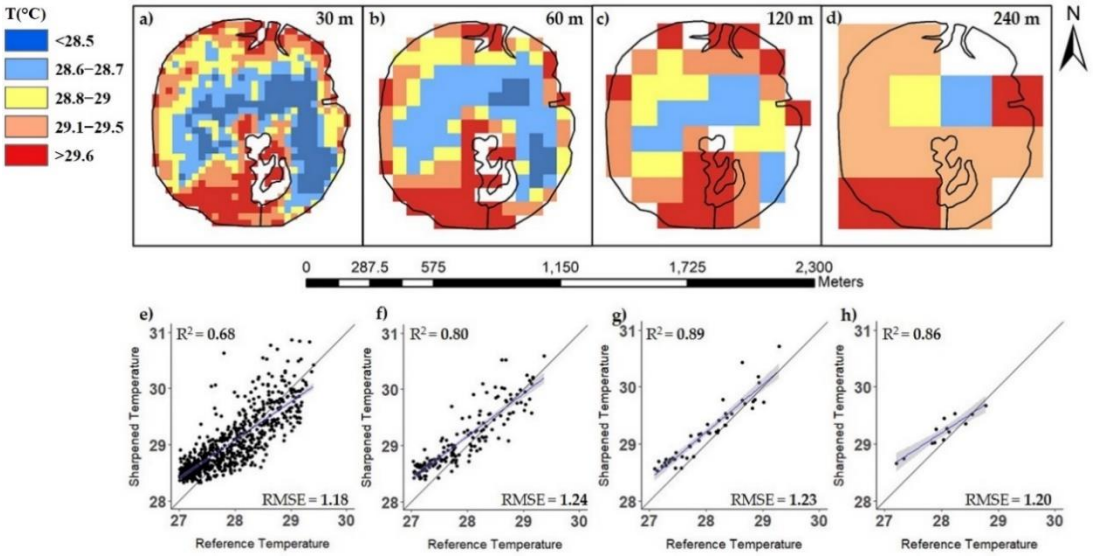

Figure 4.13. Field 3 sharpening maps of MODIS images using VENµS at (**a**) 30 (**b**) 60 (**c**) 120 and (**d**) 240 m resolution, and (**e**–**h**) the respective validation regressions.

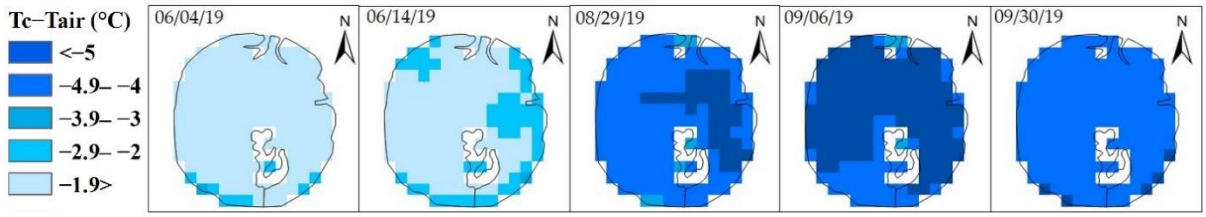

Figure 4.14. Field 3 time series of canopy temperature (Tc) - air temperature (Tair) distribution throughout the season. Canopy temperature used was extracted from the sharpened temperature maps.

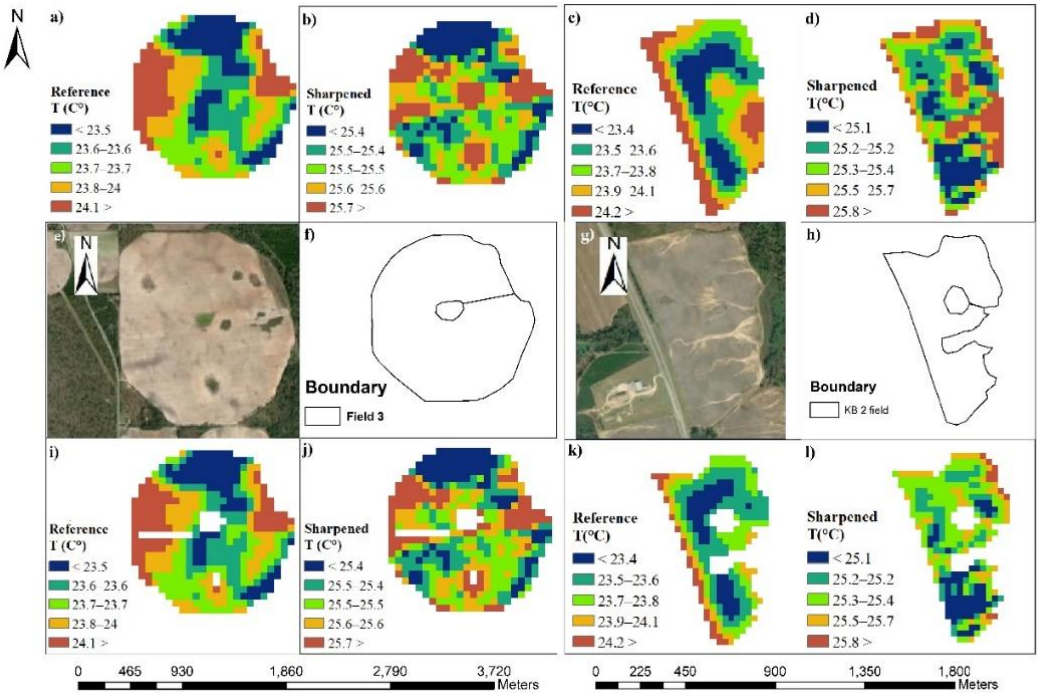

Figure 4.15. Field map comparison between reference and sharpened (MODIS/VENµS) maps before and after pixel removal. (**a**–**d**) Reference and sharpened maps of the whole area within fields 3 and 9. (**e**–**h**) Visual imagery and field boundary for both fields. (**i**–**l**) Reference and sharpened maps after pixel extraction for fields 3 and 9.

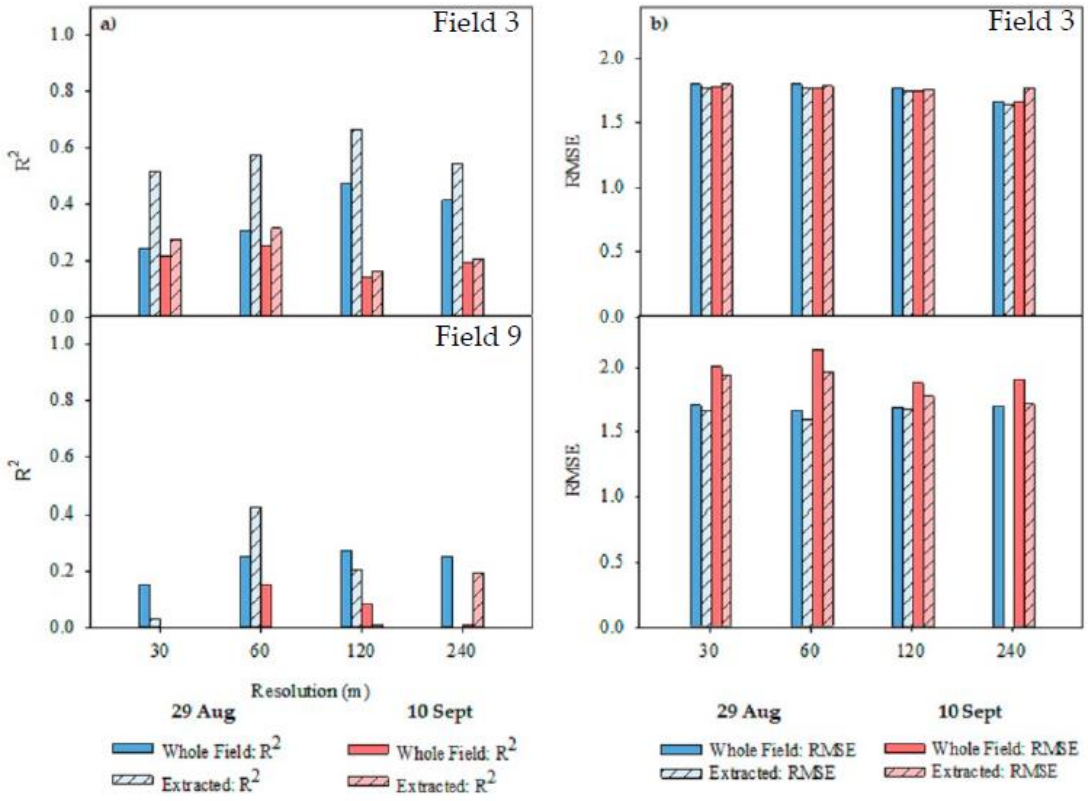

Figure 4.16. Fields 3 and 9 comparison statistics between sharpened and reference temperatures before and after pixel removal on 29 August and 10 September, including (**a**) coefficient of determination and (**b**) RMSE.

CHAPTER 5

CONCLUSIONS

The three studies conducted during the years of 2018, 2019 and 2020 approached how the use of remote sensing can improve precision irrigation practices in cotton. Remote sensing platforms such as UAVs and satellites provide an advantage to common field sampling tools which is the opportunity to collect data in large scale at a high frequency. Predawn LWP is regarded as a direct indicator of crop water status and recently it has been often used as a threshold for irrigation scheduling. Stomatal conductance is another physiological indicator of water stress in cotton. Cotton plants exposed to drought conditions close their stomata in an attempt to reduce water loss through transpiration leading to decreased stomatal conductance. Furthermore, stressed plants show increased leaf temperature because of the low transpiration rate.

In the study conducted in the 2018 and 2020 growing seasons in Camilla, GA the correlation between CWSI and cotton physiological parameters were explored. It was observed a strong relationship between predawn LWP and CWSI from all three different methodologies used to calculate CWSI using UAV-based canopy temperature. This strong relationship was in agreement with previous studies in the southern Georgia region. These results are important because it enables the creation of predicted LWP maps from remotely sensed canopy temperature data. In addition, individual bands in the visible and NIR regions of the spectrum were correlated with predawn LWP and stomatal conductance as a possible alternative method to using canopy temperature data. Bands red edge, and red showed high correlations with LWP

indicating that these two bands can be possibly combined in new vegetation indices as an alternative to the use of canopy temperature data.

One crucial technology to enable site-specific irrigation is VRI, in which water is applied in varied rates in a timely manner to meet crop water requirements. To enable different application rates to be applied areas of similar soil and landscape properties called IMZs are delineated. Currently, IMZs are delineated in the beginning of the season and used thereafter. However, results from our study (chapter 3) showed that there was high soil water tension and leaf water potential variability. The variability within individual IMZs evidenced the need to a dynamic IMZ delineation in which the zones can respond to in-field pattern changes during the season caused by the interaction of soil, plant, and environment.

In addition to the physiological parameters, mainstem height was found to be an indirect indicator of water stress because of the limited growth shown in water stressed plants. In chapter 3 the use of predicted plant height map to delineated in-season IMZ map during the vegetative stage of cotton was explored. IMZs boundaries changes once during this stage following plant height patterns. Average plant heights showed a strong linear relationship with cotton yield. The predicted plant height map also showed high similarity with final yield.

Extending the research in the use of remotely sensed canopy temperature, the sharpening of satellite thermal images at field scale was assessed. MODIS thermal images are available for free in a daily basis. However, because of its coarse resolution these images are not useful for field scale application. The TsHARP technique was used to sharpen MODIS surface temperatures to 30, 60, 120, and 240 m spatial resolution using NDVI developed from Sentinel-2 and VENμS. Images sharpened to 240 m showed the highest temperature accuracy during validation. Nevertheless, the accuracy was highly dependent on field size, once smaller fields did

not have enough pixels. In this context, images sharpened to 120 and 60 m were the most consistent for both Sentinel-2 and VENµS due to its finer pixels size. Results from this study are relevant to the use of satellite thermal images. Very few studies have explored the use of thermal disaggregation for field scale, and no studies have been published on the use of VENµS.

The results achieved from the three studies discussed showed great relevance in the use of remote sensing to delineate dynamic IMZs for VRI in cotton. Although the southern region of the USA has a humid climate with rainy summer season, episodic droughts during the cotton growing season are common and can decrease final yields. The use of site-specific irrigation to apply water to meet the crop needs at a timely manner can help mitigate the damaging effects of drought and increase irrigation water use efficiency. Further research needs to be conducted to further evaluate the benefits of applying the methodologies discussed, but remote sensing shows great promise in the frequent monitoring of crop status during the season.